Spectroscopic characterization of ion motion for an optical clock based on Coulomb crystals

Von der QUEST-Leibniz-Forschungsschule der
Gottfried Wilhelm Leibniz Universität Hannover
zur Erlangung des Grades

Doktor der Naturwissenschaften
Dr. rer. nat.

genehmigte Dissertation
von

M.Sc. Jonas Keller

geboren am 05. Dezember 1983 in Groß-Umstadt

2015

Referent: Prof. Dr. Piet O. Schmidt
Korreferent: PD Dr. Ekkehard Peik
Korreferent: PD Dr. Kilian Singer
Tag der Promotion: 09. Oktober 2015

Zusammenfassung

Lasergekühlte gefangene Ionen gehören zu den vielversprechendsten Ansätzen für einen optischen Frequenzstandard und haben bereits relative Frequenzunsicherheiten im Bereich von wenigen 10^{-18} ermöglicht. Aktuelle Umsetzungen basieren jedoch auf einem einzelnen Ion, wodurch das Signal-zu-Rausch-Verhältnis stark begrenzt ist und tagelange Mittelungszeiten nötig sind, um die hohe Frequenzgenauigkeit auflösen zu können. Dieser Zeitbedarf stellt insbesondere für mögliche Anwendungen ein Hindernis dar und kann deutlich verringert werden, indem ein Ensemble aus mehreren Ionen gleichzeitig spektroskopiert wird. Dank der gegenseitigen Abstoßung können diese in einem gemeinsamen Potential gefangen werden, wobei sich kristalline Strukturen (Coulombkristalle) bilden. Die technische Herausforderung bei diesem Ansatz besteht darin, die hohe Frequenzgenauigkeit zu bewahren, die mit einem einzelnen Ion erreichbar ist.

In dieser Arbeit werden Beiträge zur Entwicklung einer optischen Uhr auf Grundlage von Coulombkristallen aus $^{115}\mathrm{In}^{+}$- und $^{172}\mathrm{Yb}^{+}$-Ionen vorgestellt. Zur Stabilisierung von Spektroskopielasern wurden zwei hochstabile optische Resonatoren aufgebaut. Ein Diodenlaser konnte auf $\sigma_y(1\,\mathrm{s}) = 6 \times 10^{-16}$ stabilisiert werden. Die gemessene Vibrationssensitivität eines 30 cm langen Resonators mit einfachem Design zeigt dessen Eignung zur Laserstabilisierung mit einer relativen Frequenzinstabilität von $\sigma_y = 1 \times 10^{-16}$ für Zeiten $> 30\,\mathrm{ms}$, was ausreicht um das Quantenprojektionsrauschen von $7.2 \times 10^{-17}/\sqrt{\tau/\mathrm{s}}$ einer Uhr auf Grundlage von 100 $^{115}\mathrm{In}^{+}$-Ionen zu erreichen.

Frequenzverschiebungen durch Zeitdilatation aufgrund der Ionenbewegung tragen signifikant zur Unsicherheit aktueller Einzel-Ionen-Uhren bei. Zur Untersuchung der Bewegung von Coulombkristallen wurde ein Spektroskopielaser für einen schmalen Übergang in $^{172}\mathrm{Yb}^{+}$ aufgebaut. Eine EMCCD-Kamera ermöglicht räumlich aufgelöste Zustandsdetektion zur gleichzeitigen Abfrage mehrerer Ionen. Durch das Kühlen zweier Bewegungsmoden eines einzelnen Ions in den quantenmechanischen Grundzustand konnten Heizraten unter $2\,\mathrm{s}^{-1}$ bei Fallenfrequenzen um 500 kHz gemessen werden. Drei Methoden der Mikrobewegungskompensation wurden im Hinblick auf ihre Auflösung und Eignung zum Einsatz im Uhrenbetrieb untersucht. Für die Photonenkorrelationsmethode wurde ein neues Modell entwickelt, das eine quantitative Auswertung im experimentell üblichen Regime von vergleichbarer Fallenspannungsfrequenz und Linienbreite erlaubt. Es wurde im experimentellen Vergleich mit Messungen des Mikrobewegungsseitenbands bestätigt. Mit der Photonenkorrelations- sowie mit der parametrischen Heizmethode konnte Mikrobewegungskompensation mit relativen Frequenzunsicherheiten deutlich unterhalb von 1×10^{-19} gezeigt werden. Insgesamt wurde gezeigt, dass sich bewegungsbedingte Frequenzverschiebungen aufgrund externer Heizraten, Säkular- und Mikrobewegung bei einem einzelnen Indium-Ion im aktuellen Aufbau jeweils im Bereich von 10^{-19} kontrollieren lassen und es wurde die Grundlage für Messungen mit mehreren Ionen geschaffen.

Schlagwörter:
optische Uhren, Coulombkristalle, ultrastabile Laser, Spektroskopie

Abstract

Laser-cooled, trapped ions are among the most successful candidates for an optical frequency standard, with fractional frequency uncertainties approaching the low 10^{-18} range. However, current implementations of optical ion clocks are based on a single reference ion, which results in an intrinsically low signal-to-noise ratio. Averaging times of several days are necessary for resolving the transition frequency well enough to benefit from these low systematic uncertainties. In order to overcome this impediment to applications, the averaging can be performed more quickly by interrogating an ensemble of ions simultaneously. Due to their mutual repulsion, these ions can be confined by a common trapping potential, in which they arrange in crystalline structures (Coulomb crystals). The technical challenge of this approach is to preserve the excellent systematic uncertainties obtainable with a single ion.

This work contributes to the approach of using $^{115}\mathrm{In}^+$ / $^{172}\mathrm{Yb}^+$ Coulomb crystals as the reference for an optical clock. Two ultra-stable cavities for the stabilization of spectroscopy lasers have been set up. With a simple setup, a diode laser has been stabilized to $\sigma_y(1\,\mathrm{s}) = 6 \times 10^{-16}$. The vibration sensitivity of a simple 30 cm long spacer has been measured, showing that a cavity using this spacer can provide a fractional frequency instability of $\sigma_y = 1 \times 10^{-16}$ for times $> 30\,\mathrm{ms}$, sufficient to operate a clock based on 100 $^{115}\mathrm{In}^+$ ions at its quantum projection noise limit of $7.2 \times 10^{-17}/\sqrt{\tau/\mathrm{s}}$.

Frequency shifts resulting from time dilation due to ion motion are among the limiting contributions in current ion frequency standards. A spectroscopy laser has been set up in order to characterize the motion of Coulomb crystals by interrogating a narrow transition in $^{172}\mathrm{Yb}^+$. Spatially resolved state detection with an EMCCD camera allows multiple ions to be interrogated simultaneously. Groundstate cooling of two modes in a single ion allowed the determination of heating rates below $2\,\mathrm{s}^{-1}$ at secular frequencies around 500 kHz. Three micromotion compensation techniques have been characterized in terms of their resolution and applicability during clock operation. A new model was developed for the photon-correlation technique to allow quantitative evaluation in the common regime of comparable drive frequency and linewidth. It was experimentally verified in a comparison with resolved sideband measurements. Both the photon-correlation and the parametric excitation method were shown capable of micromotion compensation with a resulting fractional frequency uncertainty well below 10^{-19}. Overall, it has been shown that the motional frequency shift contributions due to external heating, secular motion and micromotion in a single $^{115}\mathrm{In}^+$ ion can each be controlled at a level of 10^{-19} in the present setup and the foundation has been laid to extend these measurements to multiple ions.

Keywords: optical clocks, Coulomb crystals, ultra-stable lasers, spectroscopy

Contents

1. Introduction **1**

2. Theoretical background **5**
- 2.1. Fundamentals of a clock based on multiple ions 5
  - 2.1.1. Principle of an atomic clock 5
  - 2.1.2. $^{115}\mathrm{In}^{+}$ as a frequency reference 5
  - 2.1.3. Instability of a multi-ion frequency standard 7
  - 2.1.4. Local oscillator requirements 8
- 2.2. Motion of ion Coulomb crystals in a Paul trap 10
  - 2.2.1. Single ion equations of motion 10
  - 2.2.2. Normal mode spectrum of a mixed-species crystal 12
- 2.3. Interaction of trapped ions with light 14
  - 2.3.1. Motional frequency shifts 17
  - 2.3.2. Spectroscopic temperature determination 18
- 2.4. Crystal configuration considerations for a clock 20

3. Experimental setup **23**
- 3.1. The ion trap 23
- 3.2. Optical setup 24
  - 3.2.1. Lasers required for $^{172}\mathrm{Yb}^{+}$ 24
  - 3.2.2. Beam geometry 25
  - 3.2.3. Wavemeter laser stabilization 28
  - 3.2.4. Spatially resolved state detection with an EMCCD camera . . 29

4. Stable lasers for motional and clock spectroscopy **33**
- 4.1. Laser stabilization to optical cavities 33
  - 4.1.1. Thermal noise 34
- 4.2. Spectroscopy laser for $^{172}\mathrm{Yb}^{+}$ 35
  - 4.2.1. Environmental vibrations 35
  - 4.2.2. Thermal expansion and aging 39
  - 4.2.3. Power sensitivity 41
  - 4.2.4. Laser system and measured instability 43
  - 4.2.5. Suitability for spectroscopy 45
- 4.3. Clock laser cavity for $^{115}\mathrm{In}^{+}$ 47
  - 4.3.1. Geometry and FEM calculations 47
  - 4.3.2. Experimental determination of the vibration sensitivity . . . 49

5. Motional spectroscopy 53
5.1. The $^2S_{1/2} \leftrightarrow {}^2D_{5/2}$ transition in Yb$^+$ 53
5.2. Selection rules and geometrical considerations 54
5.3. Spectroscopy sequence and experimental prerequisites 56
    5.3.1. The spectroscopy sequence 56
    5.3.2. Repumpers 57
    5.3.3. Zeeman components and secular sidebands 59
    5.3.4. Magnetic field 59
5.4. Temperature measurements after Doppler cooling 63
5.5. Sideband cooling 65
    5.5.1. Heating rate measurement 68

6. Micromotion determination for frequency uncertainties below 10^{-19} 71
6.1. Quantification and compensation of excess micromotion 71
6.2. The resolved-sideband method 73
    6.2.1. IMM sampling in measurements at Doppler temperature . . . 74
6.3. The photon-correlation method 79
    6.3.1. Principle 79
    6.3.2. Experimental realization 84
    6.3.3. Quantitative comparison to sideband measurements 87
6.4. The parametric heating method 89
    6.4.1. Principle 89
    6.4.2. Experimental results 90
6.5. Comparison of the techniques 91
    6.5.1. Resolution limits 91
    6.5.2. Applicability during operation in a multi-ion clock 92
6.6. Trap characterization 94
    6.6.1. Compensation voltage electric fields 94
    6.6.2. Axial excess micromotion 96
    6.6.3. Long-term drift of electric stray fields 97

7. Summary and outlook 101

A. ^{172}Yb$^+$ spectroscopic data 107

B. Photo-ionization schemes 109

1. Introduction

Individual atoms, unlike macroscopic objects, possess highly reproducible properties and are available in practically infinite numbers. This consideration led James Clerk Maxwell to suggest their use as a reference for the units of time, length and mass in 1870 [1]. The idea was realized first for the unit of time, when the SI unit second was defined in terms of the frequency associated with the hyperfine splitting of the groundstate of an unperturbed ^{133}Cs atom in 1967.

Since the first realization 60 years ago [2], microwave atomic clocks have benefited strongly from technological advances, leading to a steady decrease in uncertainty by about one order of magnitude per decade. One of the milestones in this development is the implementation of laser cooling [3–5], as employed in fountain clocks [6, 7]. Besides permitting an increased interrogation time, it reduces systematic uncertainties due to the significantly lower atom temperature and the ability to perform atomic state preparation and readout in the same interaction region. The availability of ever more precise standards for frequency and time has in turn enabled new technologies, some of which have become an essential part of everyday life, such as high-bandwidth communication networks and global navigation satellite systems. Increased precision in atomic spectroscopy also benefits fundamental research, e.g. in the search for physics beyond the standard model (see, e.g. [8–11]).

Another major improvement of atomic frequency standards was enabled by the development of highly stable optical oscillators [12] and the invention of the optical frequency comb [13], which connects the domains of optical and radio frequencies. The use of optical instead of microwave transitions corresponds to a frequency increase by five orders of magnitude, which reduces the relative influence of many systematic shifts and allows a lower statistical uncertainty per averaging time. Optical clocks have since surpassed their microwave counterparts (see, e.g. [9, 14–18]), which means that their absolute optical frequency measurements are now limited by the realization of the SI second, for which a redefinition based on an optical transition is being discussed [19, 20].

With fractional frequency uncertainties approaching the low 10^{-18} range, relativistic effects have become significant in frequency standards [21]. The gravitational red-shift according to general relativity amounts to 10^{-16} per meter of height difference. With geoid data uncertainties corresponding to height differences on the order of $0.1\,\mathrm{m}$ [22], this contribution currently presents a limitation to the absolute frequency uncertainty. On the other hand, their sensitivity to the gravitational potential opens up a new application for optical clocks in geodesy [23]. The development of portable optical clocks for direct measurements of the gravitational potential is among the goals of a recently formed collaborative research center in Hannover [24].

Trapped ions are one of the most successful realizations of the atomic reference in an optical clock. The strong confinement in a radio-frequency (rf) Paul trap [25, 26] localizes an ion to within a few nanometers, facilitating the control of external fields in order to achieve low systematic uncertainties. Trap depths of several eV permit trapping times of hours to months, such that a high duty cycle for the interrogation can be achieved. Current implementations of ion-based optical clocks are operated with a single ion. While this allows excellent control of systematic shifts, the low signal-to-noise ratio (SNR) of the single-ion signal requires averaging times on the order of several days before the statistical uncertainty is reduced sufficiently to benefit from this accuracy. These long averaging times present a strong impediment to possible applications and require time-consuming measurements for clock intercomparisons and the determination of frequency ratios. A possible way to speed up the averaging process is to replace part of the time average with an ensemble average by using multiple reference ions [27, 28]. The technical challenge is to increase the number of ions without degrading the systematic uncertainty. The work presented in this thesis is a contribution toward an optical clock based on mixed-species Coulomb crystals, in which multiple $^{115}\mathrm{In}^+$ ions are used as the clock reference and $^{172}\mathrm{Yb}^+$ ions provide sympathetic cooling.

When multiple ions are confined by a common potential, their mutual repulsion leads to the formation of crystalline structures (Coulomb crystals) at low temperatures. The equilibrium positions within such a crystal are determined by the absence of a mean electric field in the combined potential of the trap and all other ions, and therefore the clock transition cannot be affected by a static Stark shift. However, unlike for a single trapped ion, static field gradients are unavoidable within an ion crystal. $^{115}\mathrm{In}^+$ is one of the possible candidates for this approach, since the clock transition connects states with vanishing electric quadrupole moments and is therefore insensitive to these gradients. Further favorable properties of $^{115}\mathrm{In}^+$ include the low sensitivities to the 2nd-order Stark [29] and Zeeman [30] effects.

As in the single ion case, motional shifts are one of the main concerns in a clock based on multiple ions. While the first-order Doppler shift is eliminated by the tight confinement in an ion trap, relativistic time dilation due to ion motion with respect to the interrogating laser frame of reference gives rise to a 2nd-order Doppler shift. The resulting fractional frequency shift amounts to -1×10^{-18} for a speed as low as $0.42\,\mathrm{m/s}$. Precise determination of the motional state is therefore crucial to achieve fractional frequency uncertainties of 10^{-18} and below, a requirement which is facilitated by the high masses of the chosen species. In particular, two distinct kinds of ion motion contribute to the frequency uncertainty. The first is thermal motion, which can be reduced by laser cooling. Since groundstate cooling of extended crystals is challenging and time-consuming, it is more feasible to operate such a clock with Doppler-cooled ions and correct for the resulting motional frequency shift, as deduced from precise temperature measurements. Each ion adds three degrees of freedom to the crystal motion, with varying degrees of Doppler cooling efficiency. Low external heating rates [31] are essential to ensure that the Doppler limit can be reached for all of them, in order to minimize the overall temperature uncertainty. The second type of motion is micromotion [32], a fast oscillation driven by the confining rf electric field of the Paul trap. While a single ion can typically be moved to a position with vanishing micromotion, this is not necessarily possible for several ions simultaneously. A multi-ion clock therefore requires an ion trap with low heating rates, specifically designed to provide an extended region in which an ion crystal can be stored with low micromotion amplitudes [28, 33, 34].

Within this thesis, the means are provided to characterize both types of motion spectroscopically. A single $^{172}\mathrm{Yb}^+$ ion is used to characterize the external heating rates and electric field components in a prototype trap to ensure that the design and manufacturing tolerances fulfill the requirements of a multi-ion clock with motional fractional frequency uncertainties below 10^{-18}. Spectroscopic determination of the motional state is implemented in a scalable way, such that these measurements lay the foundation for tests with an increased number of ions.

The thesis is organized as follows: Chapter 2 reviews the theoretical fundamentals of a clock based on Coulomb crystals, including the stability requirements for the clock laser, trapped ion motion and the resulting frequency shifts. The main experimental apparatus, consisting of the ion trap, lasers, and the detection system, is introduced in chapter 3. Chapter 4 describes the setup of two ultra-stable reference cavities for lasers which address a narrow transition in each species. A simple ULE cavity setup is used to stabilize an external-cavity diode laser (ECDL) for sideband spectroscopy on the $^{172}\mathrm{Yb}^+$ $^2\mathrm{S}_{1/2} \leftrightarrow {}^2\mathrm{D}_{5/2}$ transition at 411 nm. A comprehensive study of contributions to frequency instability is presented for this cavity. For the laser addressing the $^{115}\mathrm{In}^+$ clock transition, a simple vibration-insensitive reference cavity design with a spacer length of 30 cm is developed and characterized. Based on an experimental determination of its vibration sensitivity and the results obtained with the $^{172}\mathrm{Yb}^+$ spectroscopy laser, it is shown that a laser stabilized to this cavity will allow the operation of a clock based on 100 $^{115}\mathrm{In}^+$ ions with a statistical uncertainty at the fundamental limit of the measurement process.

Two chapters are concerned with the determination of ion motional amplitudes in order to reduce the resulting frequency uncertainties. The implementation of sideband spectroscopy with $^{172}\mathrm{Yb}^+$, including groundstate cooling and determination of the radial trap heating rates, is the subject of chapter 5. Obtaining frequency uncertainties at a level of 10^{-18} and below also requires precise measurements of excess micromotion. The investigation of three established techniques at this level is described in chapter 6. In two cases, a refinement of models was necessary to explain the measured signals. The validity of the models is shown in experimental comparisons and a discussion of the obtainable resolutions and the applicability in a multi-ion clock is presented for each technique. Chapter 7 summarizes the results and gives an overview of further steps toward the realization of a multi-ion clock and the capabilities of the setup to investigate non-equilibrium dynamics in Coulomb crystals.

2. Theoretical background

2.1. Fundamentals of a clock based on multiple ions

2.1.1. Principle of an atomic clock

The measurement of time is based on counting the cycles of a periodic process. Figure 2.1 schematically shows the implementation of this measurement in an optical atomic clock: A frequency standard is obtained by stabilizing a laser to an atomic reference transition. The optical signal ($\approx 10^{15}\,\mathrm{Hz}$) is converted to the rf domain ($\approx 10^{8}\,\mathrm{Hz}$) by means of a frequency comb [13] to allow the use of electronics for the counting process. The pulsed nature and low SNR of the individual atomic interrogations requires the use of a flywheel oscillator to "keep track of cycles" during the time it takes to determine the transition frequency with the required uncertainty. This local oscillator (LO) is realized by stabilizing the clock laser with continuous feedback from a short-term frequency reference, typically an optical cavity. Both the absolute and short-term references are discussed within this thesis.

The two quantities which characterize the performance of a frequency standard are its instability and inaccuracy. The former is the statistical contribution to the frequency uncertainty and is therefore a function of averaging time. Its fundamental limitation and possible improvements by an increased number of interrogated ions is subject of section 2.1.3. The inaccuracy of an atomic frequency standard describes its systematic deviation from the unperturbed transition frequency. It needs to be estimated from independent measurements of all relevant influences, such as external fields and motional excitation. At the time of this writing, the lowest published fractional systematic uncertainty of an ion-based frequency standard is 3.9×10^{-18} [35]. In terms of inaccuracy, work presented in this thesis is concerned with reducing the uncertainty of motional shifts, which currently contribute a fractional uncertainty above 10^{-18} to all published uncertainty budgets for ion frequency standards (see, e.g. [14, 35, 36]). The equations of motion for ions in an rf Paul trap and the influence of ion motion on spectroscopy are therefore reviewed in sections 2.2 and 2.3, respectively.

2.1.2. $^{115}\mathrm{In}^{+}$ as a frequency reference

The choice of ion species for a multi-ion clock is affected by the unavoidable presence of static electric field gradients in a Coulomb crystal. A clock transition between two states

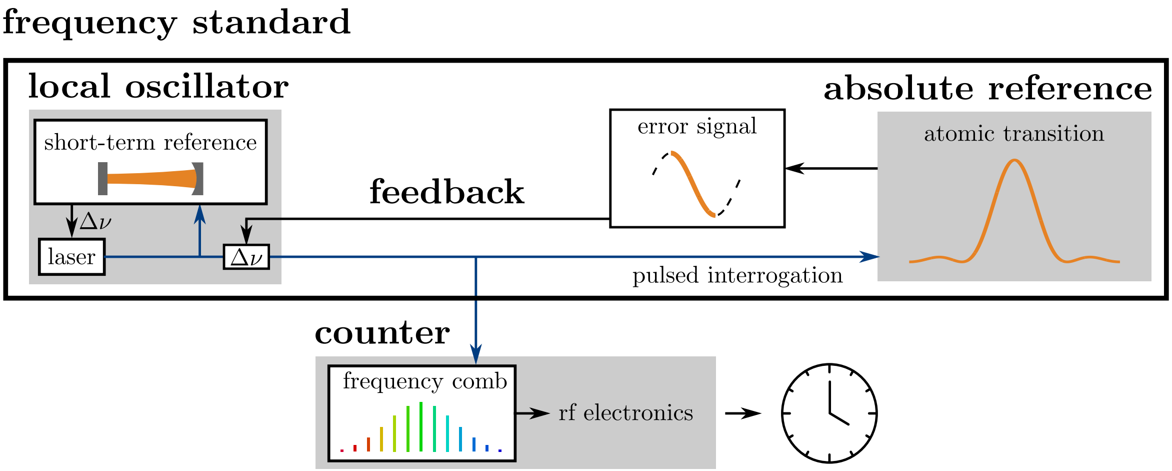

Figure 2.1.: Constituents of a generic passive clock (bold) and their implementation in an optical atomic clock.

with vanishing electric quadrupole moments should be used, as its frequency is insensitive to such gradients. This is the case for the $^1S_0 \leftrightarrow {}^3P_0$ intercombination lines in two-electron systems such as singly ionized group 13 elements, of which boron [37], aluminium [38], indium [39], and thallium [40] have been considered as frequency standards. With increasing mass, the lifetimes of the triplet states decrease due to admixtures of the short-lived $^1P_1$ state in the intermediate coupling regime[1]. Figure 2.2 shows part of the $^{115}\mathrm{In}^+$ term scheme, which presents a good compromise, in that the $^1S_0 \leftrightarrow {}^3P_0$ clock transition is still reasonably narrow (0.82 Hz [30]), whereas the $^1S_0 \leftrightarrow {}^3P_1$ transition is sufficiently wide (360 kHz) for direct state detection. This direct readout can be extended more easily to multiple ions than more complex detection strategies as required, e.g. for Al^+ [43–45]. Further favorable properties of indium as reference for a clock include the low sensitivity of the clock transition to electric [29] and magnetic [30] fields, and the high mass, which results in a reduced time dilation shift for a given kinetic energy. In addition, the clock transition wavelength of 236.5 nm coincides with the fourth harmonic of an Nd:YAG laser at 946 nm, which is advantageous due to the high intrinsic frequency stability of solid state lasers. An overview of expected frequency uncertainties in an indium clock can be found in [28] and in Ch. 7.

Although indium has been directly cooled on the $^1S_0 \leftrightarrow {}^3P_1$ transition [39], the narrow linewidth only allows low cooling rates. With a width of 159 MHz, the $^1S_0 \leftrightarrow {}^1P_1$ electric dipole transition would be an alternative, but its wavelength in the vacuum-UV range is technically challenging [46]. The approach followed here is sympathetic cooling with $^{172}\mathrm{Yb}^+$,

---

[1] For the $^3P_0$ state, decay to the ground state occurs due to hyperfine-induced admixtures of the $^3P_1$ and $^1P_1$ states [41, 42].

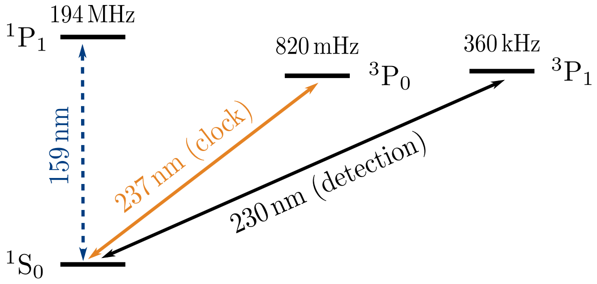

Figure 2.2.: Reduced term scheme of ^{115}In$^+$. ^{115}In has a nuclear spin of $I = 9/2$; the hyperfine structure is omitted for clarity.

chosen for its convenient level scheme (see Ch. 3) and favorable mass ratio [47].

2.1.3. Instability of a multi-ion frequency standard

The fundamental limit of attainable instability in an optical clock based on a single ion is discussed in a number of publications (see, e.g. [48–50]). This section reviews the common result, for the case of multiple simultaneously interrogated ions. Since the goal is to find the limitation due to the atomic reference, an ideal LO is assumed at first.

Frequency corrections to the LO are determined by pulsed interrogation of the atomic resonance between two states denoted by $|g\rangle$ and $|e\rangle$. The two common schemes determine the resonance frequency either from the excitation probability after a single pulse (Rabi scheme) or from the phase evolution of a superposition $(|g\rangle + e^{i\varphi}|e\rangle)/\sqrt{2}$ (Ramsey scheme [51]). An error signal is then derived from the difference in excitation probability when probing at two different detunings around the resonance (Rabi) or with different relative phase shifts (Ramsey):

$$D(\nu) = (p_+(\nu) - p_-(\nu))\, N_{\text{ions}} \frac{N_{\text{cycles}}}{2} \,, \tag{2.1}$$

where $p_\pm$ is the excitation probability under the two different conditions, N_{ions} the number of ions, and N_{cycles} the number of measurements before the correction is applied. The uncertainty of the frequency determination thus depends on the uncertainty of the population measurements and the error signal discriminator slope:

$$\sigma_\nu = \frac{\sigma_p}{|\partial D/\partial \nu|} \,, \tag{2.2}$$

where it has been assumed that close to resonance, $\sigma_{p_+} \approx \sigma_{p_-} \approx \sigma_p$. Detection is typically performed with the electron shelving technique [52], where ions in $|g\rangle$ are revealed by light scattered on a broad cycling transition, whereas ions in $|e\rangle$ stay dark. This way, the signal from a single excitation on the clock transition is amplified by the large number of photons scattered by ions in $|g\rangle$, and the technical uncertainty due to state detection becomes negligible.

The uncertainty σ_p is instead limited by a more fundamental process termed quantum projection noise (QPN) [53], which is caused by the fact that each ion is projected onto either the ground or excited state by the measurement process. The uncertainty of a single experiment $\sigma_{p,1}$ can be determined from the variance of the respective projection operator $\hat{P}$ as $\sigma_{p,1} = \sqrt{p(1-p)}$, where p is the expectation value of $\hat{P}$. For N_cycles interrogations of an ensemble of N_ions independent ions, the overall uncertainty is that of a binomial distribution: $\sigma_p = \sqrt{N_\text{cycles} N_\text{ions} p(1-p)}$.

The QPN limited frequency uncertainty is thus

$$\sigma_y = \frac{\sigma_\nu}{\nu} = \frac{\sqrt{N_\text{cycles} N_\text{ions} p(1-p)}}{\nu\, |\partial D/\partial\nu|} = \frac{1}{\kappa} \frac{\Delta\nu}{\nu} \frac{1}{\sqrt{N_\text{ions}}} \sqrt{\frac{t}{\tau}}\,, \tag{2.3}$$

where $\Delta\nu$ denotes the clock transition full width at half-maximum (FWHM), τ the total time, $t = \tau/N_\text{cycles}$ is the period of a single interrogation, and κ is a numerical factor of order unity that depends on the details of the interrogation scheme.

While σ_p vanishes for $p = 0$ or 1, so does the frequency sensitivity of the error signal. In the presence of other noise processes, the optimal choice of probe parameters is therefore around $p = 0.5$, where the frequency sensitivity is maximized at the cost of a maximized QPN contribution. Another parameter to be optimized is the interrogation time t. An increase is advantageous as long as the interrogation is Fourier-limited, since $|\partial D/\partial\nu|$ will increase linearly with t, whereas the adverse effect of reducing N_cycles in a given interval only increases $\sigma_y \propto \sqrt{t}$. The interrogation time is ultimately limited by the reduction of contrast due to excited state decay. Numerical optimization of the parameters shows that Ramsey interrogation results in slightly lower uncertainties than Rabi interrogation, and that the optimal free phase evolution time is the inverse of the excited state decay rate $1/\Gamma$ [50]. For the ${}^1\mathrm{S}_0 \leftrightarrow {}^3\mathrm{P}_0$ transition in ${}^{115}\mathrm{In}^+$ ($\Gamma = 2\pi \times 0.82\,\mathrm{Hz}$), this means $t = 195\,\mathrm{ms}$ and $\kappa \approx 0.39$. The resulting instabilities are shown in Fig. 2.3. Note that this estimate neglects a possible loss of contrast in the $\pi/2$ pulses due to motional dephasing as explained in section 2.3.

2.1.4. Local oscillator requirements

Frequency noise of the LO can prevent a frequency standard from reaching a QPN limited instability in various ways. Most importantly, the phase difference between the reference and LO must not exceed $\pm\pi$ within the interrogation period to prevent ambiguity of the outcome ("cycle slips"). With state of the art clock lasers, this requirement limits the interrogation

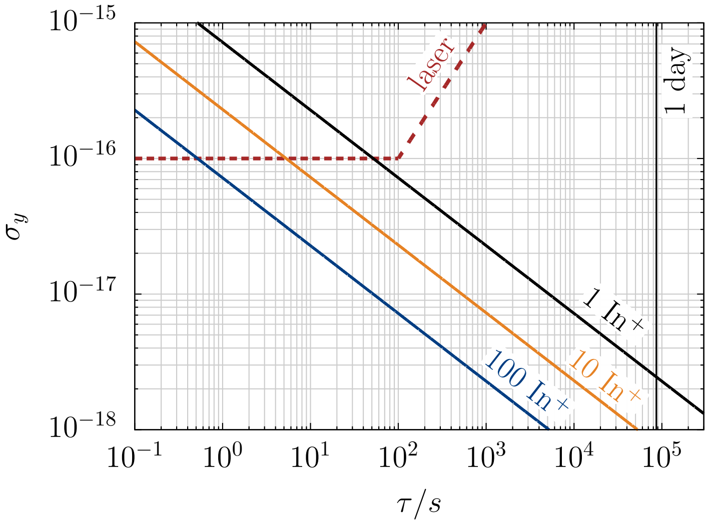

Figure 2.3.: QPN limited instabilities for a single ^{115}In$^+$ ion and the improvement achievable by interrogating 10 and 100 ions simultaneously. While almost 6 days of averaging are necessary to reach 1×10^{-18} with a single ion, the same instability could be reached in less than 90 min with 100 ions. The trace labeled “laser” illustrates the local oscillator requirements as discussed in section 2.1.4

period to less than the optimal time $1/\Gamma$ for clock transitions with long lived excited states, such as in Yb$^+$ (E3) and Al$^+$. In the case of ^{115}In$^+$, the risk of cycle slips within the relatively short optimal interrogation time of $t \approx 0.2\,\mathrm{s}$ is negligible as long as the fractional LO frequency instability $\sigma_y(t) \ll 1 \times 10^{-14}$. However, a much stricter condition is imposed by the requirement that until sufficient data for frequency feedback has been collected, the intrinsic instability of the LO must be below the QPN limit.

This last condition reveals a major advantage of the multi-ion approach: Since the amount of information obtained within a single interrogation is increased by N_{ions}, feedback can be applied at an increased rate. Assuming that at most two interrogations are necessary with $N_{\mathrm{ions}} = 100$, this means that an LO instability of $\sigma_y(400\,\mathrm{ms}) = 1 \times 10^{-16}$ is sufficient for QPN limited operation. While according to Eq. 2.3, the QPN limit of a single-ion standard could instead be improved by the use of a narrower clock transition, the feedback time constant on the order of seconds would require an LO instability in the low 10^{-17} range on that timescale to achieve the same performance.

The above derivations showed an instability scaling $\sigma_y \propto 1/\sqrt{N_{\mathrm{ions}}}$ for an ensemble of independent ions. This can be improved upon by the use of correlations, i.e. with nonclassical states, where the optimal scaling is given by the Heisenberg limit $\sigma_y \propto 1/N_{\mathrm{ions}}$ [54]. An intuitive example is the use of a maximally entangled (Greenberger-Horne-Zeilinger) state of N_{ions} ions $(|g \dots g\rangle + |e \dots e\rangle)/\sqrt{2}$, where the energy difference between the two components is $N_{\mathrm{ions}}(E_e - E_g)$. The resulting speed-up in phase evolution increases the discriminator slope in the denominator of (2.3) by a factor of $\sqrt{N_{\mathrm{ions}}}$. However, if the interrogation is limited by the excited state lifetime as assumed above, the loss of contrast due to the increased decoherence rate of such a state exactly cancels the improvement [55]. This is different if decoherence is

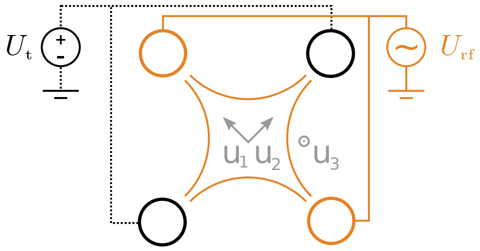

Figure 2.4.: Schematic view of the radial plane in a linear Paul quadrupole trap with asymmetric rf drive. The constant voltage U_t is applied in order to break the rotational symmetry of the radial confinement in a controlled way.

limited by correlated noise, e.g. due to LO frequency fluctuations, where an improved scaling with atom number can be achieved with nonclassical states [56, 57]. If the probe period is limited by the risk of cycle slips, cascading interrogations of increased duration to keep track of the phase can also lead to an enhanced scaling with N_{ions} [58, 59].

2.2. Motion of ion Coulomb crystals in a Paul trap

By placing no technical restrictions on the interrogation time, the above section implicitly assumed the confinement of the reference ions. In addition, spectroscopy on trapped particles has the advantage of reducing the volume in which external influences on the energy levels need to be suppressed and being able to monitor and control the motional state with high precision. This section reviews the principle of rf confinement and ion motion in a Paul trap.

2.2.1. Single ion equations of motion

Three-dimensional harmonic confinement of a particle along the directions $u_{1...3}$ requires a potential

$$\Phi = \sum_{i=1}^{3} \alpha_i u_i^2 \, . \tag{2.4}$$

For a static electric potential in a charge-free region, the Laplace equation $\Delta\Phi = 0$ imposes the condition $\alpha_1 + \alpha_2 + \alpha_3 = 0$, which leads to repulsion in at least one direction – a phenomenon known as Earnshaw's theorem [60]. Paul traps [25, 26] circumvent this issue with the use of an oscillating inhomogeneous field. For particles displaced from the trap center, the inhomogeneity leads to an imbalance between the electric field contributions from each half of the oscillation period that produces a net force toward the equilibrium position.

The trap geometry most suitable for the storage of linear ion crystals is the linear Paul trap, in which rf confinement is only used in the u_1,u_2 plane and the Laplace equation is fulfilled by setting $\alpha_2 = -\alpha_1$, $\alpha_3 = 0$. The radial plane of such a trap is shown schematically in Fig. 2.4. Near the center, the potential can be approximated by

$$\Phi_{\text{rad}} = (\kappa_{\text{rf}}\, U_{\text{rf}} \cos(\Omega_{\text{rf}} t) - \kappa_{\text{dc}}\, U_{\text{t}})\, \frac{u_1^2 - u_2^2}{2d} \, , \tag{2.5}$$

where d denotes the distance between the electrodes and the center, the factors κ are geometric corrections of order unity and a weak static quadrupole potential has been added using the constant voltage $U_t \approx 10^{-3} \times U_{\mathrm{rf}}$ in order to introduce a controlled anisotropy.

Along u_3, a harmonic trapping potential with trap frequency ω_{ax} is provided by a static electric field. By axially dividing the rf ground electrodes (shown in Fig. 2.4 in black) into separate segments, multiple independent trapping regions can be formed. According to Earnshaw's theorem, this potential must have a repulsive effect in the radial directions and thereby (slightly) weaken the radial confinement.

It is common to define the dimensionless parameters

$$q_1 = -q_2 = \frac{2e\kappa_{\mathrm{rf}} U_{\mathrm{rf}}}{md^2\Omega_{\mathrm{rf}}^2} \ , \quad q_3 = 0 \ , \tag{2.6}$$

$$a_{1,2} = -\frac{2\omega_{\mathrm{ax}}^2}{\Omega_{\mathrm{rf}}^2} \pm \frac{4e\kappa_{\mathrm{dc}} U_{\mathrm{t}}}{md^2\Omega_{\mathrm{rf}}^2} \quad \text{and} \quad a_3 = \frac{4\Omega_{\mathrm{rf}}^2}{\omega_{\mathrm{ax}}^2} \ , \tag{2.7}$$

with which the equations of motion for a particle of mass m and charge e can be written as (see, e.g. [61])

$$\ddot{u}_i + (a_i + 2q_i \cos(\Omega_{\mathrm{rf}} t)) \frac{\Omega_{\mathrm{rf}}^2}{4} u_i = \frac{eE_{\mathrm{dc},i}}{m} \ . \tag{2.8}$$

This is the inhomogeneous form of the Mathieu differential equation. The term on the right-hand side represents the influence of an external stray field E_{dc}, which is generally unwanted, as explained below. The existence of finite solutions to Eq. 2.8 depends on the choice of a_i and q_i. Confinement of particles is therefore only possible in certain stability regions within the (a,q) parameter space.

Like the majority of Paul traps, the trap used in this work is operated in the stability region closest to the origin. Under the condition $|a_i|, |q_i| \ll 1$, the inhomogeneity of the electric field within the amplitude of motion at Ω_{rf} can be neglected. This is known as the adiabatic approximation, since it leads to a solution to (2.8) for which the kinetic energy in the directions of rf confinement is almost constant in time [61]:

$$u_i(t) = (u_{0,i} + u_{1,i} \cos(\omega_i t)) \left(1 + \frac{q_i}{2} \cos(\Omega_{\mathrm{rf}} t + \varphi_i)\right) \tag{2.9}$$

$$\text{with} \quad \omega_i = \frac{\Omega_{\mathrm{rf}}}{2} \sqrt{a_i + \frac{q_i^2}{2}} \ . \tag{2.10}$$

Equation 2.9 consists of motion at two distinct frequencies: The harmonic oscillation at ω_i is referred to as *secular motion*, whereas the fast oscillations with Ω_{rf} are called *micromotion.* Two separate contributions to micromotion can be distinguished. The term with an amplitude $\propto u_{1,i} \cos(\omega_i t)$ is caused by periodic excursions from the potential minimum during the secular oscillation at ω_i. This motion, which is referred to as *intrinsic micromotion* (IMM), is a fundamental feature of the Paul trap: its mean kinetic energy is the effective ponderomotive potential energy. While the amplitude can therefore never vanish entirely, it can be reduced by decreasing the amplitude of the secular motion, i.e. by cooling. The micromotion component $\propto u_{0,i}$ is referred to as *excess micromotion* (EMM). It is caused by a residual rf field $\vec{E}_{\mathrm{rf}}$ at the potential minimum, which can exist either due to a phase shift between the rf electrodes or a residual static electric field $\vec{E}_{\mathrm{dc}}$ [32]. The measurement of EMM and its compensation is explained in detail in Ch. 6.

In order to obtain decoupled equations of motion in the radial plane, it has been assumed that the principal axes of the radial potential are oriented along u_1 and u_2. In the more general case of arbitrarily oriented principal axes, there can be a micromotion component perpendicular to the secular motion displacement.

With the exception of Ch. 6, effects of the rf confinement are neglected and the trapping potential is treated as a simple harmonic "pseudo"potential in this thesis. This includes the use of static harmonic oscillator wavefunctions. An exact treatment would result in time dependent wavefunctions with a "breathing" motion at Ω_{rf}, which, e.g. reduces the coupling to light fields, but these effects are negligible as long as $|q_i| \ll 1$ [62].

2.2.2. Normal mode spectrum of a mixed-species crystal

When multiple ions are trapped simultaneously, the Coulomb interaction between their charges modifies the effective trapping potentials. Crystalline structures form when the average kinetic energy is cooled below the interaction energy. For small excursions from its equilibrium configuration, the motion of an N-ion Coulomb crystal can be expressed in terms of its N eigenmodes per dimension. The following derivation of the mode spectrum follows [63], which treats the most general case of an arbitrary arrangement of ions with different masses. Similar derivations can be found in [64, 65]; a treatment without the pseudopotential approximation is presented in [66].

The description is simplified by restricting it to linear crystals along the $z = u_3$ axis. This alignment can be ensured with an anisotropic trapping potential with aspect ratio $\omega_{x,y}/\omega_z \gtrsim 0.73N^{0.86}$ [67]. The first step is to find the axial equilibrium positions by minimizing the potential energy

$$V_{\mathrm{ax}} = \sum_{i=1}^{N} \frac{1}{2} m_i \omega_{\mathrm{ax}}^2 z_i^2 + \frac{1}{2} \sum_{i,j=1,i\neq j}^{N} \frac{e^2}{4\pi\varepsilon_0} \frac{1}{|z_i - z_j|} \tag{2.11}$$

Rewriting the ion coordinates in terms of small deviations from the equilibrium positions

$z_{0,i}$: $z_i(t) = z_{0,i} + q_i(t)$ and expanding the potential to 2nd order in q_i simplifies (2.11) to

$$V \approx \frac{1}{2}\sum_{i,j=1}^{N} q_i q_j \left[\frac{\partial^2 V}{\partial z_i \partial z_j}\right]_0 = \frac{1}{2}\sum_{i,j=1}^{N} q_i q_j V_{ij} \tag{2.12}$$

with

$$V_{ij} = \begin{cases} m_i\omega_{\mathrm{ax},i}^2 + \sum_{k=1,k\neq i}^{N} \frac{e^2}{2\pi\varepsilon_0} \left|z_{0,i} - z_{0,k}\right|^{-3} & \text{for} \quad i = j \\ \\ -\frac{e^2}{2\pi\varepsilon_0} \left|z_{0,i} - z_{0,j}\right|^{-3} & \text{for} \quad i \neq j\ . \end{cases} \tag{2.13}$$

For the radial directions, the same approach is used with the displacement perpendicular to the axis. Using the fact that for a linear chain $x_{0,i} = y_{0,i} = 0$ leads to

$$V_{ij} = \begin{cases} m_i\omega_{\mathrm{rad},i}^2 - \sum_{k=1,k\neq i}^{N} \frac{e^2}{4\pi\varepsilon_0} \left|z_{0,i} - z_{0,k}\right|^{-3} & \text{for} \quad i = j \\ \\ \frac{e^2}{4\pi\varepsilon_0} \left|z_{0,i} - z_{0,j}\right|^{-3} & \text{for} \quad i \neq j\ . \end{cases} \tag{2.14}$$

There are two notable differences from the axial case. In a linear trap, $m_i\omega_{\mathrm{ax},i}^2$ is purely due to a static electric field and only depends on the charge. The corresponding rf confinement term, however, is mass dependent ($\propto m_i^{-1}$). In a mixed-species crystal, $m_i\omega_{\mathrm{rad},i}^2$ therefore takes different values for the individual ions. The second difference is the change in sign of the Coulomb interaction term, which reflects that a radial displacement increases the distance to all neighboring ions.

The normal modes of motion are obtained by finding the eigenvectors β_α of V:

$$\sum_{j=1}^{N} V_{ij}\beta_{\alpha,j} = \lambda_\alpha m_i \beta_{\alpha,i}\ , \tag{2.15}$$

where $\alpha = 1 \ldots N$ and the mode eigenfrequencies $\omega_\alpha = \sqrt{\lambda_\alpha}$ are real valued for stable crystal configurations.

For a single-species crystal, there is a mode for each dimension in which the center of mass (COM) oscillates at the single-ion trap frequency, while the relative ion displacements stay fixed. While the axial higher-order modes have higher frequencies than the COM mode, the mode frequencies decrease for the radial direction due to the different sign of the Coulomb term in Eq. 2.14.

A given set of ion displacements can be expressed as a set of normal mode excitations by a transformation into the $\{\beta_\alpha\}$ basis

$$\pi_\alpha = \sum_{i=1}^{N} \beta_{\alpha,i} q_i = \sqrt{\frac{\hbar}{2\omega_\alpha}} \left(\hat{a}_\alpha + \hat{a}_\alpha^\dagger\right) \ , \tag{2.16}$$

where in the second step, the annihilation operator $\hat{a}_\alpha$ of the mode has been introduced. If all ions have identical masses, the eigenvectors β_α are mutually orthogonal. This is not true for mixed-species crystals, since the energy corresponding to a given displacement is mass-dependent. In that case, a set of orthogonal eigenvectors β'_α can be obtained by defining mass-weighted displacements $q'_i = \sqrt{m_i} q_i$ and replacing $V_{i,j}$ by $V'_{i,j} = V_{i,j}/\sqrt{m_i m_j}$.

2.3. Interaction of trapped ions with light

Ion traps can provide strong confinement, in the sense that the energy spacing of motional states can be significantly higher than the natural width of an optical transition of interest. Under these conditions, the coupling between the electronic and motional degrees of freedom by electromagnetic radiation can be used to both investigate and manipulate the dynamics of trapped ions at the level of single quanta of motion. The following section briefly summarizes the fundamental processes of this interaction. More comprehensive derivations can be found, e.g., in [62, 68, 69].

For simplicity, the discussion is restricted to a two-level atom with states $|g\rangle$ and $|e\rangle$ of energy difference $\hbar\omega_0$ in a 1-dimensional trap with secular frequency ω_{sec}. Setting the internal and external ground state energies to 0, the corresponding Hamiltonian in the absence of light can be written as

$$\hat{H}_0 = \hat{H}_{\text{ion}} + \hat{H}_{\text{trap}} = \hbar\omega_0 |e\rangle\langle e| + \hbar\omega_{\text{sec}} \hat{a}^\dagger \hat{a} \ , \tag{2.17}$$

with the harmonic oscillator annihilation operator $\hat{a}$. An external field $E(t) = E_0 \cos(\omega_{\text{L}} t + k_x \hat{x})$ adds the interaction

$$\hat{H}_{\text{int}} = \frac{1}{2}\hbar\Omega_0^{(\text{int})} \left(|e\rangle\langle g| + |g\rangle\langle e|\right) \left(e^{i(\omega_{\text{L}} t + k_x \hat{x})} + e^{-i(\omega_{\text{L}} t + k_x \hat{x})}\right) \ , \tag{2.18}$$

where the free ion Rabi frequency $\Omega_0^{(\text{int})} \propto E_0$ contains the details of the electronic transition and $k_x = (2\pi/\lambda)\cos\theta$ is the x component of the wave vector. Changing into the interaction picture with respect to $\hat{H}_0$ and neglecting terms which oscillate at $2\omega_0$ yields

$$\hat{H}' = e^{i\hat{H}_0 t/\hbar} \hat{H}_{\text{int}} e^{-i\hat{H}_0 t/\hbar} = \frac{1}{2}\hbar\Omega_0^{(\text{int})} \times e^{i\omega_{\text{sec}} t \hat{a}\hat{a}^\dagger} \left(|e\rangle\langle g| e^{-i(\Delta t - k_x \hat{x})} + \text{H.c.}\right) e^{-i\omega_{\text{sec}} t \hat{a}^\dagger \hat{a}} \ , \tag{2.19}$$

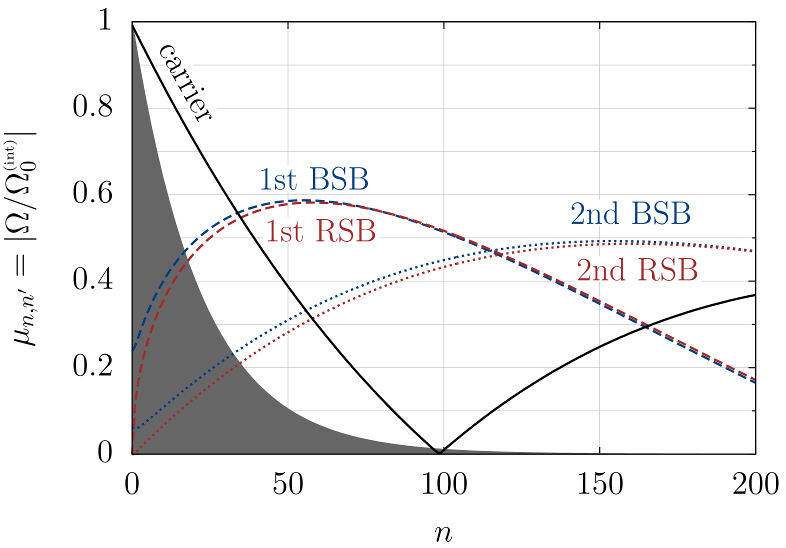

Figure 2.5.: Motional state dependence of the Rabi frequencies for the 411 nm transition in ^{172}Yb$^+$ and $\omega_{\mathrm{sec}} = 2\pi \times 470\,\mathrm{kHz}$ ($\eta = 0.12$). The shaded region illustrates the thermal occupation of states at the Doppler limit of 0.5 mK.

with $\Delta = \omega_{\mathrm{L}} - \omega_0$. The transition matrix element for an electronic excitation with simultaneous change from the harmonic oscillator state $|n\rangle$ to $|n'\rangle$ is

$$\langle n', e|\hat{H}'|n, g\rangle = \frac{1}{2}\hbar\Omega_0^{(\mathrm{int})} \left\langle n' \left| e^{ik_x\hat{x}} \right| n \right\rangle e^{i[\Delta+(n'-n)\omega_{\mathrm{sec}}]t} \;. \tag{2.20}$$

The exponential term shows that to fulfill energy conservation, the resonance is now shifted by the difference in motional energy $\hbar\omega_{\mathrm{sec}}(n' - n)$. The case $n' = n$ is referred to as the *carrier* transition, whereas transitions which change the motional state are termed either *red* ($n' < n$) or *blue* ($n' > n$) *sidebands.*

The relative transition strength is scaled by the motional overlap integral $\langle n'|e^{ik_x\hat{x}}|n\rangle = \mu_{n,n'}$, where the operator $e^{ik_x\hat{x}}$ represents the momentum transfer from the interaction with a photon. Expressing the position operator in terms of $\hat{a}$ and the groundstate wavefunction spread x_0 as $\hat{x} = x_0(\hat{a} + \hat{a}^\dagger)$ allows an evaluation of the integral [68]:

$$\mu_{n,n'} = \langle n'|e^{ik_x x_0(a+a^\dagger)}|n\rangle = \langle n'|e^{i\eta(a+a^\dagger)}|n\rangle = e^{-\frac{1}{2}\eta^2}\sqrt{\frac{n_<!}{(n_< + \Delta n)!}}(i\eta)^{\Delta n} L_{n_<}^{\Delta n}\left(\eta^2\right) \;, \tag{2.21}$$

where $\Delta n = |n' - n|$, $n_<$ is the lesser of the two values and $L_n^\alpha(x)$ is a generalized Laguerre polynomial. Figure 2.5 shows the dependence of $\mu_{n,n'}$ on n for the carrier and the first two red (RSB) and blue (BSB) sidebands of the $^2\mathrm{S}_{1/2} \leftrightarrow {}^2\mathrm{D}_{5/2}$ transition in ^{172}Yb$^+$ at 411 nm. The motional state of a Doppler cooled ion is a mixed state with a thermal energy distribution over the trap levels. For the Doppler limit of ^{172}Yb$^+$ at 0.5 mK, this distribution is shown by the shaded area.

Equation 2.21 introduced the Lamb-Dicke parameter [70]

$$\eta = k_x x_0 = k\cos(\theta)\sqrt{\frac{\hbar}{2m\omega_{\mathrm{sec}}}} = \cos(\theta)\sqrt{\frac{\omega_{\mathrm{r}}}{\omega_{\mathrm{sec}}}}\ , \tag{2.22}$$

which quantifies the influence of the light field on the motional state. It depends on the extension of the groundstate wavefunction with respect to the laser wavelength, which determines the electric field gradient over the extension of the ion and thereby the strength of the dipole force exerted by the light. Alternatively, η^2 can be interpreted as the ratio of the photon recoil energy $\hbar\omega_{\mathrm{r}}$ to the trap level energy spacing $\hbar\omega_{\mathrm{sec}}$. A motional state $|n\rangle$ is considered to be in the Lamb-Dicke regime when

$$\eta^2(2n+1) \ll 1\ , \tag{2.23}$$

such that the exponential in Eq. 2.21 can be replaced by a 1st-order approximation in $\eta(\hat{a}+\hat{a}^\dagger)$ and sideband transitions of order $|\Delta n| > 1$ can be neglected. This is an important regime for spectroscopy, since under this condition, the 1st-order Doppler effect on the carrier transition can be neglected [71].

An extension of the above derivation to multiple motional modes is straightforward. Each mode introduces new sidebands and an additional factor μ which reduces the transition strength. For Coulomb crystals, the Lamb-Dicke parameter of mode α for ion i can be calculated from the quantities derived in 2.2.2 as [63]:

$$\eta_{\alpha,i} = k\beta'_{\alpha,i}\sqrt{\frac{\hbar}{2m_i\omega_\alpha}}\cos(\theta), \tag{2.24}$$

where θ is the angle between $\vec{k}$ and the trap principal axis of the mode. The resulting distribution of Rabi frequencies leads to a loss of contrast due to the dephasing of Rabi oscillations when a thermal ensemble is probed. Since the carrier transition is affected as well, every mode with a projection onto $\vec{k}$ contributes to this effect. If N modes contribute, the excited state population after a pulse of length t is

$$\rho_{ee} = \sum_{n_1,\ldots,n_N=0}^{\infty}\left(\prod_{\alpha=1}^{N} P_\alpha(n_\alpha)\right)\sin^2\left(\Omega_0^{(\mathrm{int})} t \prod_{\alpha=1}^{N}\mu_{n_\alpha,n'_\alpha}\right)\ , \tag{2.25}$$

where $P_\alpha(n_\alpha)$ is the thermal occupation of state n_α.

The loss of coupling strength due to the motional overlap integrals of “spectator” modes has first been described in the context of x-ray spectroscopy of solids, where it is known as the Debye-Waller effect [72]. Due to the N-dimensional sum, the computational effort in calculating (2.25) quickly becomes unreasonable for an increasing number of contributing modes. If all of the modes are deep in the Lamb-Dicke regime, the expression can be simplified significantly [73, App. 1], but this approximation fails for modes where terms of order n^2 cannot be neglected. Another approach is to calculate the mean and root mean square (rms) Rabi frequencies in order to estimate the loss of contrast [69]. This treatment shows that a high number of high-frequency normal modes is favorable, since it narrows the overall Rabi frequency distribution. Low-frequency modes, however, are detrimental due to their large Lamb-Dicke factors. This can become an issue when radial modes are involved.

2.3.1. Motional frequency shifts

If secular motion is cooled to the Lamb-Dicke regime and the micromotion amplitudes are well below the wavelength of the interrogated transition, the 1st-order Doppler effect due to ion motion has negligible influence on the carrier transition frequency. The carrier is however shifted by the 2nd-order Doppler effect, which arises due to relativistic time dilation with respect to the laboratory reference frame. The relative frequency shift can be expressed as the ratio between kinetic energy E_{kin} and rest energy [74]:

$$\frac{\Delta\nu_{\mathrm{2D}}}{\nu} = -\frac{E_{\mathrm{kin}}}{mc^2} \, . \tag{2.26}$$

Under the assumption that the static contribution to the radial trapping potential is negligible ($a_i \ll q_i^2$), IMM effectively doubles the kinetic energy in the radial degrees of freedom. The mean kinetic energy from thermal excitation is therefore

$$\langle E_{\mathrm{kin,th}} \rangle = \frac{1}{2} k_B T_{\mathrm{axial}} + k_B T_{\mathrm{radial,1}} + k_B T_{\mathrm{radial,2}} \approx \frac{5}{2} k_B T \, . \tag{2.27}$$

Combined with the kinetic energy due to EMM,

$$\langle E_{\mathrm{kin,EMM}} \rangle = \frac{m}{2} \langle v_{\mathrm{EMM}}^2 \rangle = \frac{1}{m} \left(\frac{e}{2\Omega_{\mathrm{rf}}} E_{\mathrm{rf}} \right)^2 , \tag{2.28}$$

the total 2nd-order Doppler shift is

$$\left\langle \frac{\Delta\nu_{\mathrm{2D}}}{\nu} \right\rangle = -\frac{\langle E_{\mathrm{kin}} \rangle}{mc^2} = -\frac{5 k_B T}{2mc^2} - \left(\frac{e}{2mc\Omega_{\mathrm{rf}}} E_{\mathrm{rf}} \right)^2 \, . \tag{2.29}$$

Both contributions in Eq. 2.29 are addressed within this thesis. For an $^{115}\mathrm{In}^+$ ion sympathetically cooled to Doppler limit of Yb^+ at 0.5 mK, the thermal contribution is -1.0×10^{-18}. Precise knowledge of the temperature is therefore necessary to reduce the frequency uncertainty due to this term. Since cooling during clock interrogation should be avoided due to the risk of AC Stark shifts, low external heating rates are vital. Spectroscopic methods for measuring temperature are introduced in the next section, and their experimental implementation, including a measurement of the heating rates, is shown in Ch. 5. Measurement and minimization of the micromotion contribution to below 10^{-19} is discussed in Ch. 6.

2.3.2. Spectroscopic temperature determination

The dependence of coupling strength on the motional state allows a determination of the ion temperature from spectroscopic signals. Depending on the temperature range, as quantified below by the mean phonon number $\bar{n}$, different schemes provide the most sensitive signals.

Deep Lamb-Dicke regime, $\bar{n} \approx 0$

The most straightforward determination of $\bar{n}$ is possible close to the quantum ground state. Rewriting the thermal distribution in terms of n and $\bar{n}$ as [75]

$$P_n(\bar{n}) = \frac{1}{\bar{n}+1}\left(\frac{\bar{n}}{\bar{n}+1}\right)^n , \tag{2.30}$$

equation 2.25 can be expressed as

$$\rho_{ee}^{(\Delta n)} = \frac{1}{\bar{n}+1}\sum_{n=0}^{\infty}\left(\frac{\bar{n}}{\bar{n}+1}\right)^n \sin^2\left(\Omega_0^{(\text{int})} t\, \mu_{n,n+\Delta n}\right) , \tag{2.31}$$

where only a single motional mode is considered for clarity. Assuming $\Delta n > 0$, Eq. 2.31 represents a blue sideband of order Δn. Due to the fact that $|\mu_{n,n'}| = |\mu_{n',n}|$, the corresponding red sideband excitation probability can be written as

$$\rho_{ee}^{(-\Delta n)} = \left(\frac{\bar{n}}{\bar{n}+1}\right)^{\Delta n} \rho_{ee}^{(\Delta n)} . \tag{2.32}$$

The ratio of excitations on the two sidebands can therefore be used to determine $\bar{n}$, regardless of $\Omega_0^{(\text{int})}$ and t:

$$\bar{n} = \left[\sqrt[\Delta n]{\frac{\rho_{ee}^{(+\Delta n)}}{\rho_{ee}^{(-\Delta n)}}} - 1\right]^{-1} . \tag{2.33}$$

The advantage of this method is that knowledge of the Lamb-Dicke parameter, i.e. of the relative orientation between the mode principal axis and $\vec{k}$, is not necessary. As a rule of thumb, the method is most sensitive when the sideband order Δn is chosen close to $\bar{n}$ [76].

Higher temperatures, $\bar{n} \approx 10 \ldots 100$

The above method relies on the difference in thermal occupation of nearby oscillator states and quickly becomes insensitive for $\bar{n} > 1$. It is therefore not suitable, e.g., at the ytterbium Doppler temperature of 0.5 mK, which corresponds to $\bar{n} \approx 20$ in a mode with $\omega = 2\pi \times 500\,\text{kHz}$. If the Lamb-Dicke parameter is known, the temporal evolution of the excited state population can be used to infer the temperature under these conditions. Figure 2.6

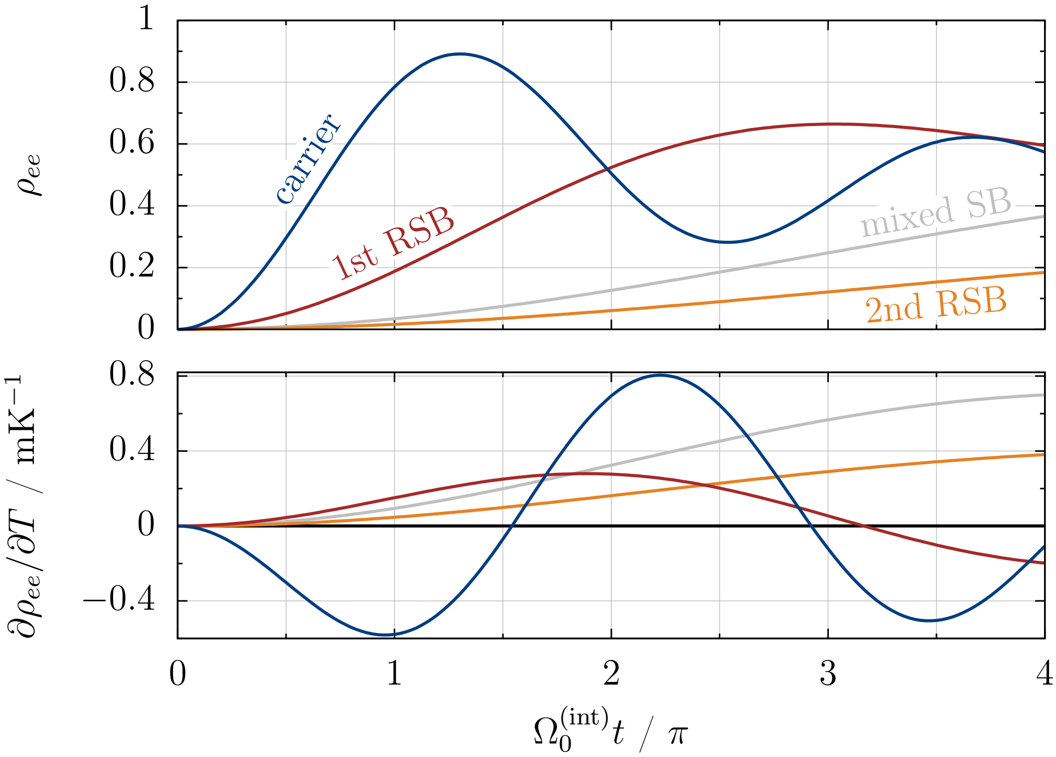

Figure 2.6.: Calculated excited state populations and their temperature derivatives for the experimental parameters of Ch. 5 at $T = 0.5$ mK. Besides the carrier transition, the lowest order sidebands of a mode with $\omega_{\mathrm{sec}} = 2\pi \times 440$ kHz are shown. A second mode with $\omega_{\mathrm{sec}} = 2\pi \times 492$ kHz is assumed to be at the same temperature and has an equal projection onto the laser. The Lamb-Dicke parameters are 0.08 and 0.09, respectively. “mixed SB” refers to the sideband transition which transfers one phonon from the 492 kHz mode to the 440 kHz mode.

shows thermally dephasing Rabi oscillations on the carrier and lowest-order sideband transitions at 0.5 mK according to Eq. 2.25, assuming the experimental configuration of Ch. 5: $\vec{k}$ has a similar projection onto two modes around 470 kHz. Based on these dependencies, a combination of sideband transitions and pulse areas can be chosen in order to maximize the temperature sensitivity. The assumption of equal mode temperatures was made in this example for clarity; a proper choice of sidebands will also allow a distinction between the temperatures of individual modes.

2.4. Crystal configuration considerations for a clock

To illustrate the considerations involved in choosing a crystal configuration for clock spectroscopy, consider the example of a 10-ion crystal consisting of 8 $^{115}\mathrm{In}^+$ clock ions and 2 $^{172}\mathrm{Yb}^+$ cooling ions. It is advantageous to have the heavier ions in the center for a practical reason: Since the ponderomotive potential is stronger for the light ions, the heavy ones leave the linear configuration first when the trap aspect ratio is reduced. This behavior can be used to quickly restore the configuration after ions have switched their positions, e.g. due to a background gas collision. Alternatively, a crystal configuration can be stabilized by heating the eigenmodes of unwanted arrangements [77], but this approach becomes increasingly complex as the number of ions is increased.

The eigenvectors of the radial modes for this configuration are visualized in Fig. 2.7, where the secular frequencies for a single $^{172}\mathrm{Yb}^+$ ion are set to 1.5 MHz (radial) and 330 kHz (axial). Since only $^{172}\mathrm{Yb}^+$ ions interact with the cooling laser, the cooling rate for a mode scales with the relative eigenvector components of those ions. For this reason and due to symmetry considerations, an even number of $^{172}\mathrm{Yb}^+$ ions has been chosen: In odd-numbered ion chains with a symmetric arrangement of masses, there is at least one mode in which the center ion eigenvector component is zero and it does not contribute to cooling at all. Low non-zero eigenvector components of the cooling ions are not an issue as long as external heating rates are negligible compared to the cooling rate, such that the Doppler temperature is reached in equilibrium [47]. As the fluctuating fields responsible for the external heating are likely to be homogeneous over the extension of the crystal, this is mostly a concern for the highest frequency mode, in which all ions move in phase.

Another important parameter is the amount of Coulomb coupling between neighboring ions, which can be adjusted via the trap aspect ratio. In order to optimize sympathetic cooling, the configuration shown here is close to instability, where the coupling is maximized. At an axial frequency of 340 kHz, the equilibrium positions of the $^{172}\mathrm{Yb}^+$ ions would no longer be on the trap axis. A possible downside of this choice is the modification of the radial potential by the Coulomb repulsion. If the radial force due to mutual repulsion cannot be neglected compared to the ponderomotive force, the thermal secular motion of ions will extend further from the rf node, leading to increased IMM amplitudes, i.e. a higher 2nd-order Doppler shift [47, appendix B]. A possible way to avoid this trade-off is to introduce separate cooling and clock interrogation trap configurations. The time consumption of an adiabatic radial potential ramp would be negligible compared to the hundreds of milliseconds of interrogation time.

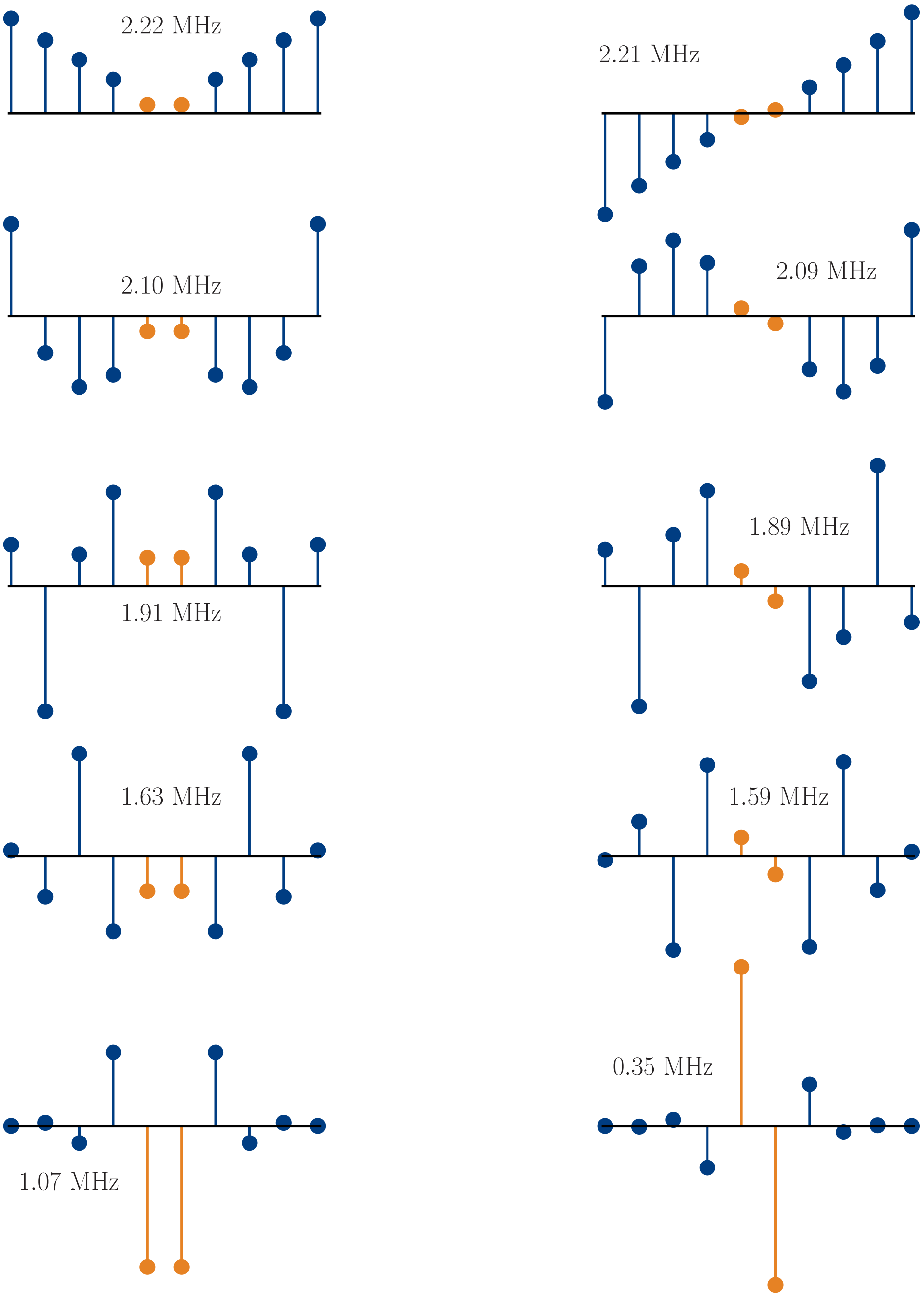

Figure 2.7.: Visualization of the radial normal mode eigenvectors in a 10-ion mixed-species crystal. The blue circles depict $^{115}\mathrm{In}^{+}$ ions, while orange circles symbolize $^{172}\mathrm{Yb}^{+}$. The trap parameters correspond to a radial secular frequency of 1.5 MHz and an axial frequency of 330 kHz for a single $^{172}\mathrm{Yb}^{+}$ ion.

3. Experimental setup

This chapter describes the central components of the experimental apparatus, including the ion trap, spatially resolved electron-multiplying CCD (EMCCD) camera detection and most of the lasers. More specific details are provided in the appropriate places in later chapters.

3.1. The ion trap

A segmented linear Paul trap is used for the confinement of the ion crystals. Since it is developed for clock operation, great effort went into the design [28] and fabrication process [33, 34] in order to allow systematic frequency uncertainties below 1×10^{-18}. All the experiments presented here are performed in an early prototype made from milled wafers of Rogers 4350B$^{\mathrm{TM}}$ printed circuit board material. As shown in Fig. 3.1, the trap consists of four layers, physically implemented as wafers stacked along the x direction. The two innermost wafers contain the rf quadrupole electrodes, whereas the outer layers contain a single set of electrodes solely used for stray field compensation. The trap rf voltage is enhanced by a helical resonator [78]. With the trap connected, its quality factor is 589, at a resonance frequency of $\Omega_{\mathrm{rf}} = 2\pi \times 25.42\,\mathrm{MHz}$. An antenna inside the resonator allows live monitoring of the actual voltage at the electrodes. To avoid the risk of a dielectric breakdown, only about 865 V are applied at the rf electrodes of the prototype trap, yielding radial secular frequencies around $2\pi \times 470\,\mathrm{kHz}$. With the next trap generation made from AlN wafers, the voltage can be safely increased by at least a factor of two. Along the trap axis, the rf ground electrodes are separated into five sections. Axial confinement is provided by dc voltages added to the rf ground electrodes of the neighboring segments. These voltages, along with additional voltages for stray field compensation explained in Ch. 6, are controlled by the experiment control computer using digital-to-analog converters. Since fast switching of the dc voltages is not necessary, they are lowpass filtered with a cutoff frequency of 113 Hz directly on the respective trap wafer. The purpose of this filtering is to reduce resonant heating by fluctuating electric fields at the secular frequencies. Ions are produced by photoionization from beams of neutral atoms from resistively heated ovens. These beams only overlap with a single "loading" trap segment to prevent contamination of the electrodes of the "spectroscopy" segment, in which the experiments are performed.

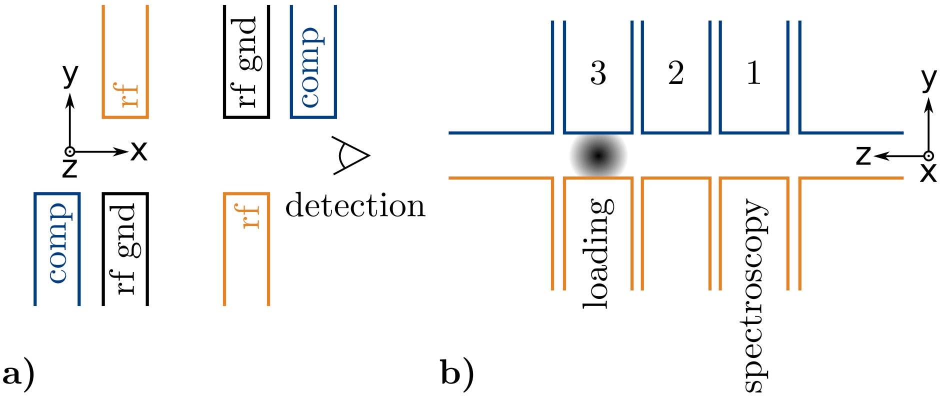

Figure 3.1.: Schematic of the trap electrode geometry (not to scale). **a)** view of the radial plane, showing the rf quadrupole and compensation electrodes. The cross section of the central slit is 1 mm × 1 mm. **b)** side view. The prototype trap consists of three segments, each with a width of 2 mm. To avoid contamination from the neutral atom beams, loading and spectroscopy are performed in separate segments.

3.2. Optical setup

3.2.1. Lasers required for ^{172}Yb^{+}

^{172}Yb^{+} ions are used for sympathetic cooling, trap characterization and for investigating the Coulomb crystal dynamics. Besides having a good mass ratio to sympathetically cool ^{115}In^{+} [47], the species is chosen for its convenient alkali-like level structure, part of which is shown in Fig. 3.2. All of the required transitions can be addressed by (frequency-doubled) diode lasers. The 370 nm $^2S_{1/2} \leftrightarrow {}^2P_{1/2}$ transition has a natural linewidth of $2\pi \times 19.6$ MHz [79] and is used for Doppler cooling and fluorescence detection. The light is produced via the second-harmonic generation (SHG) of a diode laser at 739 nm. Two repumpers are necessary to maintain a closed cooling cycle. A laser at 935 nm clears out the $^2D_{3/2}$ state, which is populated by decay from the $^2P_{1/2}$ state. Collisions with background particles can populate the long-lived $^2F_{7/2}$ state [80], which is cleared out with radiation at 639 nm. As shown in section 5.3.2, this clearout is more efficient when the $^2D_{5/2}$ state is simultaneously depleted via the transition to the $^2P_{3/2}$ state at 1650 nm, in order to prevent cycling. The electric quadrupole transition from the ground state to the $^2D_{5/2}$ state at 411 nm has a natural linewidth of $2\pi \times 23$ Hz [81] and is used for sideband spectroscopy and groundstate cooling.

Isotope-selective photo-ionization of ytterbium is achieved by first exciting the neutral atoms to the $4f^{14}6s6p\,{}^1P_1$ state with radiation at 399 nm and then beyond the ionization threshold with a photon at 370 nm. The light at 399 nm is produced by SHG of a diode laser at 798 nm. Details about the states and transitions involved in both photo-ionization process

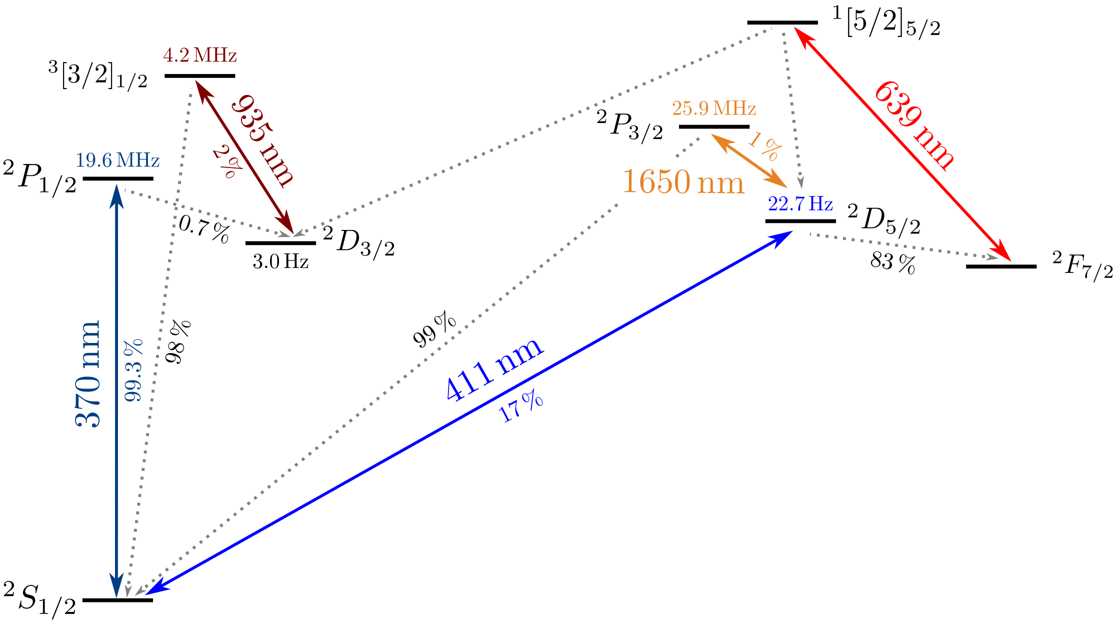

Figure 3.2.: Reduced term scheme of ^{172}Yb$^+$, showing transition wavelengths, linewidths and branching ratios. See appendix A for the spectroscopic references.

can be found in appendix B.

3.2.2. Beam geometry

Figures 3.3 and 3.4 show the geometry of the optical setup around the trap. Doppler cooling light can be applied from three directions, termed "H1", "H2" and "V", to allow a three-dimensional characterization of ion motion, used, e.g. in the measurements of Ch. 6. The beams have elongated waists along the trap axis in order to cover all three segments and to illuminate extended crystals approximately homogeneously. Monitor photodiodes are present in all three beams to allow power stabilization using a common acousto-optic modulator (AOM), which is also used for pulse shaping during spectroscopy sequences. The cooling beam configuration can be set with the help of a mechanical shutter before each fiber. For spectroscopy, the H2 beam can be switched to circular polarization by means of a motorized quarter waveplate for optical pumping into the $m_j = -1/2$ substate of the ground state. A separate AOM is used to apply the optical pumping pulses independent of the Doppler cooling light.

For the use in spectroscopy sequences, each of the lasers at 411 nm, 639 nm and 1650 nm each can be switched with an AOM as well. The rf signals for all AOMs are controlled by

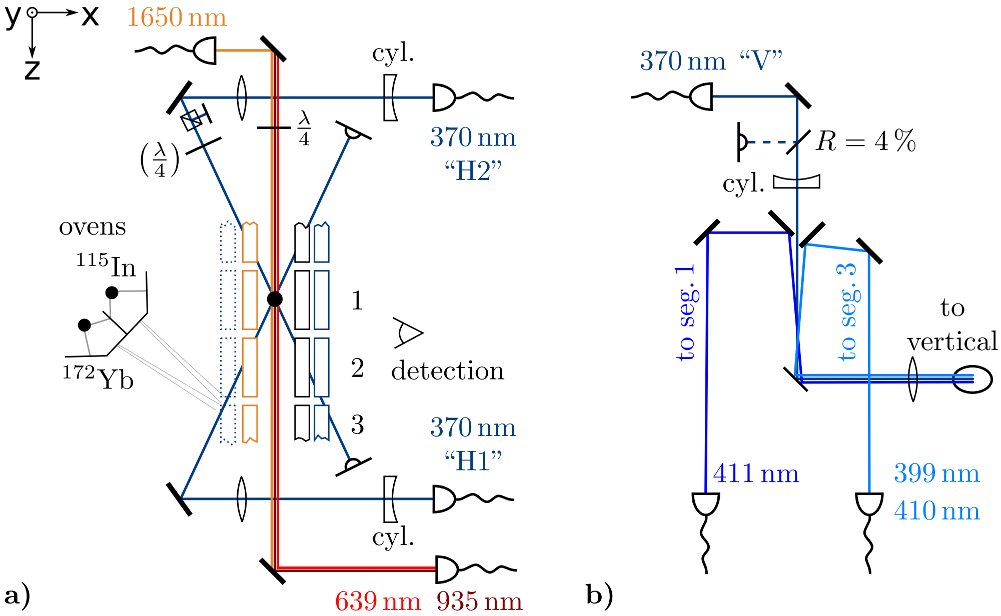
y
x
z
1650 nm
cyl.
$\frac{\lambda}{4}$
$(\frac{\lambda}{4})$
370 nm
"H2"
ovens
^{115}In
^{172}Yb
1
2
3
detection
370 nm
"H1"
cyl.
639 nm
935 nm
a)
b)
370 nm "V"
$R = 4\,\%$
cyl.
to seg. 1
to seg. 3
to
vertical
411 nm
399 nm
410 nm

Figure 3.3.: Simplified optical setup around the ion trap (not to scale). All 370 nm beams have elongated waists along the direction of the trap axis and cover all three trap segments (omitted for clarity). All fibers are polarization maintaining. **a)** top view of the trap showing the horizontal beam configuration and ovens. **b)** setup below the trap providing the vertical beams. Light at 410 nm is used for the photo-ionization of indium.

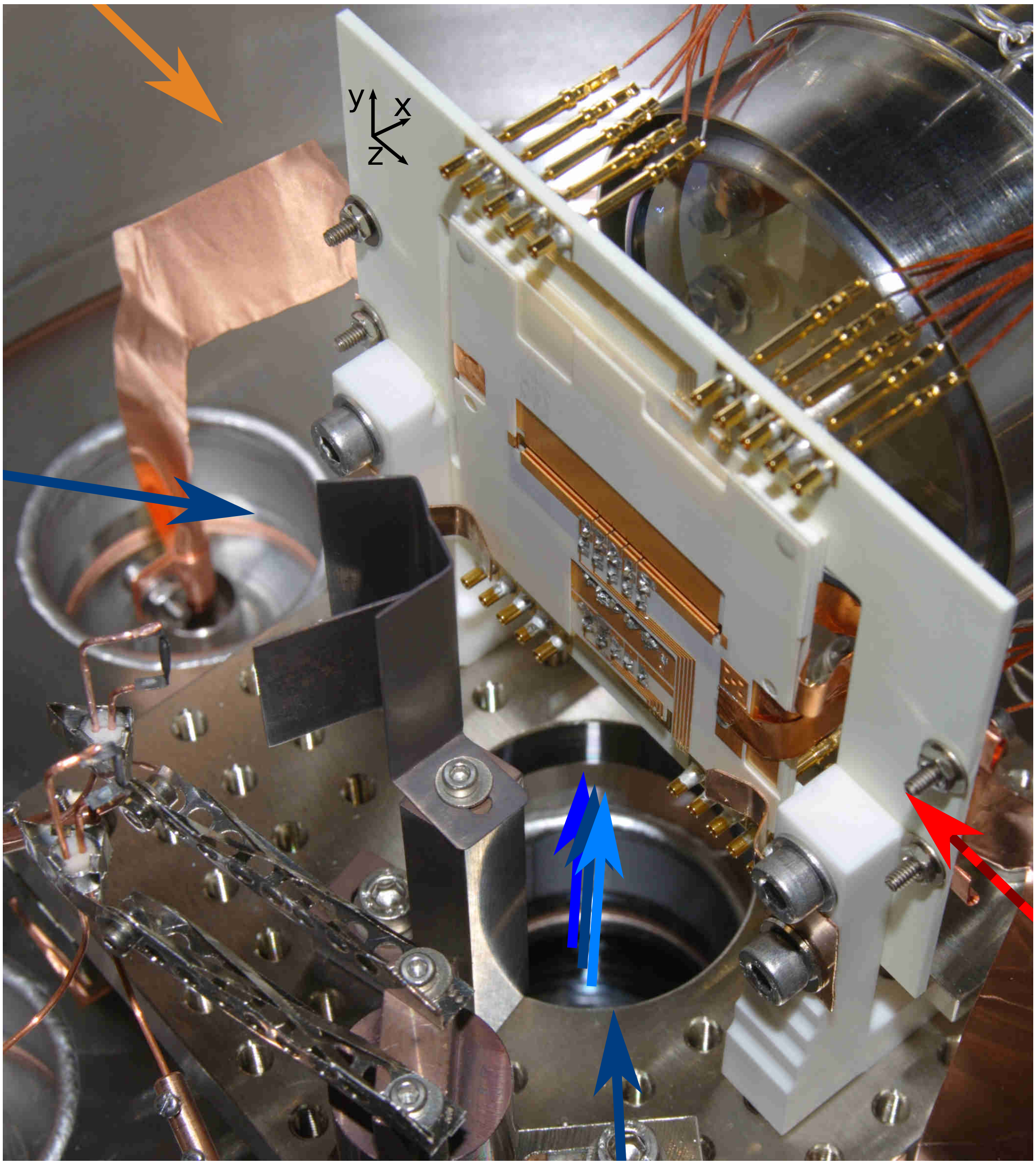

Figure 3.4.: Image of the prototype trap inside the vacuum chamber. The ovens are visible on the left; they consist of vertical tantalum tubes filled with Yb/In and are supported by the copper leads which also supply the currents. Atomic beams exit through a small hole facing right (not visible) and pass an aperture which protects the trap electrodes from contamination. Behind the trap carrier board, a re-entrant viewport with the imaging objective an be seen. The rf voltage is applied via the flat copper strip visible in the top left corner, some of the dc voltage connections can be seen at the top of the carrier board. Arrows indicate the directions of laser beams.

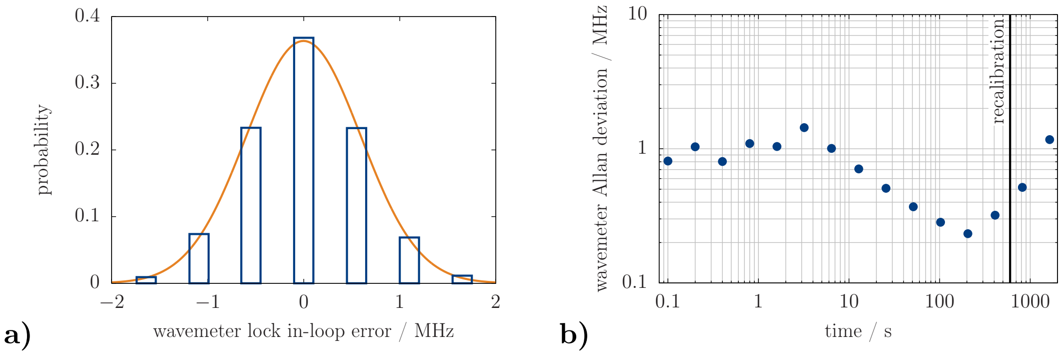

Figure 3.5.: Characterization of the wavemeter lock. **a)** histogram of the 739 nm laser in-loop error signal when locked to the wavemeter, recorded over a period of 680 s. The fit is a Gaussian distribution with $\sigma = 0.6$ MHz. **b)** Allan deviation of the wavemeter reading for the ultra-stable laser at 822 nm. To prevent the drift from exceeding 1 MHz, the wavemeter is re-calibrated every 600 s using this laser.

a field-programmable gate array (FPGA) which is programmed by the experiment control computer.

3.2.3. Wavemeter laser stabilization

The lasers at 798 nm, 739 nm, 935 nm, and 639 nm all address transitions with widths of several 10 MHz, either naturally or due to saturation broadening. Slow feedback to prevent frequency drifts is therefore sufficient for their stabilization. The reference is a wavemeter[1] with a mechanical fiber switch, which provides an update about every 100 ms for each channel. The experiment control computer implements a PI controller for each channel and steers the laser frequencies by adjusting the ECDL grating angles and laser diode currents at a fixed ratio. Figure 3.6a shows a histogram of the in-loop error values for the laser at 739 nm. According to the fit with a Gaussian distribution, the standard deviation of the mean frequency from the set value with respect to the wavemeter is 0.6 MHz.

As described in Ch. 4, the 822 nm fundamental light for spectroscopy on the 411 nm transition is referenced to an ultra-stable cavity with an absolute frequency drift below 0.1 Hz/s. This light is used as the reference for the wavemeter. Fig. 3.6b shows the Allan deviation of the wavemeter reading for this laser. After about 2000 s, the wavemeter drift would exceed its short-term instability of 1 MHz. This is prevented by re-calibrating to the 822 nm laser every 600 s.

---

[1] HighFinesse WS7

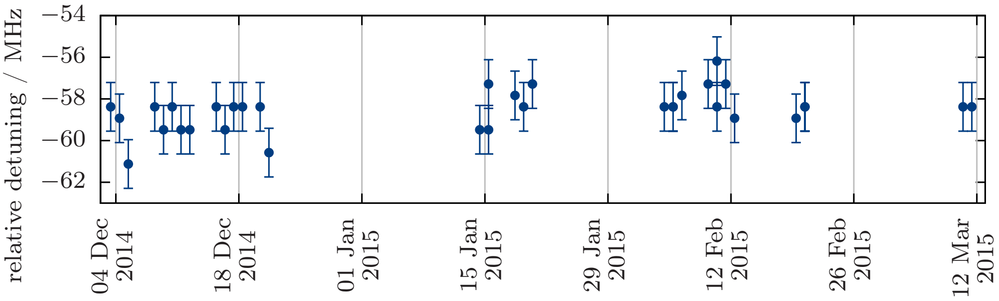

Figure 3.6.: Long-term wavemeter instability (with regular calibration at 822 nm), determined by the difference with respect to the literature value [82] of the reading at 739 nm when the frequency-doubled radiation is on resonance with the 370 nm cooling transition.

The long-term stability of the wavemeter with regular calibration shows in repeated scans of the atomic transitions. As an example, Fig. 3.6 shows the 739 nm laser wavemeter reading when its second harmonic is at resonance with the $^2S_{1/2} \leftrightarrow {}^2P_{1/2}$ transition, with respect to the literature value [82]. The resonance frequency is determined from photon-correlation measurements (see Ch. 6.3, Fig. 6.7). The overall mismatch of frequencies is well within the combined uncertainties of the wavemeter (150 MHz) and literature value of the transition ($1/2 \times 659$ MHz). Similar reproducibility is seen for the 798 nm laser, whereas the 639 nm laser reading at resonance differs by a few 10 MHz over the course of the day. This is probably caused by a higher differential temperature sensitivity of the reading with respect to 822 nm due to the higher frequency difference.

3.2.4. Spatially resolved state detection with an EMCCD camera

Both a photomultiplier tube (PMT) and an EMCCD camera[2] are available for detection. Light can be split equally between the devices or imaged entirely onto either by means of a slider containing a beamsplitter, a mirror and an open aperture. The fluorescence within 2 % of the solid angle is captured by a custom-made objective, which is described in more detail in Refs. [33, 34]. A narrowband optical filter at 370 nm is used to suppress straylight. At a magnification of 22, the camera has a spatial resolution of 0.72 μm per pixel and a total field of view of 370 μm. Computer-controlled actuators allow transverse and focal adjustment of the objective position in order to reproducibly switch between trap segments.

There are multiple reasons for performing state detection with a camera instead of a PMT. The most straightforward is that the camera can distinguish between excitations of different ions in a chain, which allows the evaluation to take different conditions into account, such as the laser intensity profile or a spatially inhomogeneous magnetic field. Moreover, with

---

[2] Andor iXon EM+ DU-897D-CS0-UVB

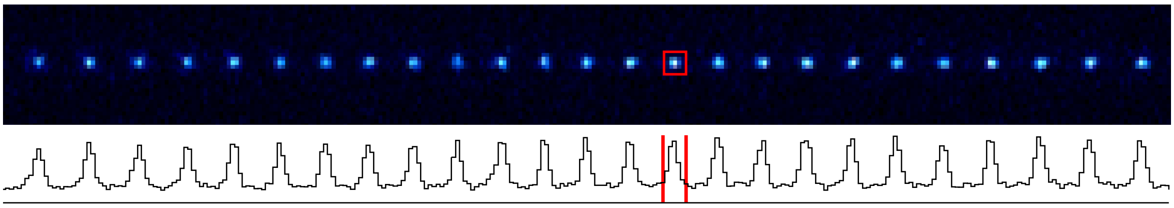

Figure 3.7.: False color EMCCD camera image showing part of a linear ion chain. A 5 × 5 pixel ROI, as used for state detection, is shown for one of the ions. The lower graph shows the column sums of the pixel values.

this detection system, shot noise affects each ion signal individually. This is important for the scalability of the clock readout, as the accumulated shot noise from an ensemble of ions would at some point exceed the signal of an individual ion and thereby prevent an exact determination of the excited fraction of ions. Another advantage of camera detection is the improved SNR: Since the detection beams are elongated along the trap axis to illuminate extended crystals, there is a higher level of straylight than obtainable when focusing onto a single ion. The spatial resolution of the camera allows a small region of interest (ROI) to be placed around each ion, which acts as a narrow aperture and thereby strongly suppresses this background. Figure 3.7 shows an image taken with this setup, including an ROI of 5×5 pixels, such as is used in the experiments.

Camera readout parameters and noise sources

The camera parameters for the experiments presented here have been optimized as a compromise between sequence duration and detection fidelity. The following section gives a brief overview of the camera parameters and the sources of noise in the readout process. A comprehensive analysis of these noise sources can be found in [83].

By cooling the detector chip to $-75\,^\circ\mathrm{C}$, the number of thermally excited electrons is suppressed to an order of 10^{-3}/s per pixel [83]. Electrons can however be excited by the (vertical) shifting of rows of pixels during readout. The number of these clock-induced charges (CIC) depends on the readout speed. Faster shifting is favorable, but the speed is limited by an increasing probability to lose image electrons in the process. The fastest shift speed without losing image information is $0.5\,\mu$s per row, at which clocking noise of $1.4 \times 10^{-3}\,\mathrm{e}^-$ per pixel and image has been observed using images with a closed camera shutter. Pixels within a row are then shifted horizontally at a rate of 5 MHz for readout. Using these settings, an image can be recorded every 1.5 ms (including exposure).

The major advantage of an EMCCD is the direct amplification of image electrons, which

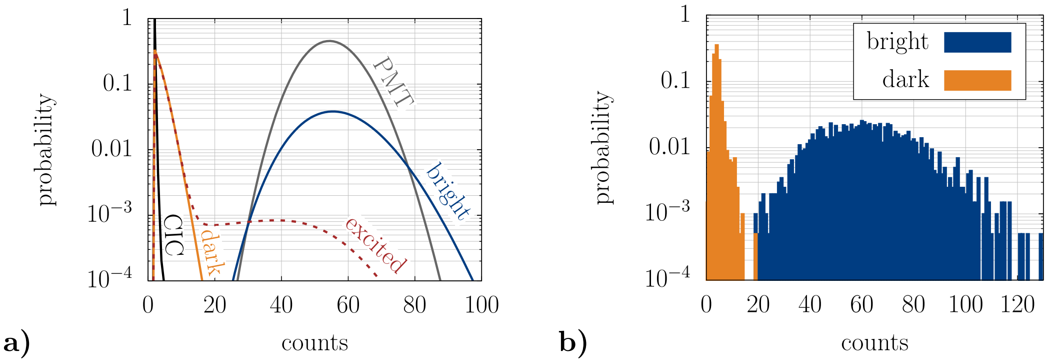

Figure 3.8.: a) calculated distributions for the EMCCD signals of a single ion. Experimental values are used for CIC and the straylight and fluorescence count rates. The graphs labeled "bright" and "dark" correspond to an ion in the ground and excited state during the entire exposure, respectively; the dashed line labeled "excited" takes into account the fraction of ions decaying back to the ground state during the 1.5 ms exposure. A Poisson distribution for the bright count rate, as would be obtained with a PMT of the same quantum efficiency, is shown for comparison. **b)** measured distributions. Note that the bright distribution is slightly broader than the model predicts because the fluorescence is distributed among 25 pixels, which are individually amplified. On-chip binning can improve this at the cost of a reduced spatial resolution.

makes noise from the subsequent A/D conversion negligible. The EM amplifier consists of a series of "gain pixels", in which secondary electrons are produced by impact ionization. An amplification of up to 1000 is achieved by cascading several hundred amplification stages, each with a gain slightly above 1. Since the stochastic nature of this process leads to fluctuations in the overall gain, it is an additional source of noise. Different models have been used to describe this process, with similar results [83, 84]. In the limit of high gain and with a normal distribution of the input electron number, the description can be simplified to an increase of the variance by a factor of 2.

Finally, the output distribution of counts also depends on the noise of the light impinging on the sensor. Both straylight and fluorescence photons are detected with a limited quantum efficiency of 0.35 and follow Poisson distributions. Additional errors can occur when the ion decays back to the ground state during the detection period, as has been derived in [73, App. 2.2] for the $^2S_{1/2} \leftrightarrow {}^2D_{5/2}$ transition in Ca^+. The $^2D_{5/2}$ state in Yb^+ only has a lifetime of 7 ms, but 83 % of its population decays to the $^2F_{7/2}$ state and therefore stays dark during the detection.

Figure 3.8a shows the count distributions according to the model derived in [83] for experimentally determined parameters and an exposure time of 1.5 ms. The intensity and detuning of the laser at 370 nm are $I \approx 0.3 \times I_{\mathrm{sat}}$ and $\Delta = -\Gamma/2$ and all of the collected fluorescence is imaged onto the camera. To illustrate the broadening due to the amplification process, the bright (Poisson) distribution of a PMT is shown for comparison, assuming an equal quantum efficiency. Normalized histograms of 2000 measurements each are shown in Fig. 3.8b for a fluorescing ion and the straylight background. The 25 pixels of the ROI are amplified individually, leading to a broader distribution as predicted by the model. At the cost of a reduced spatial resolution, it could be narrowed by binning the collected charges during the readout, before they enter the gain register.

With these settings, the camera allows state discrimination with a simple threshold condition for the number of counts.

4. Stable lasers for motional and clock spectroscopy

Two transitions in the mixed $^{115}\mathrm{In}^+$ / $^{172}\mathrm{Yb}^+$ system require highly stable lasers. The most demanding is the local oscillator for clock spectroscopy on the $^1\mathrm{S}_0 \leftrightarrow {}^3\mathrm{P}_0$ transition in $^{115}\mathrm{In}^+$ ($\Gamma = 2\pi \times 0.8\,\mathrm{Hz}$). As detailed in Ch. 2, its fractional frequency instability should be on the order of 1×10^{-16} for averaging times of $200\,\mathrm{ms} < \tau < 400\,\mathrm{ms}$ in order not to limit the instability of a clock based on 100 indium ions. The second stable laser is used to address the $^2\mathrm{S}_{1/2} \leftrightarrow {}^2\mathrm{D}_{5/2}$ transition ($\Gamma = 2\pi \times 23\,\mathrm{Hz}$) in $^{172}\mathrm{Yb}^+$. This transition allows the resolution of motional sidebands in the trap for the study and control of the Coulomb crystal dynamics. Since the requirements for the ytterbium spectroscopy laser are less strict, it was built up first and used to assess which contributions to frequency instability need to be further suppressed in the $^{115}\mathrm{In}^+$ clock laser. The laser reaches a fractional frequency instability below $\sigma_y = 5 \times 10^{-16}$ in 4 s with a comparatively simple setup, without vibration-insensitive cavity mounting, under typical laboratory conditions. The individual instability contributions are described in detail in section 4.2. For the $^{115}\mathrm{In}^+$ clock laser, a simple vibration-insensitive cavity design for achieving $\sigma_y = 1 \times 10^{-16}$ with a room temperature setup is implemented. Finite-element method (FEM) calculations of the vibration sensitivity and their experimental confirmation are presented in section 4.3. The main results in this chapter have been published in Applied Physics B [85].

4.1. Laser stabilization to optical cavities

Optical cavities made from ultra-low thermal expansion glass[1] are used for the stabilization of both lasers, as they have proven to be highly stable frequency references at the required timescales [12]. Stabilizing a laser to a cavity means transferring fractional length stability into fractional frequency stability: $\Delta\nu/\nu = -\Delta l/l$. The technical challenge is therefore to suppress all external influences on the cavity length. A fundamental limit for these length fluctuations is thermal noise, i.e. the Brownian motion in the constituents of the cavity. The choice of materials and geometry is therefore in part dictated by the need to minimize the impact of such thermal motion.

---

[1] Corning Inc. ULE®

4.1.1. Thermal noise

The basis for calculating the degree of length fluctuations due to thermal noise is the fluctuation-dissipation theorem [86], which states that thermal fluctuations are caused by the same microscopic processes responsible for the dissipation of the energy from a small periodic external force. The displacement power spectral density (PSD) due to thermal fluctuations as probed by the light field inside the cavity can therefore be derived from the dissipation of power due to a periodic force at the mirror surface with the same spatial distribution as the mode profile [87]. The most important material property in this context is the mechanical quality factor (Q). Since the cavities consist of rigid materials, the mechanical resonances are far above the relevant frequency range, and a frequency-independent loss factor $\phi = 1/Q$ can be assumed. The displacement noise then has a PSD of $G(f) \propto 1/f$ (flicker frequency noise). The resulting fractional frequency Allan deviation [88] for a cavity of length l_spacer,

$$\sigma_y = \frac{\sigma_\nu}{\nu} = \frac{\sigma_l}{l_\text{spacer}} = \sqrt{2\ln(2)}\frac{\sqrt{G(1\,\text{Hz})}}{l_\text{spacer}} , \tag{4.1}$$

is independent of the averaging time [89].

The effect of thermal noise can be reduced by using materials with higher quality factors. While ULE is chosen as the spacer material for its low coefficient of thermal expansion (CTE), fused silica (FS) can be used for the mirror substrates [90, 91] in order to reduce their contribution by about a factor of 20. Even further reduction has been achieved with a spacer and mirror substrates made from silicon [92], both due to its higher Q factor and the fact that the cavity can be operated at cryogenic temperatures, where the CTE of silicon has two zero crossings. Another approach is to increase the spot size on the mirror surfaces in order to average fluctuations over a larger area [93–95]. A straightforward solution is to increase the spacer length [95–98], which reduces the relative influence of the mirror contributions by $1/l_\text{spacer}$, and the spacer contribution by $1/\sqrt{l_\text{spacer}}$.

Numata et al. [99] have derived analytic expressions to estimate the thermal noise contributions of the cavity spacer, mirror substrates and mirror coatings. Table 4.1 lists those contributions for the two ULE cavities with FS mirrors described in this chapter. Since then, Kessler et al. [100] have shown that the spacer contribution is underestimated by this approach, mainly due to additional deformations close to the spacer-mirror interfaces. For the cavities discussed here however, these corrections are negligible, since the mirror contributions are an order of magnitude above those from the spacer.

Table 4.1 shows that the mirror coatings are the most problematic constituent in terms of thermal noise. Tantalum pentoxide (Ta_2O_5) layers, as used in dielectric high-reflectivity coatings, are known to be problematic due to their low Q [101]. Various approaches have been investigated to reduce this contribution, including thermal noise optimized layer thicknesses

	^{172}**Yb**$^+$ **cavity**	^{115}**In**$^+$ **cavity**
spacer length	12 cm	30 cm
TEM$_{00}$ spot sizes	293 μm, 313 μm	371 μm, 446 μm
$G_{\mathrm{spacer}}(1\,\mathrm{Hz})$	$9 \times 10^{-36}\,\mathrm{m^2/Hz}$	$3 \times 10^{-35}\,\mathrm{m^2/Hz}$
$G_{\mathrm{substrates}}(1\,\mathrm{Hz})$	$1 \times 10^{-34}\,\mathrm{m^2/Hz}$	$1 \times 10^{-34}\,\mathrm{m^2/Hz}$
$G_{\mathrm{coatings}}(1\,\mathrm{Hz})$	$7 \times 10^{-34}\,\mathrm{m^2/Hz}$	$5 \times 10^{-34}\,\mathrm{m^2/Hz}$
σ_y (thermal noise floor)	2.9×10^{-16}	9.4×10^{-17}

Table 4.1.: Contributions to thermal noise from the spacers, mirror substrates and coatings for the cavities described in this chapter, estimated according to Numata et al. [99].

to reduce the amount of Ta$_2$O$_5$ [102], different coating materials [103, 104], and diffractive structures to replace the coating altogether [105].

4.2. Spectroscopy laser for ^{172}Yb$^+$

The ^{172}Yb$^+$ spectroscopy laser system consists of an ECDL operating at 822 nm, which is amplified and frequency doubled to address the $^2\mathrm{S}_{1/2} \leftrightarrow {}^2\mathrm{D}_{5/2}$ transition at 411 nm. It is stabilized to a cavity which consists of a cylindrical spacer with a length of 12 cm and a diameter of 6 cm. This section presents the experimental setup and discusses the individual frequency instability contributions, which are summarized in Fig. 4.1.

4.2.1. Environmental vibrations

The spacer design is not optimized for vibration insensitivity; the support consists of four viton rings approximately at the longitudinal Airy points of the spacer, as shown in Figs. 4.2a,b and 4.3. An estimate taking only deformation due to the Poisson effect into account (assuming a density of $2.2 \times 10^3\,\mathrm{kg/m^3}$, Young's modulus of 6.8×10^{10} Pa, and Poisson ratio of 0.17 [106]) results in a sensitivity of the frequency to vertical accelerations of $2.8 \times 10^{-10}\,/(\mathrm{ms^{-2}})$. Since the mounting is symmetric in the other dimensions, lower values are expected for the sensitivities to horizontal vibrations. The vibration sensitivities have been determined experimentally by monitoring the frequency of the laser stabilized to the cavity while subjecting the setup to controlled mechanical oscillations. The observed values are $3.5(2) \times 10^{-10}\,/(\mathrm{ms^{-2}})$ (vertical accelerations) and below $10^{-10}\,/(\mathrm{ms^{-2}})$ (horizontal). To reduce the influence of vibrations on the frequency stability, the cavity is set up on a passive vibration isolation

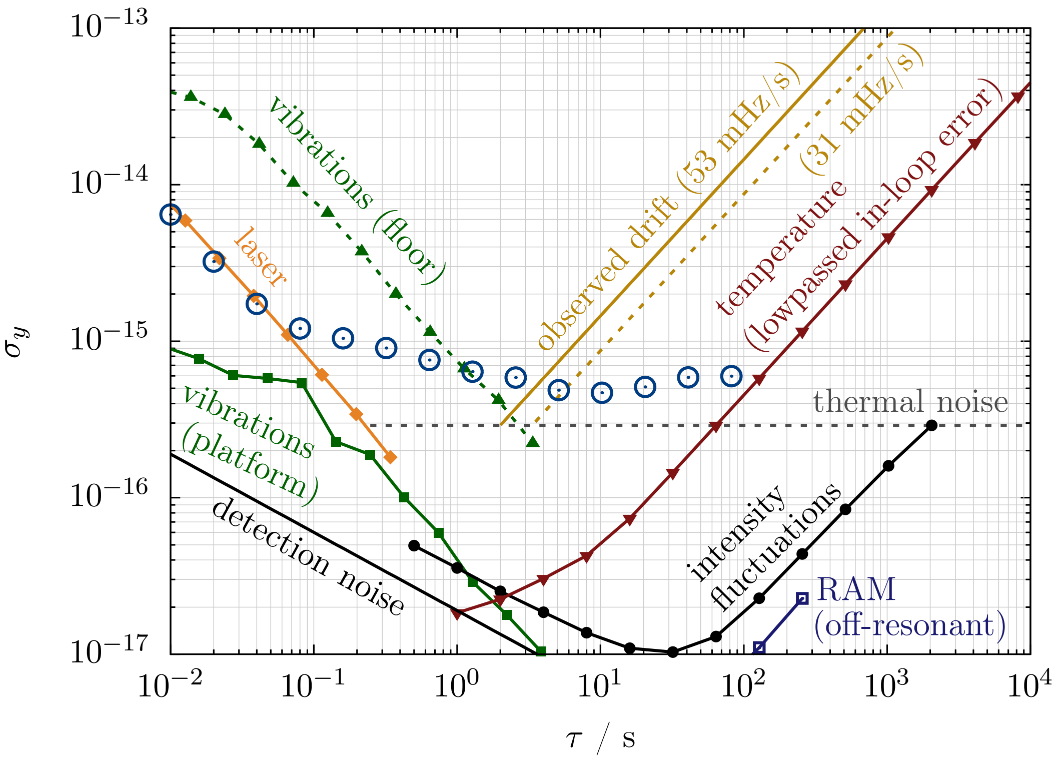

Figure 4.1.: Summary of instability contributions of an ECDL stabilized to a 12 cm long ULE cavity. Instabilities are given as fractional frequency Allan deviations [88]. The blue open circles show the resulting instability of the laser (after removing the linear drift) determined in a three-cornered-hat measurement with two other stable lasers.

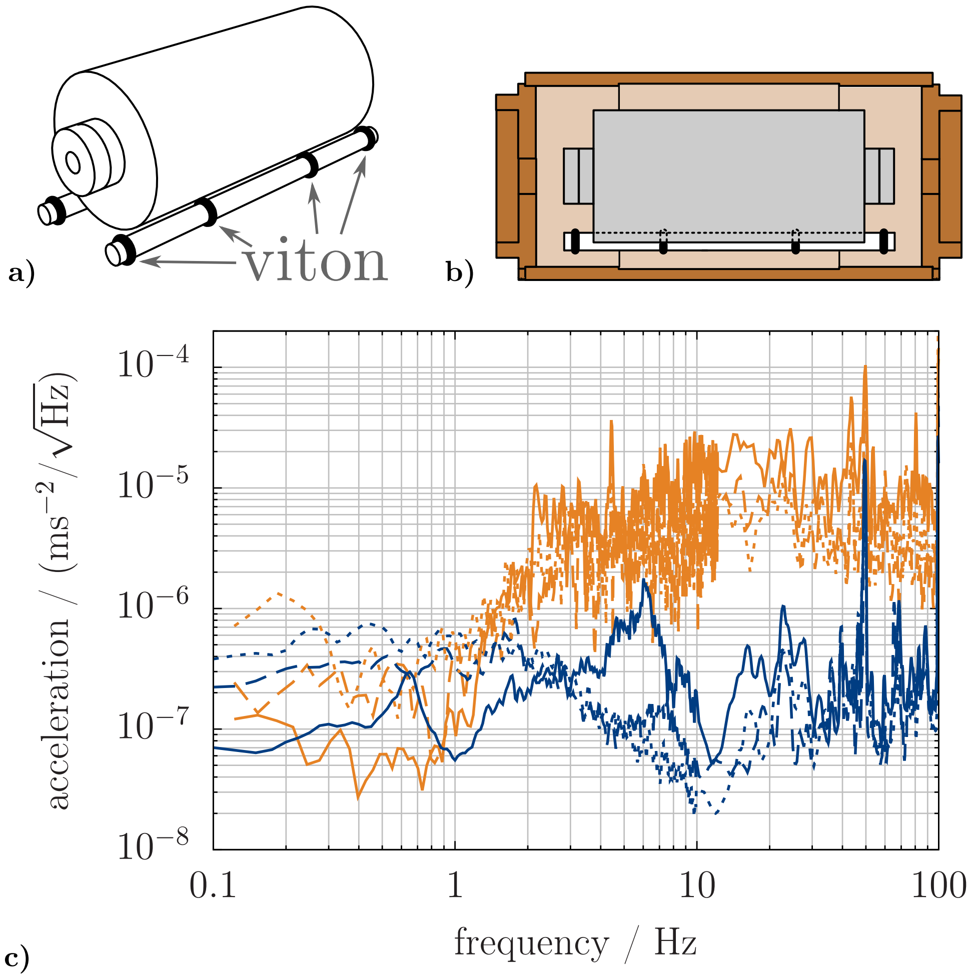

Figure 4.2.: Cavity mount and environmental vibrations. **a)** the spacer is supported by four viton rings held in place by fused silica rods. **b)** these rods rest on four additional viton rings inside a cylindrical copper heat shield with varying inner diameter. Their transverse distance is fixed by an aluminium clamp (not depicted). **c)** acceleration spectra due to environmental vibrations. The orange curves were recorded on the floor of the laboratory; blue curves show the suppressed vibrations on the passive isolation platform supporting the cavity. The solid lines correspond to the vertical, dashed and dotted lines to the horizontal directions. The peak at 50 Hz is due to electronic noise.

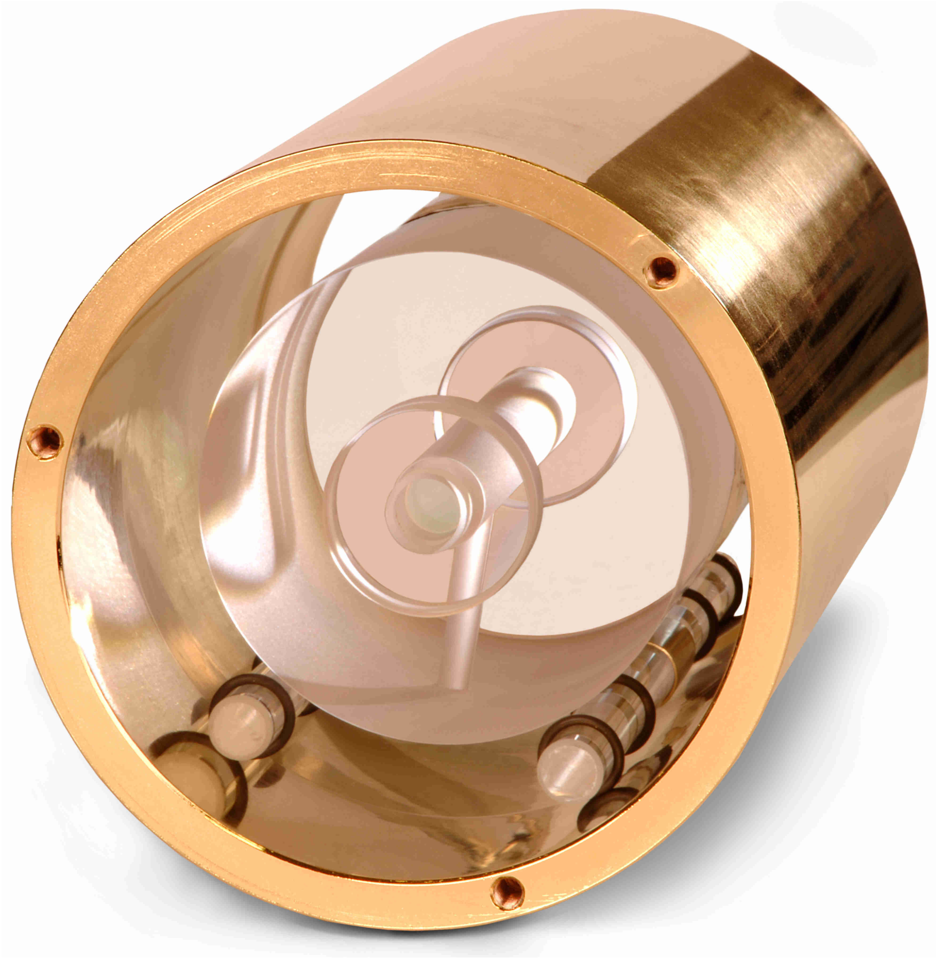

Figure 4.3.: Photo of the 12 cm cavity and its mount within the copper heat shield.

Figure 4.4.: Frequency response to a temperature step (24.56 °C to 24.99 °C) measured using a frequency comb referenced to a hydrogen maser. The dots show the experimental data after subtracting the previously observed linear drift; the solid line is a fourth-order low-pass function fitted to the data. The time constants are $\tau_1 = \tau_2 = 1.8\,\mathrm{h}$ (active stabilization), $\tau_3 = 1.9\,\mathrm{h}$ (copper ↔ cavity), and $\tau_3 = 44.4\,\mathrm{h}$ (vacuum chamber ↔ copper). The inset schematically shows the heat shield configuration.

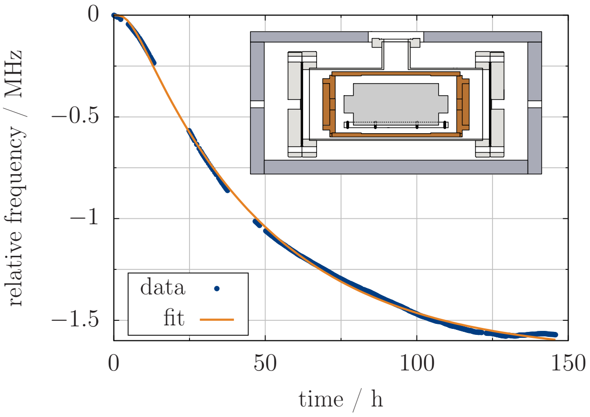

platform[2]. Additional acoustic isolation is achieved by encasing the whole setup in a wooden box lined with sound absorbing polyurethane mats[3]. Figure 4.2c shows the acceleration spectra measured on the laboratory floor as well as the suppressed accelerations on the platform. The contribution to frequency instability is obtained by multiplying these with the respective sensitivities; the corresponding Allan deviations are shown in Fig. 4.1 as green squares (triangles) for the case with (without) the passive vibration isolation. While this is more than sufficient for the purpose of this laser, it would be above the maximum acceptable instability of the clock laser.

4.2.2. Thermal expansion and aging

The spacer material is expected to have a zero-crossing of its CTE around 20 °C. However, the CTE mismatch between ULE and FS induces stress at the spacer-mirror interface, which leads to a temperature-dependent bulging of the mirrors. This effect, which would reduce the zero crossing temperature of the combined effective CTE to between −10 °C and 0 °C, is expected to be suppressed by about a factor of 7 by ULE rings (6 mm thickness, outer/inner diameter of 25.4 mm and 8 mm) optically contacted to the back of the mirrors [107]. This allows the use of a simple temperature stabilization based on resistive heating that keeps the setup slightly above room temperature, at about 25 °C, which is still reasonably close to the zero-crossing. The expected temperature sensitivity of $1.7 \times 10^{-9}\,\mathrm{K}^{-2}$ around the zero-crossing [106] requires temperature fluctuations to be on the order of 10 nK on the relevant timescales. As shown schematically in the inset of Fig. 4.4, two heat shields are used in order to achieve this. To avoid convective heat transfer (and fluctuations of the refractive index), the cavity is inside a vacuum of $10^{-6}\,\mathrm{Pa}$. Within the vacuum chamber, temperature fluctuations are passively dampened by a copper cylinder with polished surfaces that are gold coated to prevent a decrease in reflectivity due to oxidation. To decouple the cavity mount from the thermal expansion of the copper, the supporting viton rings are held in place by two fused silica rods which are in turn resting on additional viton rings, as shown in Figs. 4.2a,b and 4.3. The vacuum chamber is placed inside an aluminium enclosure, which is where the active temperature stabilization is applied. A layer of polystyrene and the acoustic isolation box provide additional decoupling from fluctuations of the room temperature.

---

[2] Minus-K Technology 150BM-1

[3] BaryCell 1440

To estimate the temperature filtering effect of the copper shield, the radiative heat transfer at each stage is modeled as a 1st-order lowpass. Assuming a small deviation from thermal equilibrium at temperature T and equal surface area A, the time constant can be estimated as

$$\tau = \frac{\varepsilon_1 + \varepsilon_2 - \varepsilon_1 \varepsilon_2}{4\sigma \varepsilon_1 \varepsilon_2 A T^3} C \,, \tag{4.2}$$

where ε_i denote the emissivities of the two surfaces, C is the heat capacity of the inner object and σ the Stefan-Boltzmann constant. This model predicts a time constant of 1.5 to 3 days for the temperature of the copper heat shield and another 19 h to 46 h before fluctuations reach the cavity. The main uncertainty is due to the unknown emissivities. With an estimated time constant of more than 10 days, heat conduction through the mount is negligible.

For an experimental characterization of the temperature instability, the effect of a temperature step on the resonance frequency is observed by monitoring the beat note of the laser with a frequency comb referenced to a hydrogen maser. Figure 4.4 shows the response after subtracting the linear drift. A fourth-order low-pass function is fitted to the data, with two of the time constants fixed at 1.8 h, as determined from the error signal of the temperature PI controller. The additional time constants are 44.4(5) h and 1.93(1) h. Using the 1st-order lowpass model, the long time constant can be attributed to the heat transfer between the vacuum chamber ($\varepsilon_{\mathrm{steel}} = 0.3$) and the gold-coated copper cylinder ($\varepsilon_{\mathrm{Cu1}} = 0.05$). The second time constant corresponds to heat transfer between the copper cylinder and the cavity if emissivities of $\varepsilon_{\mathrm{Cu2}} = 0.5$ and $\varepsilon_{\mathrm{ULE}} = 0.8$ are assumed. The order of magnitude difference between the two values for the copper cylinder could be due to the dullness of the indented section in the inner surface due to imperfections in the electroplating process.

The temperature sensitivity of the frequency is seen to be $-1.02(5) \times 10^{-8}\,\mathrm{K}^{-1}$, which corresponds to a zero crossing of the composite cavity effective CTE at 19(1) °C. According to [107], this implies that the CTE of the spacer material vanishes at about 22 °C.

The effect of temperature fluctuations on the achievable instability can be estimated using the error signal of the temperature controller, which has an instability of 2 mK in 1 s. After applying the heat shield lowpass functions, the curve shown in Fig. 4.1 (red triangles) is obtained. As it is derived from an in-loop signal, this just serves as a lower bound. It corresponds to a linear drift of $2\,\mathrm{mHz/s}$, which is negligible compared to the expected effect due to

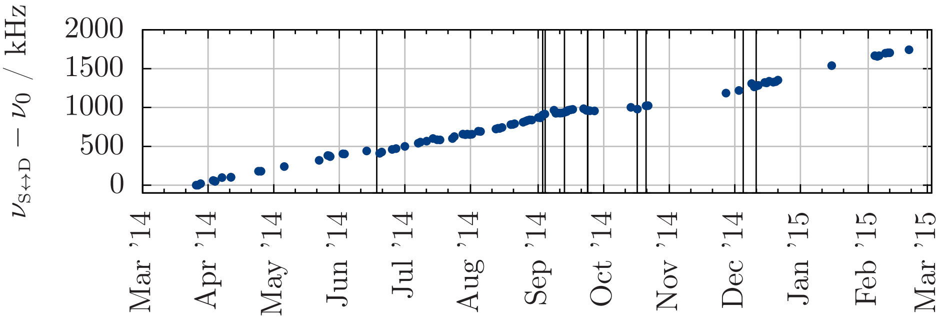

Figure 4.5.: Long-term behavior of the resonance frequency as determined by the relative shift of the frequency-doubled radiation with respect to the atomic resonance. A linear fit results in a 31 mHz/s drift of the cavity resonance. Vertical lines mark adjustments of the magnetic field compensation at the ion position, which affects these measurements via the Zeeman shift.

aging of the spacer material [108]. After about two years in vacuum, experimentally observed frequency variations with respect to a hydrogen maser within a period of 4×10^4 s reveal a linear drift of 53 mHz/s and a sinusoidal variation with an amplitude of 132 Hz and a period of ≈ 1 d. Higher order frequency fluctuations contribute less than 8×10^{-15} in 8000 s. Figure 4.5 shows the change in the frequency shift with respect to the atomic resonance, starting about one year after the previous determination. The linear drift seen in these measurements is about 31 mHz/s.

4.2.3. Power sensitivity

Due to the high finesse of about 2.8×10^5, fluctuations of the input power are strongly amplified within the cavity, resulting in temperature changes of the mirror coatings and substrates that shift the resonance frequency. The sensitivity to this effect is $2 \times 10^{-13}\,\mathrm{W}^{-1}$ (intracavity power), as determined by observing the change in frequency when a step of $\pm 5\,\mu$W is applied to the input power. The response is shown in Fig. 4.6. A fit indicates that two processes with time constants of 0.3 s and 5 s, observed for both increasing and decreasing power, contribute by an equal amount to this shift. Keeping this contribution below the thermal noise limit at an input power of $25\,\mu$W and a coupling efficiency of 0.35 requires a relative intensity instability on the order of 10^{-4}, which is realized by an active stabilization using an AOM. The error signal uses the transmitted power to prevent fluctuating non-resonant stray light from affecting the stabilization. The contribution to the frequency instability, derived from an out-of-loop measurement of the power instability, is shown in Fig. 4.1 as filled black circles.

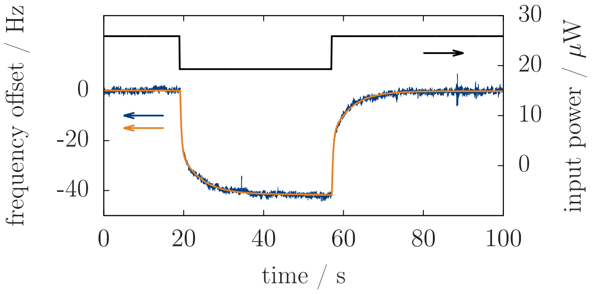

Figure 4.6.: Response of the cavity resonance frequency to a step in the input intensity. The fit reveals a sensitivity of $2 \times 10^{-13}\,\mathrm{W}^{-1}$ (intracavity power) and time constants of 0.3 s and 5 s, independent of the step direction.

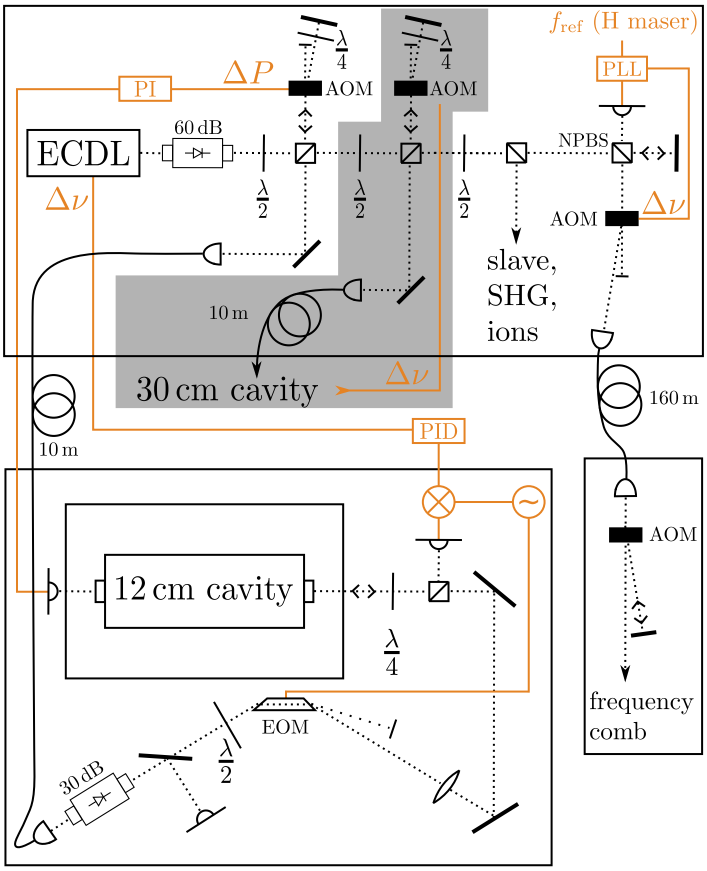
f_{ref} (H maser)
PLL
PI
ΔP
$\frac{\lambda}{4}$
AOM
$\frac{\lambda}{4}$
AOM
ECDL
60 dB
$\frac{\lambda}{2}$
$\frac{\lambda}{2}$
$\frac{\lambda}{2}$
NPBS
$\Delta\nu$
AOM
$\Delta\nu$
slave,
SHG,
ions
10 m
30 cm cavity
$\Delta\nu$
160 m
10 m
PID
AOM
12 cm cavity
$\frac{\lambda}{4}$
EOM
$\frac{\lambda}{2}$
30 dB
frequency
comb

Figure 4.7.: Simplified diagram of the optical setup. All fibers are polarization maintaining; beam splitter cubes are polarizing unless labeled otherwise. The shaded area indicates the temporary addition used for the measurements described in section 4.3.

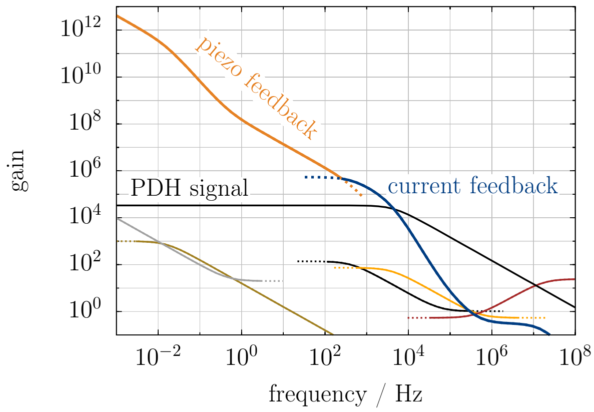

Figure 4.8.: Amplitude section of the feedback Bode diagram. The black line marked "PDH signal" represents the optical part of the setup, including the lowpass characteristic of the cavity and the ratio between voltages applied to the modulation input of the laser and the error signal. Unmarked lines in the lower part of the graph correspond to individual contributions from an integrator, three lowpasses and a differentiator. All components are connected in series.

4.2.4. Laser system and measured instability

The simplified schematic diagram of the complete laser system is shown in Fig. 4.7. A grating stabilized 822 nm diode laser in Littrow configuration is locked to the cavity by applying feedback to the piezo actuator that adjusts the grating, and to the injection current using a transistor in parallel to the laser diode. The error signal is generated using the Pound-Drever-Hall (PDH) method [109]. Figure 4.8 shows the frequency dependence of the feedback gain. Disturbances at frequencies below 0.5 kHz are corrected with the piezo, whereas noise between 0.5 kHz and 410 kHz is suppressed via the current. Much higher feedback bandwidths have been achieved with diode lasers [110], but the current modulation of this diode is limited by a resonance at about 1.2 MHz. The frequency noise PSD of the free running diode laser is shown in Fig. 4.9a, along with the expected suppression due to the gain characteristic of the feedback. The detection noise floor, determined from the PSD of the in-loop error signal, is shown as a solid black line. The corresponding Allan deviations, shown in Fig. 4.9b, reveal that white frequency noise at frequencies beyond the feedback bandwidth, likely Schawlow-Townes noise [111], is the limiting instability contribution for averaging times below 0.1 s. Experimentally, the instability at a given time $\tau < 0.1$ s is observed to scale with the inverse square root of the feedback bandwidth. It can be seen from Fig. 4.9b that this is expected: the bandwidth determines the time at which the slope of the Allan deviation changes from $\propto \tau^{-1/2}$ (white frequency noise) to $\propto \tau^{-1}$.

For generating the PDH error signal, sidebands at 32 MHz are introduced by phase modulation in an electro-optic modulator (EOM) with a Brewster cut crystal. This geometry spatially separates any residual power in the (non-modulated) ordinary beam from the extraordinary beam and prevents multiple reflections inside the crystal from overlapping, thus reducing residual amplitude modulation (RAM). The RAM component present when the light is off resonance contributes less than $\sigma_y = 10^{-17}$ for times between 0.5 s and 100 s (open blue squares in Fig. 4.1). On resonance, an additional component due to parasitic etalons

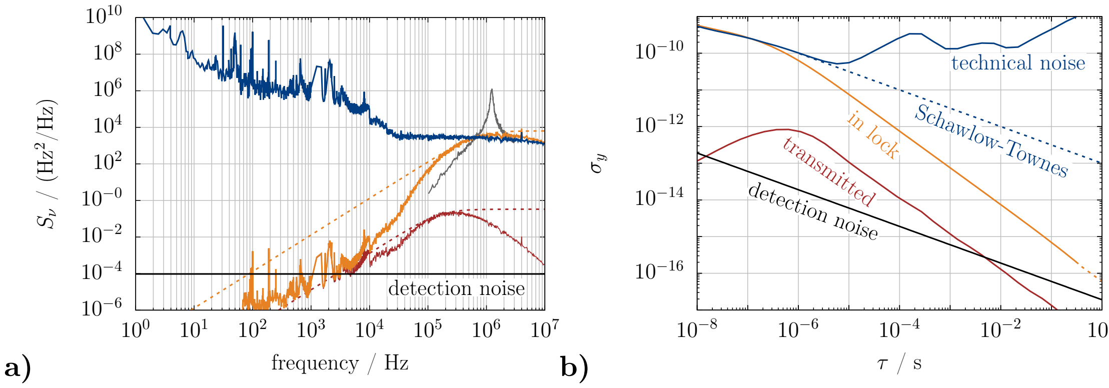

Figure 4.9.: a) frequency noise power spectral density of the free running laser (blue) and adjusted for the expected suppression by the feedback (orange) and in the light transmitted through the cavity (red, discussed in section 4.2.5). A resonance in the current modulation at about 1.2 MHz limits the bandwidth, as shown by the grey trace. The dashed lines show the power law estimates used in section 4.2.5. **b)** Allan deviations corresponding to the spectra in **a**.

coupled to the cavity ("line pulling") could appear that cannot be measured separately.

To characterize the system, the light is transferred to a hydrogen-maser-referenced frequency comb using a 160 m fiber with active phase noise cancellation [112]. The frequency instability is determined in a three-cornered-hat measurement [113] using transfer beat notes [114] with two other stable lasers: a fiber laser at 1543 nm stabilized to a cryogenic silicon cavity [92] and a diode laser at 698 nm stabilized to a ULE cavity. Subtracting the linear drift, a minimum fractional frequency Allan deviation of 4.7×10^{-16} is reached for an averaging time of 10 s as shown in Fig. 4.1 (open blue circles). For averaging times between 0.1 s and 1 s, there is a discrepancy between the expected contributions and the measured instability. The modified Allan deviation [115], shown in Fig. 4.10, averages out the high-frequency contributions more quickly and thereby identifies a peak around $\tau = 0.2$ s. Further tests have shown that it is caused by vibrations transmitted through the power supply cable of the temperature stabilization circuit, which was not present during the acceleration measurements shown in Fig. 4.2c. With the cable temporarily removed, the laser achieves an instability of $\sigma_y = 3.7 \times 10^{-16}$ in 4 s. While this is not an issue for the Yb$^+$ laser system, the cables for the clock laser system have to be chosen more carefully. Cables as soft as RG-58 (or Lemo type 106330 for supplying high voltages) have proven not to be a limitation at this level.

For spectroscopy on the ^{172}Yb$^+$ ^{2}S$_{1/2} \leftrightarrow {}^2D_{5/2}$ transition, the light is frequency doubled using a periodically poled potassium titanyl phosphate (PPKTP) crystal [116]. The SHG input power of 65 mW is produced by an injection-locked ("slave") laser diode.

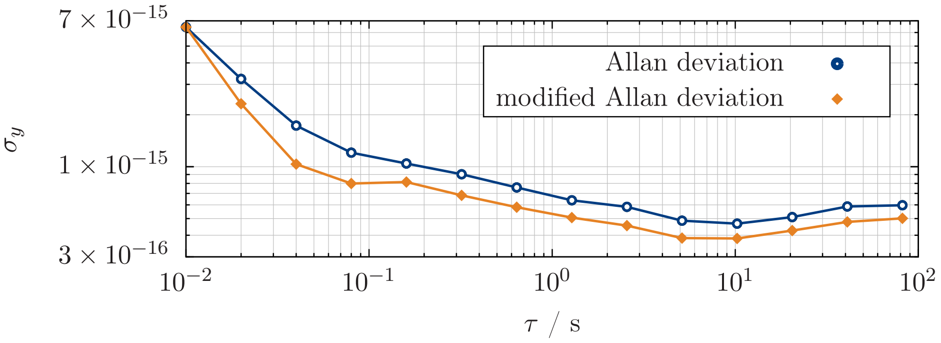

Figure 4.10.: The modified Allan deviation reveals the peak at 0.2 s due to vibrations transmitted by a cable.

4.2.5. Suitability for spectroscopy

The frequency instability of this laser system is suppressed to the level of the cavity length instability for times $\tau \geq 200\,\text{ms}$. Section 4.3 is concerned with lowering the cavity contributions to the level of 1×10^{-16} for the clock laser. Since clock interrogation averages the laser frequency over a pulse duration of several 100 ms, high frequency noise would not degrade the outcome. The ^{172}Yb^{+} spectroscopy laser, however, is meant to investigate the dynamics of Coulomb crystals, which occur on timescales on the order of a period of secular motion ($\approx 10\,\mu$s). If weak sidebands are to be probed in the vicinity of much stronger transitions, off-resonant excitation due to laser phase noise at high Fourier frequencies ($> 10\,\text{kHz}$) must be avoided. Its influence is best understood from the power distribution in the carrier frequency domain, which is estimated in the following.

If amplitude noise is negligible and the phase noise PSD does not diverge for $f \to 0$, it can be used to calculate the carrier domain spectrum of the laser under the assumption that the noise process is ergodic [117]. For Fourier frequencies above 100 Hz, the phase noise PSD of the locked laser can be conservatively estimated by a 1st-order lowpass

$$S_\Phi(f) = \frac{S_\nu(f)}{f^2} \leq \frac{K}{1 + (f/f_0)^2}\,, \tag{4.3}$$

as shown in Fig. 4.9a (dashed orange line), for which the carrier domain spectrum is described by the analytic expression [118]

$$\begin{aligned} S_E(\nu) &= \frac{\delta(\Delta)}{f_0} + K\ \mathrm{Re}\left[\frac{{}_2F_2(1, 1 - i\Delta; 2, 2 - i\Delta; \sigma_\Phi^2)}{1 - i\Delta}\right] \\ \text{with} \quad \Delta &= \frac{\nu - \nu_0}{f_0} \quad \text{and} \quad \sigma_\Phi^2 = \pi K f_0\,. \end{aligned} \tag{4.4}$$

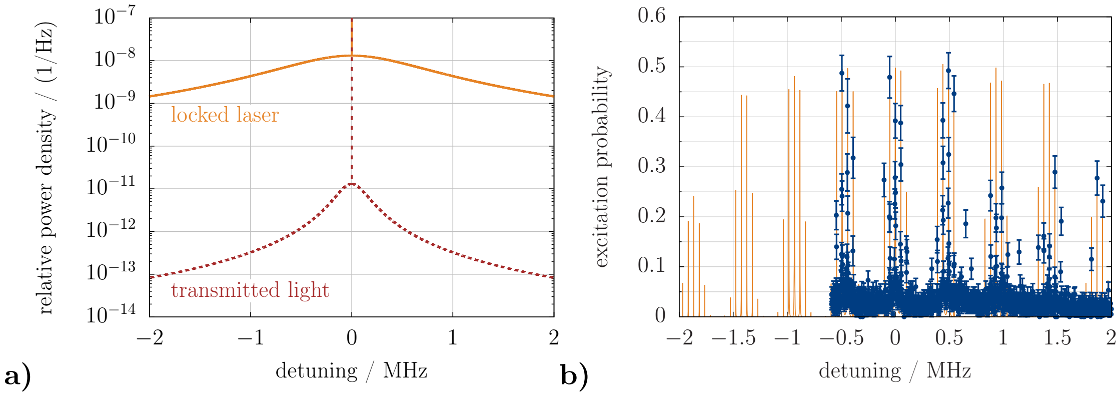

Figure 4.11.: Off-resonant excitation due to high frequency noise. **a)** estimated line shapes according to [118]. The power densities are normalized to the total power contained in the delta peak at the carrier frequency. **b)** Sideband spectrum recorded with 1 ms pulses and a free ion Rabi frequency of $\Omega_0 = 2\pi \times 7\,\text{kHz}$ (blue data points; see Ch. 5 for details). Between the narrow sideband resonances, off-resonant excitation produces a broad background signal. The orange line shows a calculated spectrum with these parameters for comparison.

In Eq. 4.4, ${}_2F_2$ denotes a generalized hypergeometric function and the normalization is chosen such that the absolute power contained in the delta peak is 1. The result is shown in Fig. 4.11a for $K = 1.3 \times 10^{-8}\,\mathrm{rad^2/Hz}$ and $f_0 = 700\,\text{kHz}$ (upper trace). For these parameters, the pedestal contains 3 % of the total optical power. The influence of this background can be observed experimentally, as Fig. 4.11b shows. Any change in the feedback gain is observed to increase this background, due to either weaker suppression of the intrinsic laser noise or excitation of the laser diode current modulation resonance at 1.2 MHz (cf. Fig. 4.9). Note that in order to emphasize the effect, the used power is much higher than necessary for the observation of most of the shown sideband transitions at this pulse duration.

If necessary, the background could be strongly suppressed by using the high-finesse cavity as an optical lowpass filter [119]. The corresponding frequency noise PSD and Allan deviation are shown in red in Fig. 4.9. Using again (4.3) to approximate the resulting phase noise PSD with $K = 1.3 \times 10^{-11}\,\mathrm{rad^2/Hz}$ and $f_0 = 160\,\text{kHz}$ yields the spectrum shown in Fig. 4.11a in red. Only 6×10^{-6} of the total power is contained in the pedestal in this case.

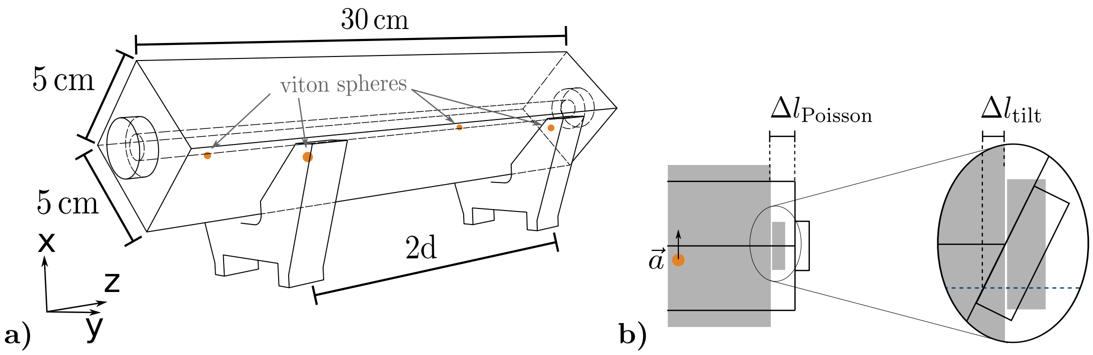

Figure 4.12.: Design for a vibration insensitive 30 cm long cavity. **a)** cuboid spacer resting on 4 viton spheres. **b)** the optical axis is displaced vertically to allow a cancellation of $\Delta l_{\text{Poisson}}$ by the tilt of the mirrors for vertical accelerations.

4.3. Clock laser cavity for ^{115}In$^+$

While the laser characterized in the previous section is sufficiently stable for its purpose, it would limit the instability of a clock based on the $^1\text{S}_0 \leftrightarrow {}^3\text{P}_0$ intercombination line in ^{115}In$^+$. This section describes the design and experimental characterization of a cavity for the clock laser stabilization, and the improvements compared to the ^{172}Yb$^+$ spectroscopy laser.

To achieve QPN limited interrogation in a clock with 100 ^{115}In$^+$ ions, an instability of $\sigma_y = 1 \times 10^{-16}$ needs to be reached at timescales on the order of 100 ms. Three of the frequency instability contributions seen in the previous section (cf. Fig. 4.1) have to be addressed in order to achieve this. The first, Schawlow-Townes noise, is expected to be lower for this system, as a frequency-quadrupled solid state (Nd:YAG) laser can be used to generate the light at 236.5 nm. The second limitation is the thermal noise floor, which is lowered to $\sigma_y = 9.4 \times 10^{-17}$ by choosing a spacer length of 30 cm. The third contribution to be addressed is the influence of vibrations. This section describes the vibration-insensitive spacer design which has been developed for this purpose and its experimental characterization using the laser described in the previous section.

4.3.1. Geometry and FEM calculations

The spacer design consists of a cuboid resting on viton spheres slightly below its vertical symmetry plane, as shown in Fig. 4.12a. The supports can be freely moved along the optical axis, as no machining of the spacer is necessary at their positions. The sensitivity to horizontal vibrations is suppressed by the symmetry of the support. This is not the case for vertical accelerations, where low sensitivities are achieved due to a cancellation of the Poisson effect

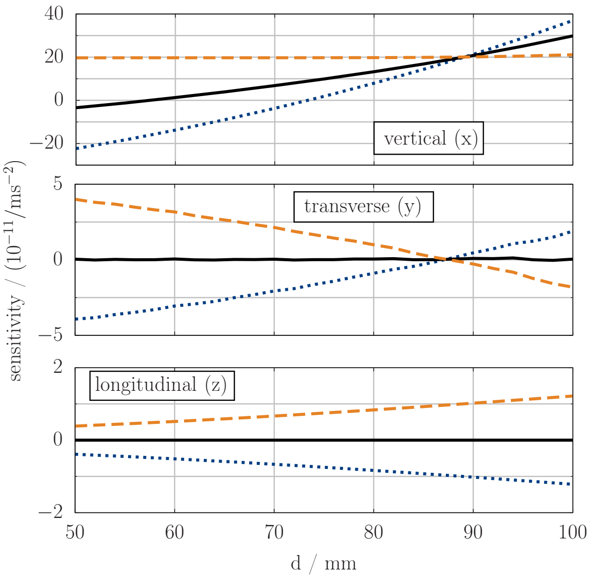

Figure 4.13.: Calculated sensitivities as a function of the longitudinal support positions. Top to bottom, the graphs show the sensitivity to vertical, transverse and longitudinal accelerations, respectively. Solid lines correspond to the experimentally implemented placement of the optical axis. Dashed/dotted lines show the effect of +0.45 mm / −0.55 mm vertical displacement, ±1 mm horizontal displacement, and ±2 mm/30 cm tilt, respectively.

by the tilt of the mirrors. Because of the 45 ° angle of the support plane, vertical accelerations deform the spacer in both the vertical and transverse direction. Assuming the forces to be equally distributed in the respective planes and adding up both components, the effect can be estimated by

$$\left(\frac{\Delta l}{l}\right)_{\text{Poisson}} = \frac{\nu\rho W}{\sqrt{2}E} a_x \,, \tag{4.5}$$

where ν denotes the Poisson ratio, ρ the density, E Young's modulus, W is the width of the spacer (measured along the short edges), and a_x the vertical acceleration. FEM calculations, performed in the range of $W = 3\ldots10\,\text{cm}$, agree with this approximation. Note that Eq. 4.5 is independent of the vertical support position, since its effects on the two contributions compensate each other. For the experimentally realized case of $W = 5\,\text{cm}$, the expected Poisson effect contribution is $1.9\times10^{-10}/\,(\text{ms}^{-2})$. If the cavity is supported within the inner 60 % of its length, the mirrors tilt around the vertical symmetry plane. Therefore, a vertical displacement of the optical axis is necessary for the tilt to have an effect on the effective resonator length that compensates for the Poisson effect, as illustrated in Fig. 4.12b.

The top graph of Fig. 4.13 shows the simulated sensitivity to vertical accelerations for coinciding optical and symmetry axes (dotted), and for an optical axis that is shifted downward by 0.55 mm (solid) and 1.00 mm (dashed). The experimentally realized displacement is 0.55 mm, resulting in a zero crossing at $d = 57\,\text{mm}$. The supports are placed $5/\sqrt{2}\,\text{mm}$ below the vertical symmetry plane. In the center and bottom panels, the solid lines show the sensitivities to transverse and longitudinal accelerations, respectively. The dashed and dotted lines show the effects of the most critical optical axis misalignments, which are a horizon-

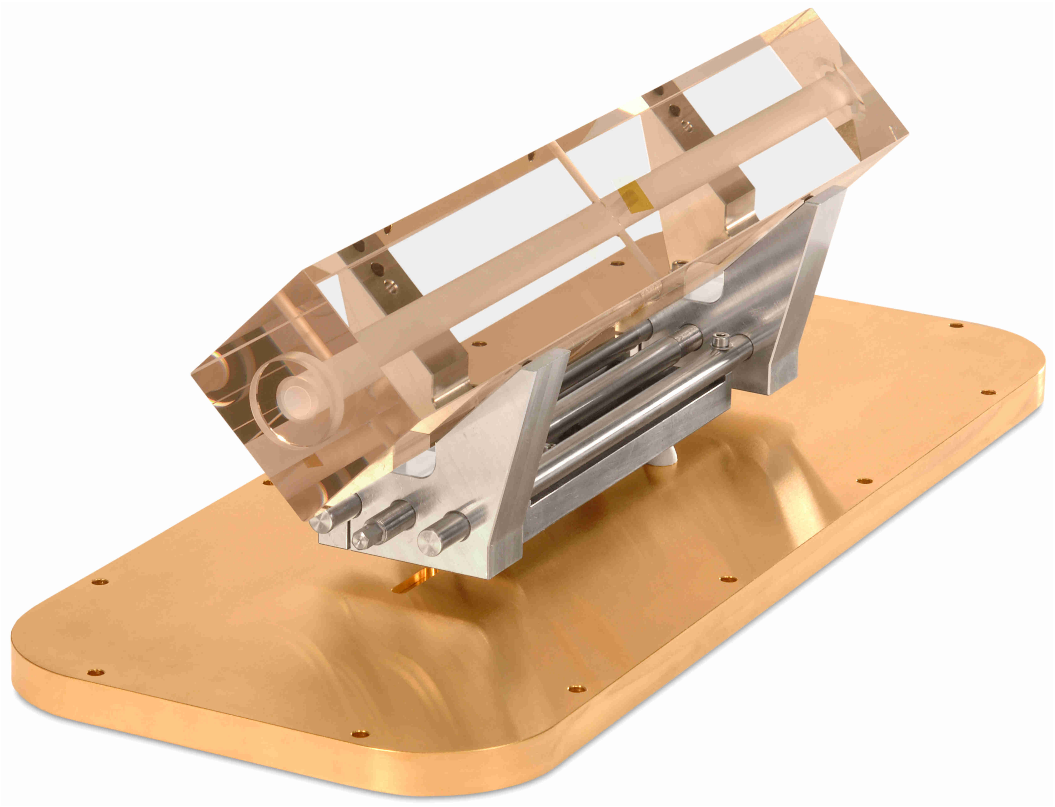

Figure 4.14.: Photo of the 30 cm cavity on the mount used to test its vibration sensitivity. The longitudinal support position can be adjusted using the central rod, which has fine threads with opposing orientation at its ends.

tal displacement ($\pm 1\,\mathrm{mm}$) for transverse and a vertical tilt ($\pm 2\,\mathrm{mm}/30\,\mathrm{cm}$) for longitudinal vibrations. The mirror positioning tolerances are rather relaxed: a transverse displacement leads to a sensitivity of at most $4 \times 10^{-12}\,\mathrm{ms}^{-2}$ per 0.1 mm, and the zero crossing of the vertical sensitivity shifts by 8 mm per 0.1 mm of vertical displacement. Due to the freely movable supports, this can easily be compensated; the slope around the zero crossing is $5 \times 10^{-12}/\,(\mathrm{ms}^{-2})$ per mm.

4.3.2. Experimental determination of the vibration sensitivity

Figure 4.14 shows a photo of the cavity on a mount with adjustable longitudinal support positions, which is used to measure the vibration sensitivity. In order to observe changes of the spacer length, the ^{172}Yb^{+} spectroscopy laser is used as the reference. For these measurements, 822 nm mirrors are contacted to the 30 cm spacer using an aluminium mask to ensure correct placement of the optical axis. Both the case of the optical axis coinciding with the symmetry axis and shifted downward by 0.55 mm are investigated. The accuracy of this method has been tested in the first case by a tactile determination of the mirror position, showing a displacement of 14 μm, which is negligible when compared to the tolerances given in the previous section.

The optical setup is shown in the shaded region in Fig. 4.7, omitting the PDH error signal generation, which is similar to the 12 cm cavity setup. Light from the stabilized laser is locked to the 30 cm cavity using an AOM, and the feedback signal – depicted as $\Delta\nu$ in the diagram – is used to deduce the relative frequency fluctuations between the cavities. A piezoelectric acceleration sensor for each dimension is placed on the vibration isolation platform and sinusoidal accelerations on the order of $5 \times 10^{-2}\,\mathrm{ms}^{-2}$ are applied for 120 s in each direction at the eigenfrequency of about 0.5 Hz. For evaluation, all signals are bandpass filtered and a least squares fit adjusts amplitudes of the sensitivity coefficients such that the weighted sum of the accelerations equals the frequency deviation. As expected for a rigid mount, the excitation frequency is far from any mechanical resonances and therefore no phase shift is observed. The scatter observed when repeating such a measurement without moving the cavity is below $4 \times 10^{-12}/\,(\mathrm{ms}^{-2})$.

Figure 4.15 shows the observed sensitivities to vertical accelerations when varying the longitudinal support position. As expected from the simulations, there is no dependence of the support position when the optical axis coincides with the symmetry axis. In the case of a displaced optical axis, the slope agrees with the simulations, and the minimum experimental value at $d = 73\,\mathrm{mm}$ is $1.8 \times 10^{-11}/\,(\mathrm{ms}^{-2})$. There is an overall offset of $9 \times 10^{-11}/\,(\mathrm{ms}^{-2})$ with respect to the simulations for both mirror configurations, which means that the tilt-independent length change is two times smaller than expected. Since the viton supports are not included in the model, this might be due to friction at the interface which reduces the transverse effect of vertical forces. As the sensitivity to accelerations in both horizontal directions only depends on the symmetry of the applied forces, both positive and negative values have been observed independently of the longitudinal support position. With careful alignment, values as low as $3.4 \times 10^{-12}/\,(\mathrm{ms}^{-2})$ have been achieved for both transverse and longitudinal accelerations.

The measurements shown here were performed with a rigid mount. Since the cavity is supported at four points, force imbalance leads to a scatter of $\pm 2 \times 10^{-11}/\,(\mathrm{ms}^{-2})$ (vertical), $\pm 5 \times 10^{-11}/\,(\mathrm{ms}^{-2})$ (longitudinal) and $\pm 1 \times 10^{-10}/\,(\mathrm{ms}^{-2})$ (transverse) when the cavity is removed and realigned between measurements at the same mount position. This could be reduced by including a force balancing mechanism in the mount, e.g. allowing one of the V mounts shown in Figs. 4.12a and 4.14 to tilt or translate in the y direction, thus reducing the geometry to an effective three-point support [98]. The symmetric scatter in the horizontal sensitivities, independent of the longitudinal support position, indicates that in principle, the

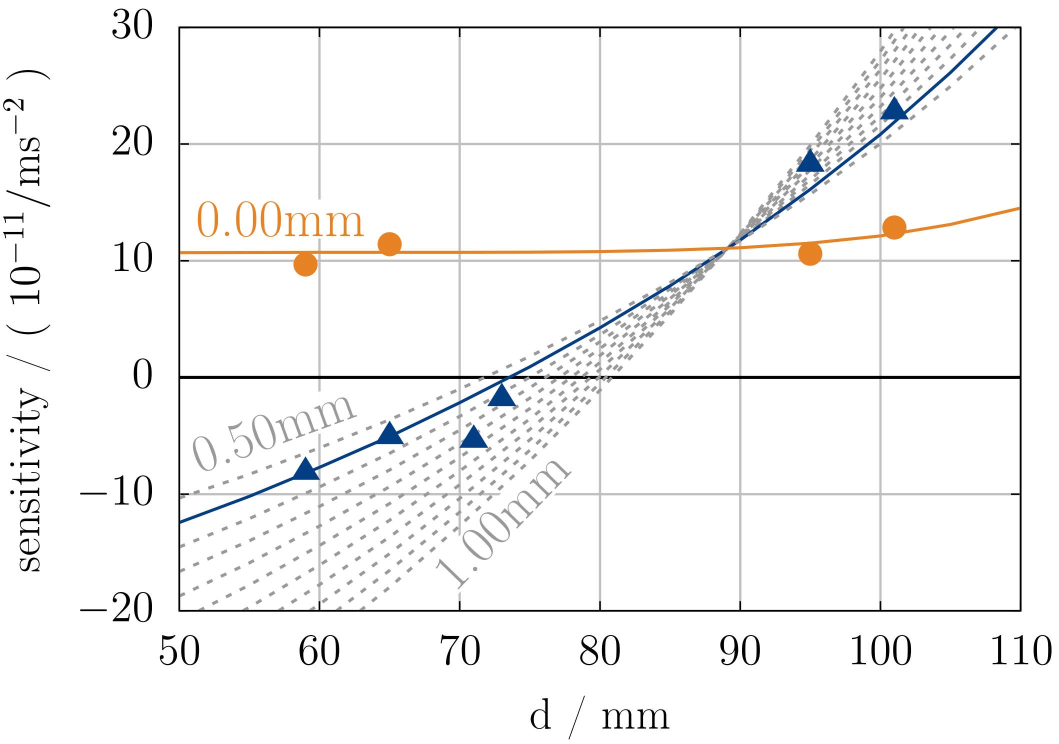

Figure 4.15.: Experimentally observed minimum sensitivity to vertical accelerations. Circles: optical axis coinciding with the symmetry axis. Triangles: optical axis 0.55 mm below the symmetry axis. The lines show FEM simulations for various axis displacements, shifted by $-9 \times 10^{-11} / (\mathrm{ms}^{-2})$ to account for effects not included in the model; the solid lines correspond to the experimentally tested configurations. Positive accelerations point along gravity. The uncertainty of $4 \times 10^{-12} / (\mathrm{ms}^{-2})$ of the sensitivity measurements is smaller than the symbols.

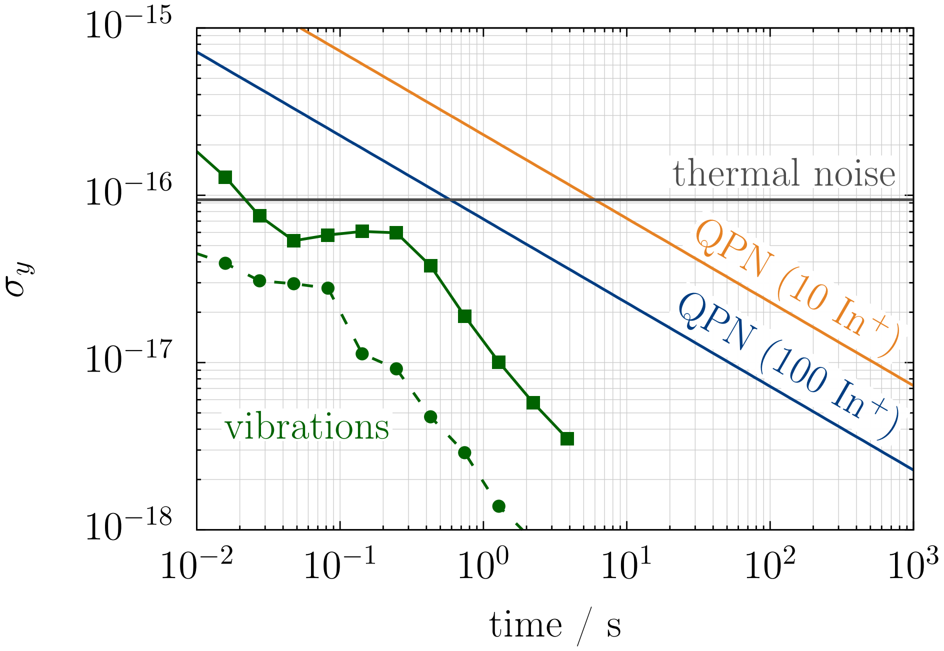

Figure 4.16.: Expected instability contributions due to thermal noise and vibrations compared with the quantum projection noise limit for 10 and 100 In^+ ions. The contributions are based on the minimum sensitivities observed simultaneously (squares: $1.8 \times 10^{-11}/(\mathrm{ms}^{-2})$ vertical, $6.3 \times 10^{-11}/(\mathrm{ms}^{-2})$ transverse, $8.5 \times 10^{-11}/(\mathrm{ms}^{-2})$ longitudinal) and individually (circles: $1.8 \times 10^{-11}/(\mathrm{ms}^{-2})$ vertical, $3.4 \times 10^{-12}/(\mathrm{ms}^{-2})$ transverse, $3.4 \times 10^{-12}/(\mathrm{ms}^{-2})$ longitudinal)

lowest sensitivities observed so far could be obtained simultaneously.

The expected instability contribution due to vibrations is shown in Fig. 4.16, calculated from the spectra shown in Fig. 4.2c and the lowest sensitivities observed simultaneously (squares) and individually for each dimension (circles). For comparison, the ideal case quantum projection noise limit for 10 and 100 In^+ ions, calculated according to [50], is shown.

In conclusion, even with its current rigid mount this cavity achieves sufficiently low vibration sensitivities for the QPN-limited operation of a frequency standard based on 100 $^{115}\mathrm{In}^+$ ions. This is facilitated by the fast feedback from the parallel interrogation of multiple ions. With the current mirrors, the instability of this cavity will be limited by thermal noise. Since a vibration contribution significantly below the thermal noise could be achieved for times $> 10\,\mathrm{ms}$ with the use of a force-balancing mount, a cavity based on this design would benefit from mirrors with reduced thermal noise contribution, e.g. due to higher-Q coatings [104]. This would be of use, e.g. for clocks based on narrower transitions.

5. Motional spectroscopy

Thermally excited secular motion results in a frequency shift of -1×10^{-18} due to time dilation in an $^{115}\mathrm{In}^+$ ion at 0.5 mK, the Doppler temperature of $^{172}\mathrm{Yb}^+$ (see section 2.3.1). Sufficiently precise knowledge of the temperature is therefore important to reduce the uncertainty of this shift to a negligible level. This chapter describes the application of the laser characterized in Ch. 4 for the measurement and manipulation of secular motion amplitudes. After an introduction of the addressed transition, experimental prerequisites and the general pulse sequence used for spectroscopy are introduced. The results include measurements of the Doppler temperature and the implementation of groundstate cooling to determine the low heating rates of the trap.

5.1. The $^2\mathrm{S}_{1/2} \leftrightarrow {}^2\mathrm{D}_{5/2}$ transition in Yb^+

An optical transition with linewidth well below the trap secular frequencies allows the spectroscopic resolution of motional sidebands and thereby provides a means to characterize and manipulate the motional state of the ions. In Yb^+, the electric quadrupole transition between the $^2\mathrm{S}_{1/2}$ ground and $^2\mathrm{D}_{5/2}$ state at 411 nm with a natural linewidth of 23 Hz fulfills this requirement. The term scheme of Yb^+ differs from lighter alkali-like ions, such as Ca^+, by the existence of the metastable $4f^{13}6s^2\ {}^2\mathrm{F}_{7/2}$ state, which can only decay to the ground state via an electric octupole transition and therefore has a lifetime on the order of 10 years [120]. Decay to this state is the main limitation of the $^2\mathrm{D}_{5/2}$ lifetime; the branching ratio is 0.83 compared to 0.17 for decay back to the ground state.

The 411 nm transition has been considered as a clock transition [121–123], but work with ytterbium in the past decade has concentrated on the narrower E2 transition to the $^2\mathrm{D}_{3/2}$ state (436 nm, 3 Hz) [124] and the extremely narrow E3 transition to $^2\mathrm{F}_{7/2}$ (467 nm, $\sim$ nHz) [15, 120].

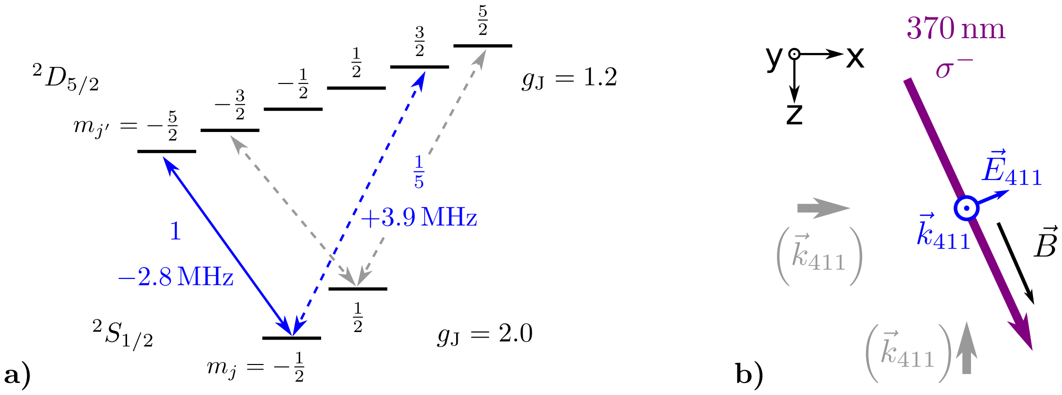

Figure 5.1.: Zeeman components and angular momentum selection rules. **a)** all experiments are performed on the $-\frac{1}{2} \leftrightarrow -\frac{5}{2}$ transition. The geometrical arrangement only allows $|\Delta m| = 2$ transitions. The values next to the transitions indicate the relative coupling strength and the Zeeman shift in a 100 μT magnetic field. The dashed grey arrows indicate the allowed transitions from the $m_j = +\frac{1}{2}$ substate, which are suppressed via optical pumping. **b)** top view of the geometry at the ion position. A horizontal beam at 370 nm is used for state preparation. Grey arrows indicate future beam paths for 3d spectroscopy.

5.2. Selection rules and geometrical considerations

The free-atom Rabi frequency for an electric quadrupole transition between states with total angular momenta j and j' can be expressed as [64]

$$\begin{aligned}\Omega_0^{(\mathrm{int})}(E, m_j, m_{j'}) = {} & E\frac{e}{\hbar\sqrt{c\alpha}}\sqrt{\frac{A}{k^3}}\sqrt{\frac{15(2j'+1)}{4}} \\ & \times \left|\sum_{\Delta m=-2}^{2}\begin{pmatrix} j & 2 & j' \\ m_j & \Delta m & -m_{j'}\end{pmatrix} c_{ij}^{(\Delta m)}\varepsilon_i^{(\Delta m)} n_j\right| ,\end{aligned} \tag{5.1}$$

where A denotes the Einstein coefficient, α the fine-structure constant, and $\vec{\varepsilon}$, $\vec{n}$ are unit vectors along the directions of $\vec{E}$ and $\vec{k}$, respectively. Explicit expressions for the tensor c can be found, e.g. in the appendix of [64] and in [73], along with a graphical representation. The experiments within this thesis are performed on the Zeeman component with $m_j = -1/2$, $m_{j'} = -5/2$, because it allows for a clean reduction to an effective two-level system and it is the energetically lowest transition from its initial state. The last condition eliminates the risk of heating by off-resonant excitation of blue sidebands from other components. For $|\Delta m| = 2$ transitions, the angular momentum coupling contribution to Eq. 5.1 is maximized if the light is linearly polarized and $\vec{k}$, $\vec{E}$ and $\vec{B}$ are mutually orthogonal. In that case, the $3j$-symbol and the tensor element each evaluate to $1/\sqrt{6}$.

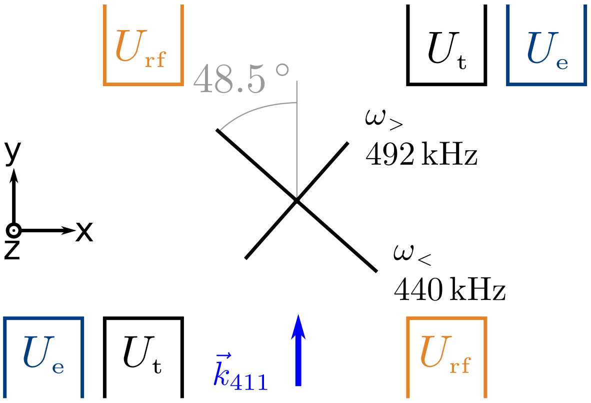

Figure 5.2.: Radial view of the trap. The vertical spectroscopy beam has projections on both radial principal axes. An additional voltage U_e will allow a rotation of the axes in future measurements in order to reduce the number of addressed modes.

Expressed in terms of optical power P and beam radii w_1, w_2 and inserting the atomic constants, the Rabi frequency becomes

$$\Omega_0^{(\mathrm{int})} \approx \sqrt{\frac{P/(w_1 w_2)}{1\mathrm{W/m}^2}} \times 2\pi \times 233\,\mathrm{Hz} \approx 2\pi \times 140\,\mathrm{kHz}\ , \tag{5.2}$$

where the experimental parameters $P = 1.8\,\mathrm{mW}$, $w_1 = w_2 = 70\,\mu\mathrm{m}$ have been used for the last step.

Figure 5.1a shows the allowed transitions and their relative strengths. The components can be addressed separately due to their spectral separation in an applied bias magnetic field. Transitions from the $m_j = +1/2$ substate are excluded by optical pumping on the 370 nm transition to the ${}^2\mathrm{P}_{1/2}$ state. The required σ^- light is provided by a circularly polarized beam propagating parallel to the magnetic field, as shown in Fig. 5.1b. All experiments in this chapter are performed with a vertical spectroscopy laser beam, while the H2 beam at 370 nm is used for optical pumping. For a future three-dimensional characterization of the ion motion, two additional horizontal beams at 411 nm will be introduced. Both the magnetic field and optical pumping beam can then be applied vertically.

While the optical access in the radial plane allows beams along the horizontal and vertical directions, the principal axes of the rf potential are currently rotated with respect to these directions, as illustrated by Fig. 5.2. As a consequence, $2N$ modes have projections onto $\vec{k}$ and contribute to the dephasing of Rabi oscillations in an N-ion crystal. While this is acceptable for the experiments with a single ion shown here, it would become a problem when the crystal size is increased. The next revision of the dc trap voltage electronics will therefore allow a common bias voltage U_e to be applied to the outer compensation electrodes. With this additional degree of freedom, the radial static potential can be used to define principal axes oriented along the x and y directions.

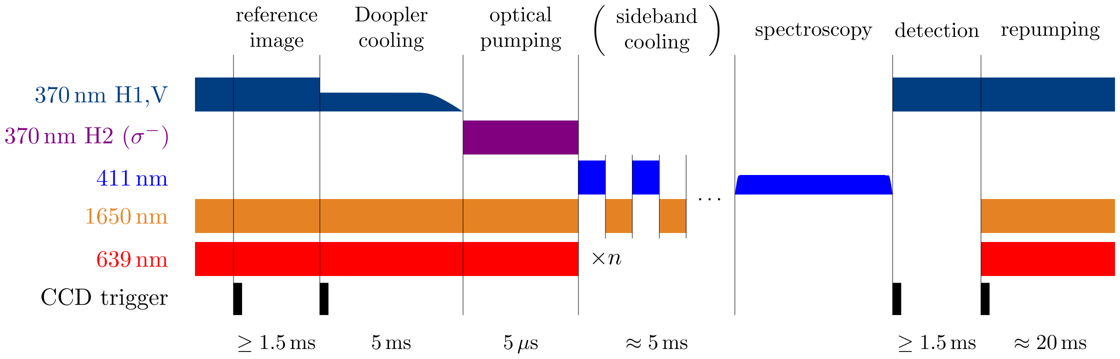
reference image
Doppler cooling
optical pumping
(sideband cooling)
spectroscopy
detection
repumping
370 nm H1,V
370 nm H2 (σ^-)
411 nm
1650 nm
639 nm
CCD trigger
$\times n$
...
≥ 1.5 ms
5 ms
5 μs
≈ 5 ms
≥ 1.5 ms
≈ 20 ms

Figure 5.3.: General composition of the spectroscopy sequences. Most of the experiments are performed at Doppler temperature; sideband cooling is only used in the measurements described in section 5.5. See Fig. 5.4 below for an overview of the transitions involved in repumping.

5.3. Spectroscopy sequence and experimental prerequisites

5.3.1. The spectroscopy sequence

Figure 5.3 shows the general spectroscopy sequence, which is repeated 200 times for each set of parameters in a typical experiment. A reference image in the beginning is used to determine whether ions were initially in the ground state. Cycles with dark reference images are discarded individually for each ROI. While images are taken with high intensity at 370 nm to increase the count rate, the power is reduced for Doppler cooling to achieve a low temperature. The light is switched off in a 1 ms ramp to prevent motional excitation due to a jump of the equilibrium position as the radiation pressure vanishes.

Next, a short pulse of σ^- light pumps all population to the $m_j = -1/2$ substate. Its parameters are optimized by minimizing the excitation on the $m_j = +1/2$, $m_{j'} = +5/2$ transition. The duration of 5 μs is chosen conservatively. Since on average only two photons need to be scattered, no significant heating is expected due to the optical pumping pulse. Sideband cooling is described in 5.5; it is omitted in all other experiments. After these preparations, a Blackman pulse of variable length, detuning and power is used to probe the quadrupole transition. It is followed by a detection image and about 20 ms of repumping time before the sequence is repeated. The only critical powers in the sequence are those of the Doppler cooling pulse and the pulses at 411 nm. They are stabilized using sample-and-hold PI controllers and 100 ms sampling pulses once every 200 cycles.

5.3.2. Repumpers

Since an excitation on the 411 nm transition leads to population of the metastable $^2\mathrm{F}_{7/2}$ state 83 % of the time, a fast and reliable way to return these ions to the ground state is essential for the experiments. Because the same issue is faced by optical clocks based on both the 411 nm and 467 nm transitions, different repumping schemes have been investigated. Experiments at NPL compared the 639 nm $^2\mathrm{F}_{7/2} \leftrightarrow {}^1[5/2]_{5/2}$ and the 864 nm $^2\mathrm{F}_{7/2} \leftrightarrow {}^3[5/2]_{3/2}$ E2 transitions, concluding that the former is more efficient [122]. The $^1[5/2]_{5/2}$ state has two dipole allowed decay channels. Part of its population ends up in the $^2\mathrm{D}_{3/2}$ state, from where it is returned to the ground state by the 935 nm transition also needed for Doppler cooling. The more problematic decay is to the $^2\mathrm{D}_{5/2}$ level, as it is likely to lead back to $^2\mathrm{F}_{7/2}$. Besides taking up time, these cycles can lead to the population of Zeeman substates which are not addressed as efficiently by the 639 nm laser. This problem is even more pronounced in odd isotopes such as $^{171}\mathrm{Yb}^+$, where the other hyperfine sublevel of $^2\mathrm{F}_{7/2}$ can be populated this way [125].

The strengths of the decay channels from the $^1[5/2]_{5/2}$ state are unknown, because the lines cannot be observed directly in trapped-ion experiments and are too weak to be seen in emission lamp spectra. The measurements at NPL gave an upper bound on the state's lifetime of 160 ms [123]. Measurements at the PTB $^{171}\mathrm{Yb}^+$ clock showed a longer effective lifetime of 250 ms for the $^2\mathrm{F}_{7/2}$ state when the repumper at 639 nm is used [35], the suspicion being that the radiation at 411 nm present during the NPL experiments mitigated the cycling issue by stimulated emission back to the ground state [1].

Figure 5.4 illustrates the repumping scheme used in the experiments presented here: light at 639 nm is used in combination with a laser at 1650 nm, which clears out the $^2\mathrm{D}_{5/2}$ state via the short-lived $^2\mathrm{P}_{3/2}$ level. 639 nm radiation with a power of 4.6 mW is focused to about 125 μm at the ion position. At 1650 nm, 2 mW are available at the ion position, similarly focused. The transition frequencies are found by simultaneously illuminating the ion with the repumpers and the 411 nm laser and maximizing the mean fluorescence observed on the Doppler cooling transition. In this way, the frequency of the $^2\mathrm{D}_{5/2} \leftrightarrow {}^2\mathrm{P}_{3/2}$ transition was determined to be

$$\nu\left({}^2\mathrm{D}_{5/2} \leftrightarrow {}^2\mathrm{P}_{3/2}\right) = 181.65947(19)\,\mathrm{THz}\,, \tag{5.3}$$

corresponding to 1650.2991(17) nm, using a wavemeter stabilized to a HeNe laser[2].

The efficiency of the repumpers is characterized with a measurement of the clearout times. Starting from the ground state, the ion is first excited on the 411 nm transition. If no fluorescence is observed on the 370 nm transition after 100 ms, it is considered to have decayed

---

[1] For the PTB $^{171}\mathrm{Yb}^+$ clock, the issue was resolved by switching to the 760 nm E2 transition to the $^1[3/2]_{3/2}$ state, which decays directly to the ground state, achieving an effective lifetime of 1.6 ms [15, 35].

[2] Bristol Instruments 228

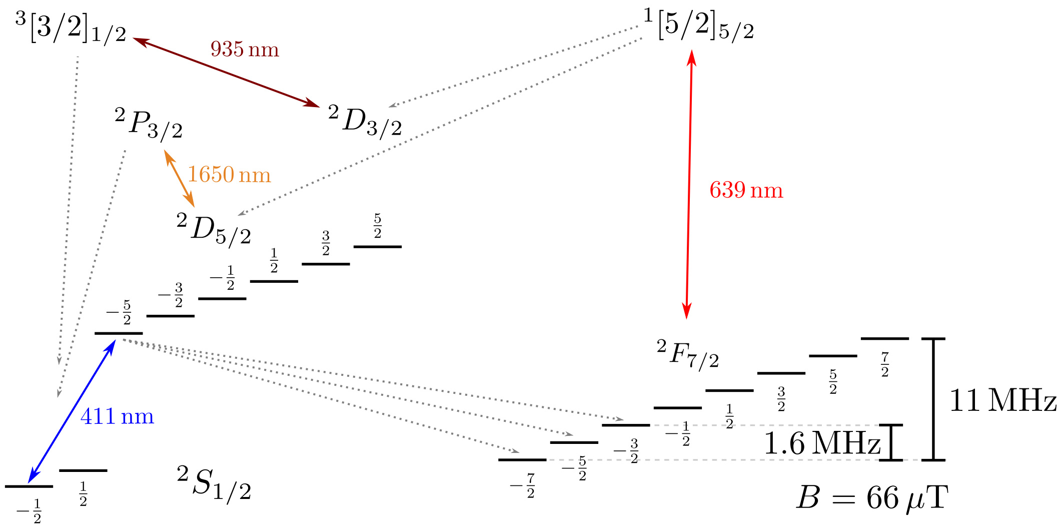
$^3[3/2]_{1/2}$
935 nm
$^1[5/2]_{5/2}$
$^2P_{3/2}$
$^2D_{3/2}$
1650 nm
639 nm
$^2D_{5/2}$
$-\frac{5}{2}$
$-\frac{3}{2}$
$-\frac{1}{2}$
$\frac{1}{2}$
$\frac{3}{2}$
$\frac{5}{2}$
$^2F_{7/2}$
$-\frac{7}{2}$
$-\frac{5}{2}$
$-\frac{3}{2}$
$-\frac{1}{2}$
$\frac{1}{2}$
$\frac{3}{2}$
$\frac{5}{2}$
$\frac{7}{2}$
11 MHz
1.6 MHz
411 nm
$-\frac{1}{2}$
$\frac{1}{2}$
$^2S_{1/2}$
$B = 66\,\mu$T

Figure 5.4.: Transitions involved in clearing out the ^{2}F$_{7/2}$ state. The decay channel $^1[5/2]_{5/2} \rightarrow$ ^{2}D$_{5/2}$ can lead to cycling and population of further detuned ^{2}F$_{7/2}$ Zeeman substates. Adding a laser at 1650 nm to directly clear out the ^{2}D$_{5/2}$ state speeds up repumping and makes it more reliable.

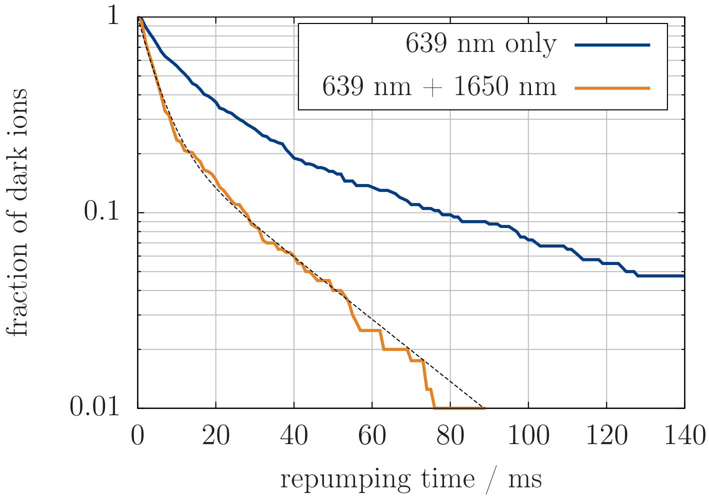

Figure 5.5.: Characterization of the ^{2}F$_{7/2}$ state clearout. The transition at 1650 nm prevents cycling, which can otherwise occur after the ion has decayed back to the ^{2}D$_{5/2}$ state. Besides slowing down the process, these cycles can populate Zeeman sublevels not covered by the 639 nm laser. The dashed line is a double-exponential decay fit to the data with time constants of 5 ms (74 %) and 27 ms (26 %).

to the $^2\mathrm{F}_{7/2}$ state and the repumpers are switched on. A histogram of the time intervals until fluorescence is restored then allows the determination of an effective lifetime. Fig. 5.5 shows the deduced fractions of dark ions as a function of time from 400 measurements each with and without the 1650 nm laser.

In the applied bias magnetic field of 66 μT, the $^2\mathrm{F}_{7/2}$ sublevels are spread over 11 MHz, while the three substates which are accessible by decay from $^2\mathrm{D}_{5/2}$, $m_{j'} = -5/2$ lie within 1.6 MHz of each other. The injection current of the laser diode at 639 nm is modulated at a frequency of 1 kHz to control the spectral coverage of these substates. The amplitude of this modulation needs to be chosen as a compromise between clearout speed of the frequently populated substates and coverage of the further detuned ones, and has been experimentally optimized to ± 2 MHz. With only the 639 nm laser, a remaining 1 % of the ions stay dark indefinitely, while with both lasers on, the ion was returned to the groundstate after at most 130 ms in all of the 400 runs.

The dashed curve in Fig. 5.5 shows that the data obtained with the 1650 nm light present can be approximated by a double-exponential decay. The fitted time constants are 5 ms (74 %) and 27 ms (26 %), setting a new upper bound on the $^1[5/2]_{5/2}$ lifetime. Since 75 % of the population decaying from $^2\mathrm{D}_{5/2}$, $m_{j'} = -5/2$ to $^2\mathrm{F}_{7/2}$ end up in the $-7/2$ substate, the fast process is likely due to repumping from this state.

These measurements show that the repumping time is currently limited by the power at 639 nm. Laser diodes with four times more output power have become available since the system was set up and a replacement is planned for future measurements.

5.3.3. Zeeman components and secular sidebands

The correct Zeeman component of the transition is identified by observing the relative shifts of lines as the magnetic field amplitude is varied. Figure 5.6 shows a coarse scan over both $|\Delta m| = 2$ lines from $^2\mathrm{S}_{1/2}$, $m_j = -1/2$ at a bias field of 66 μT. Due to the temperature of 1.3 mK, strong excitation on the secular sidebands can be seen. Increasing the spectral resolution with the use of longer pulses at lower power allows the frequency splitting of the radial modes to be resolved, as shown in Fig. 5.7. Besides the individual mode sidebands, transitions involving the simultaneous interaction with both modes can be seen.

5.3.4. Magnetic field

The magnetic field at the ion position can be controlled by three pairs of coils in approximate Helmholtz configurations. Changes in the magnetic field orientation can deteriorate the optical pumping process and weaken the transition strength of the spectroscopy Zeeman

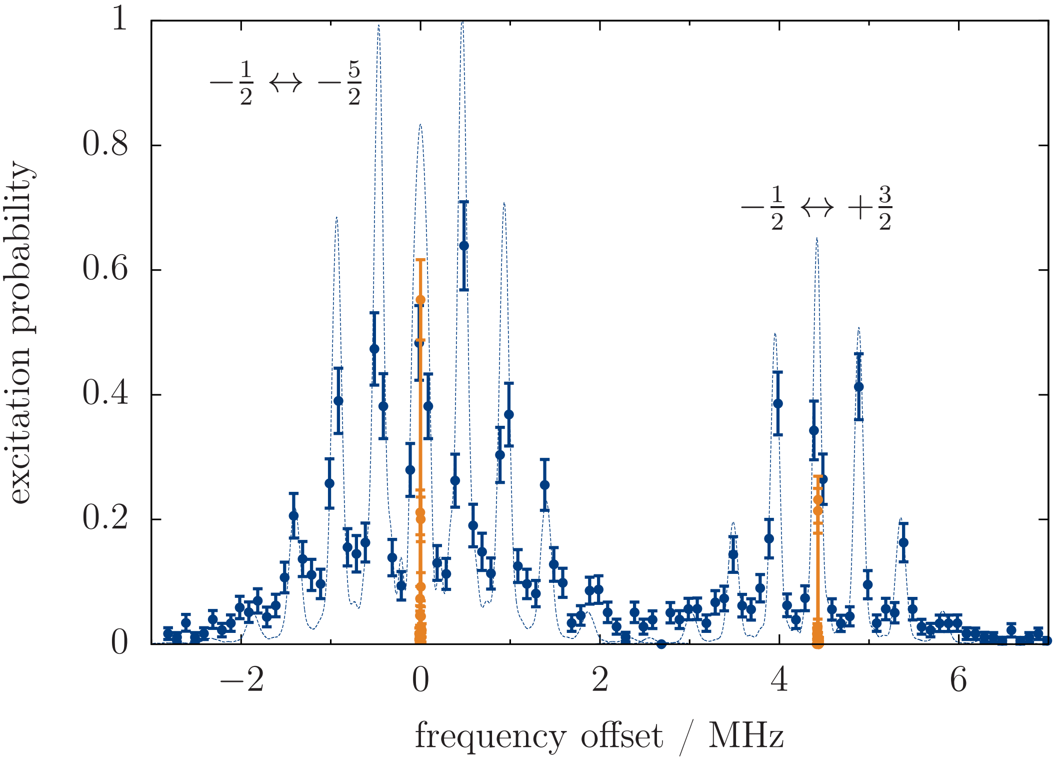

Figure 5.6.: Coarse scan of the $\Delta m = \pm 2$ transitions from the $m_j = -1/2$ state at a temperature of 1.3 mK. 10 μs pulses with a power corresponding to $\Omega_0^{(\mathrm{int})} = 2\pi \times 140$ kHz are used for the blue data points. The relative shift between the Zeeman components is 4.4 MHz, as expected for the applied bias field of $B = 66\,\mu$T. The dotted lines show the calculated spectra for these parameters. Between the peaks, the background due to off-resonant excitation from high-frequency laser noise is visible (cf. section 4.2.5). The orange data points show a more precise determination of the carrier transitions with strongly attenuated 1 ms pulses.

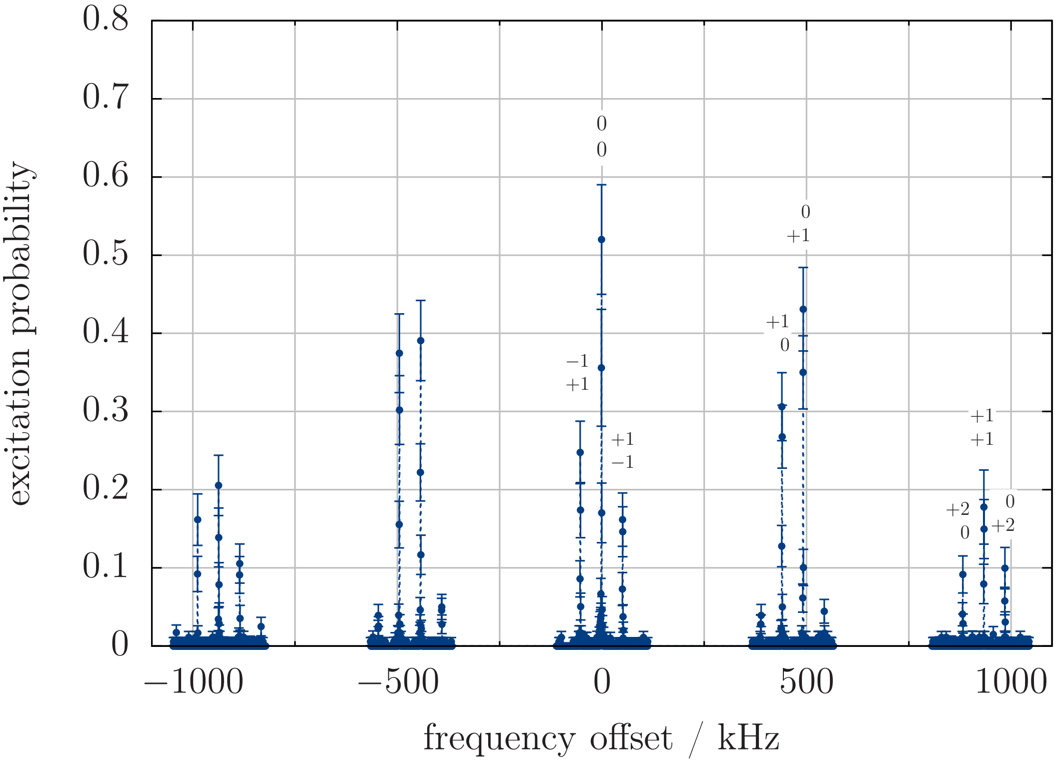

Figure 5.7.: Scan of the $m_j = -1/2$, $m_{j'} = -5/2$ transition sideband spectrum with higher resolution. Pulses with a duration of 875 μs and an intensity corresponding to $\Omega_0^{(\mathrm{int})} = 2\pi \times 700\,\mathrm{Hz}$ were used to obtain this spectrum. Besides the sidebands of the two different radial modes, transitions which transfer energy between the modes appear at multiples of the frequency difference. The respective change in phonon number is indicated for the most pronounced transitions (top number: 440 kHz mode, bottom number: 492 kHz mode)

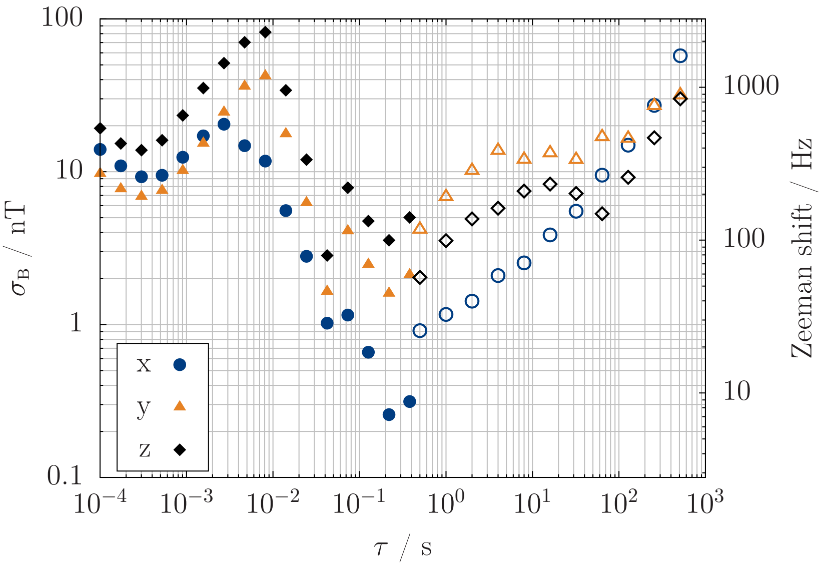

Figure 5.8.: Allan deviation of the ambient magnetic field as measured with a fluxgate. Closed and open symbols indicate measurements with different temporal resolutions. The right ordinate shows the corresponding Zeeman shift of the $m_j = -2/1$, $m_{j'} = -5/2$ transition with a sensitivity of $-28\,{}^{\mathrm{Hz}}\!/_{\mathrm{nT}}$.

component. Long-term drifts of the external field are therefore compensated with the help of the ${}^2\mathrm{D}_{3/2} \leftrightarrow {}^3[3/2]_{1/2}$ transition at 935 nm: Since only $\Delta m = 0$ transitions are allowed in zero field, the outer substates of the ${}^2\mathrm{D}_{3/2}$ level become dark states under this condition. By minimizing the fluorescence during Doppler cooling, the coil currents for compensating the external field can be found. A more detailed description of the underlying process can be found, e.g. in [120, 121]. The currents are then adjusted to produce a field of 66 μT along the H2 direction, a value chosen as a compromise between sufficient separation of the spectroscopy transition Zeeman components and tolerable heat generation from the coils.

External magnetic field fluctuations on shorter timescales affect spectroscopy by changes of the Zeeman shift, which has a magnitude of $-28\,{}^{\mathrm{Hz}}\!/_{\mathrm{nT}}$ for the interrogated component. This presents a limit for the measurement of weak sideband transitions, as signals are affected when the changes in detuning between individual experimental cycles become comparable to the Rabi frequency. In order to estimate this limit, the fast external magnetic field fluctuations have been measured with a fluxgate magnetometer. The corresponding Allan deviation is shown in Fig. 5.8. The strong peak around averaging times of $\tau = 10$ ms is the result of fluctuations with the mains frequency of 50 Hz. To reduce the influence of this component and its harmonics, the individual cycles are synchronized to the mains. There are, however, similar contributions at other Fourier frequencies which lead to shifts on the order of several

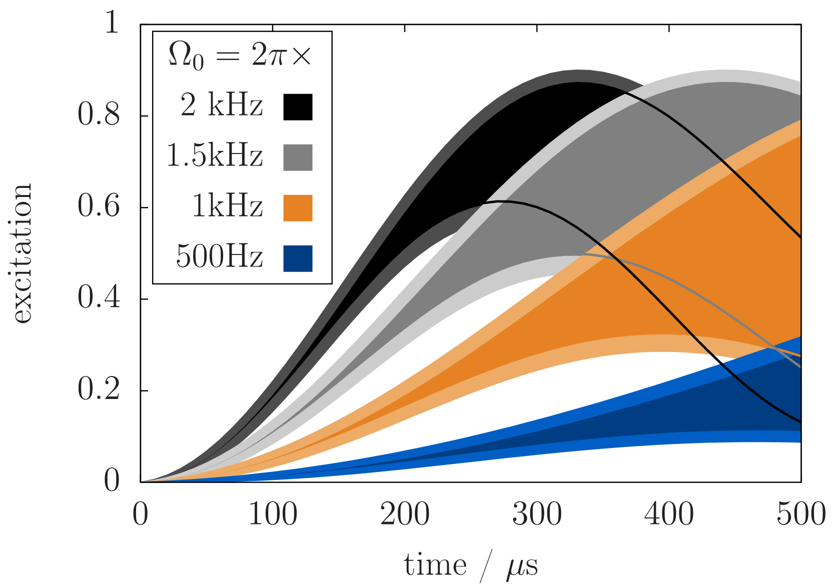

Figure 5.9.: Illustration of the Rabi frequency resolution limit at $T = 0.5\,\mathrm{mK}$ due to magnetic field fluctuations. The areas between resonant Rabi oscillations and the evolution at a detuning of 1 kHz are shown for four different free ion Rabi frequencies. The lighter areas show the additional broadening due to shot noise, assuming 150 valid cycles each. Magnetic field fluctuations between individual cycles cause a scatter of the measured points within these areas, limiting the lowest discernible difference in sideband strength.

100 Hz between individual cycles. The effect of these fluctuations is illustrated in Fig. 5.9, which shows the range between thermal Rabi oscillations on resonance and detuned by 1 kHz. As measured excitation probabilities will scatter within these areas, their width determines the closest distinguishable Rabi frequencies. The scatter is increased further by shot noise, which is shown by the lightly colored areas, assuming 150 valid experimental cycles each. The current resolution is therefore limited to slightly below the shown 500 Hz. In a future setup, magnetic shielding of the trap will be used to improve this limit.

5.4. Temperature measurements after Doppler cooling

The temperature after Doppler cooling as well as the free ion Rabi frequency $\Omega_0^{(\mathrm{int})}$ can be inferred from fits to the temporal evolution of the excited state population during carrier excitation. By comparison with calculated curves, an upper bound of 0.1 mK is assumed for the uncertainty of the derived temperature. Figure 5.10 shows an example for two Doppler cooling geometries. Since the H1 beam has a low projection of ≈ 0.3 onto the radial principal

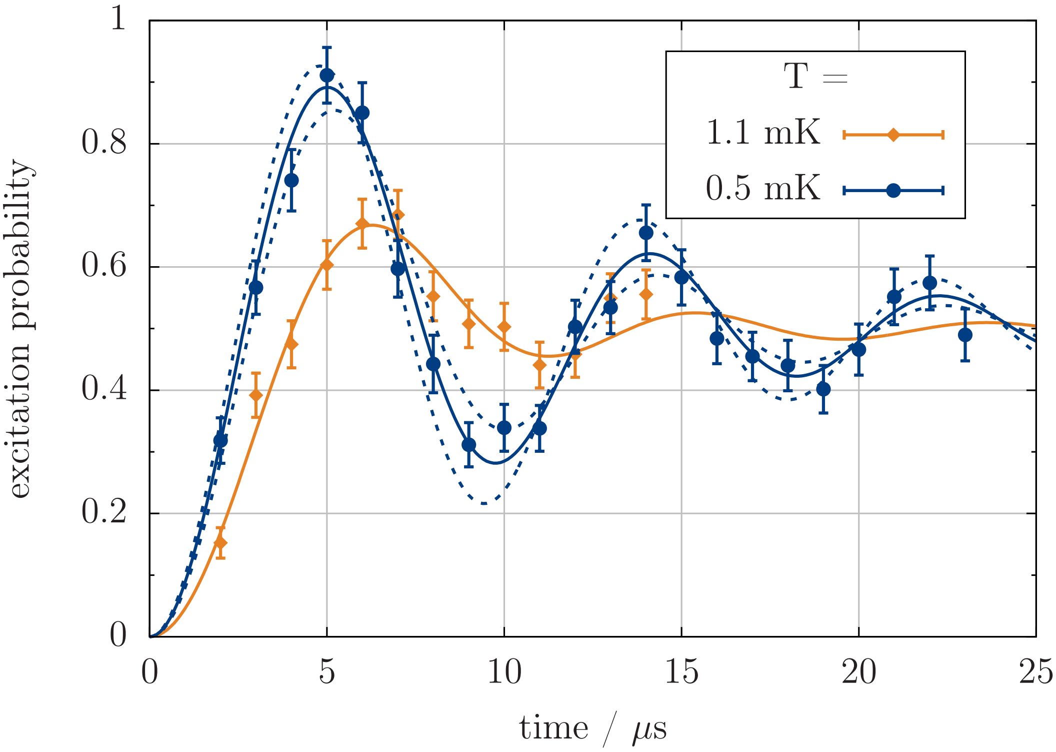

Figure 5.10.: Rabi oscillations on the carrier transition after Doppler cooling. Due to the small projection onto the radial principal axes, Doppler cooling with a laser along H1 only reaches a temperature of 1.1 mK, whereas cooling along the V direction[3] allows a temperature close to the Doppler limit of 0.5 mK. The fitted free ion Rabi frequency is $\approx 2\pi \times 130$ kHz in both cases. Dashed lines indicate the estimated uncertainty interval of ±0.1 mK.

axes, the achieved temperatures of the respective modes are more than a factor of two above the Doppler limit [47]. With the cooling light applied along the V direction[3], the more favorable projections of ≈ 0.7 allow temperatures close to the theoretical limit. The calculated evolution for temperature differences $\pm 0.1\,\mathrm{mK}$ is indicated by the dashed lines for the $0.5\,\mathrm{mK}$ data.

In order to distinguish the temperatures of different modes, a selection of sidebands can be probed at the respective pulse areas with maximized temperature sensitivity (cf Fig. 2.6). Such a measurement has been tested for the two radial modes, but the current implementation adjusts the pulse area by varying the time and therefore suffers from magnetic field induced decoherence when a combination of strong and weak transitions is probed. Measurements which vary the power instead will improve the resolution of this technique.

5.5. Sideband cooling

Since its first implementation about 25 years ago [126], resolved sideband cooling (SBC) has become a commonly employed technique to reach sub-Doppler temperatures with trapped ions. The basic principle is illustrated in Fig. 5.11a: By exciting the ion on an RSB transition, energy is removed from the motional degree of freedom. Since spontaneous emission occurs mainly on the carrier transition in the Lamb-Dicke regime, a net loss in motional energy is achieved with each absorption–emission cycle. Once an ion reaches the motional ground state, the red sidebands vanish and no more absorption takes place. The minimal temperature achievable in this way is limited by heating processes from off-resonant excitation of the carrier and BSB transitions. Because a narrow transition, as is required for resolving the sideband structure, requires a long-lived excited state, the cooling rate is usually increased by adding a controllable fast decay channel via a second transition. Fig. 5.11b shows an implementation in Yb^+: Sidebands are addressed with the 411 nm quadrupole transition, and the ${}^2\mathrm{D}_{5/2}$ state is subsequently cleared out via an excitation to the short-lived ${}^2\mathrm{P}_{3/2}$ state with a photon at 1650 nm.

An ideal pulsed SBC scheme would consist of π pulses at 411 nm, each followed by a short pulse at 1650 nm. Achieving a consistent pulse area of π is prevented by the motional state dependence of the Rabi frequencies (see Fig. 2.5) and the fact that the ion occupies a thermal distribution of states after Doppler cooling. Besides a spread of optimal pulse durations for the initial distribution, this dependence leads to a temporal change in the optimal parameters as the temperature is lowered. The chosen sequence consists of 150 pulses on the 2nd-order RSB of each mode, followed by 200 pulses on each 1st-order RSB. The high number of pulses is necessary due to the low secular frequencies, which lead to high mean occupation numbers

---

[3] A weak H1 beam is added to prevent heating of the axial mode.

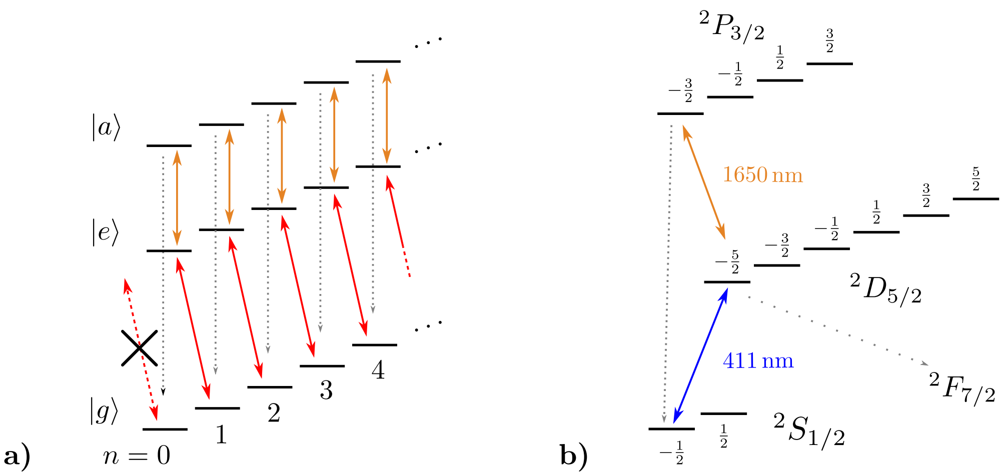

Figure 5.11.: Sideband cooling scheme. **a)** general concept of sideband cooling: a narrow transition is used to selectively excite a red sideband transition $|g\rangle \rightarrow |e\rangle$. Energy is dissipated in subsequent carrier decay. The lifetime of the metastable state $|e\rangle$ is shortened with the help of a transition to the short-lived auxiliary state $|a\rangle$. **b)** actual states used for the scheme implemented here. The decay channel $^2\mathrm{D}_{5/2} \rightarrow {}^2\mathrm{F}_{7/2}$ leads to losses in the pulsed scheme.

of $\bar{n} \approx 50$ after Doppler cooling[4]. All pulse durations, including the 1650 nm repump pulses, were experimentally optimized to about 10 μs each.

The relatively high amount of time spent in the $^2\mathrm{D}_{5/2}$ level during SBC leads to a $^2\mathrm{F}_{7/2}$ population of 0.18(5), which shows up as a background in subsequent experiments. It can be eliminated by shining in the 639 nm laser during the cooling sequence, but this could have a negative effect on the motional state distribution, since the ions returned to the ground state this way have not taken part in all of the cooling cycles.

These losses could be reduced in a much better way by employing a cooling scheme with shorter dwell times in the $^2\mathrm{D}_{5/2}$ state. Continuous SBC [127], where the effective lifetime of the $^2\mathrm{D}_{5/2}$ state is controlled by mixing it with the $^2\mathrm{P}_{3/2}$ state, seems most appropriate. The amount of this “quenching” presents a compromise between fast cooling and minimum temperature, as broadening the 411 nm transition increases the probability of off-resonant carrier and BSB excitation. An optimized sequence would consist of a sweep from strong to weak quenching as the ion temperature decreases. Such a scheme requires a controlled

---

[4] These experiments were performed at a time when the 370 nm AOM setup only allowed cooling pulses along H1, with which the radial temperatures are well above the Doppler limit due to the weak projections onto the respective principal axes. Starting from a temperature of 0.5 mK ($\bar{n} \approx 20$), as obtained with the optimized cooling geometry, the total number of SBC pulses is reduced to 120 per mode.

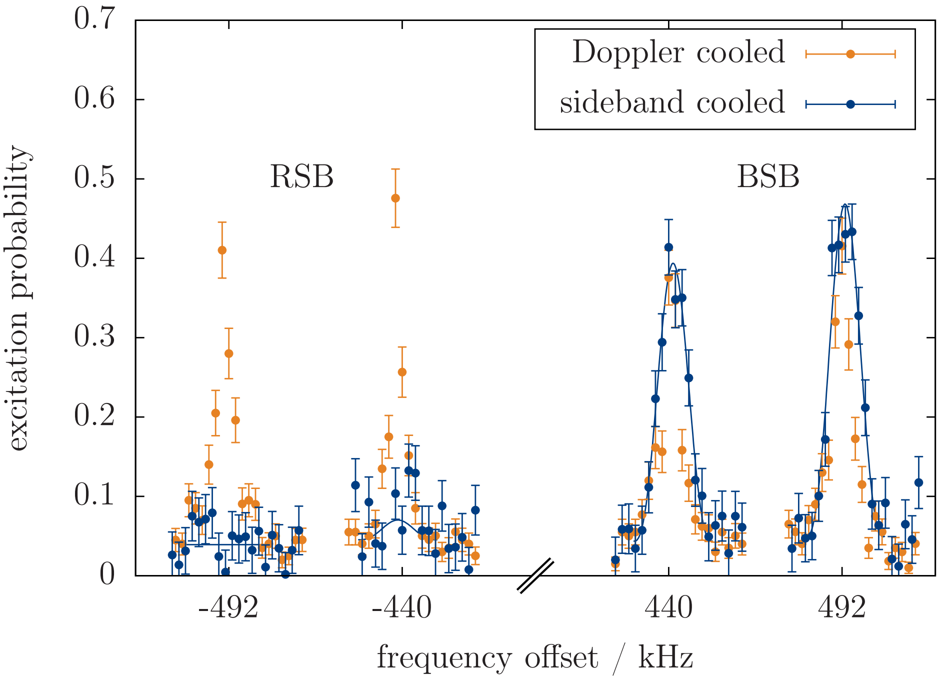

Figure 5.12.: Comparison of sideband excitations for both radial modes before and after sideband cooling. A background of 0.18 due to decay to $^2F_{7/2}$ during sideband cooling has been subtracted. Note that the spectrum after Doppler cooling was recorded with different pulse parameters and only serves to show the spectral positions of the sidebands.

quench laser detuning. Since 1650 nm is outside the range of the wavemeter used for laser stabilization (cf. section 3.2.3), an SHG has meanwhile been set up to obtain a signal at 825 nm. Because this was not available at the time of the experiments described here, the pulsed SBC scheme was used instead.

Figure 5.12 shows the 1st-order sidebands of both radial modes before and after SBC. The mean occupation numbers are $\bar{n} = 0.48(35)$ (440 kHz mode) and $\bar{n} = 0.18(18)$ (492 kHz mode). Further reduction of the temperature was not attempted due to the high amount of losses and the prospect to switch to the continuous scheme in the near future.

5.5.1. Heating rate measurement

During clock spectroscopy, off-resonant radiation at the clock ion positions needs to be suppressed to avoid AC-Stark shifts. Although the Coulomb crystal approach allows the use of dedicated cooling ions, cooling during clock interrogation would require single-ion addressing, which is not easily scalable and bears the risk of straylight-induced frequency shifts. Ideally, clock interrogation therefore takes place without simultaneous cooling. To reduce the 2nd-order Doppler shift from secular motion and IMM (see 2.3.1), the temperature during interrogation should be low and constant. Together, these requirements can only be fulfilled if external heating in the trap is negligible on the timescale of the interrogation.

External heating is caused by fluctuating electric fields resonantly coupling to the secular motion of the ions. The small spatial extension of Coulomb crystals compared to their distance to the trap electrodes means that fluctuations mainly produce in-phase forces on the individual ions. The secular modes most prone to external heating are therefore those in which all ions move in phase, i.e. the COM modes in a single-species crystal.

There are multiple sources of fluctuating electric fields in the relevant frequency range [31]. The dominant contributions are suspected to be due to fluctuating patch potentials on the electrode surfaces, pickup of external electromagnetic noise by the electronics supplying the trapping voltages, and Johnson-Nyquist noise. While these processes follow different scaling laws, heating rates are in general expected to decrease with larger electrode–ion distance d [76, 128], higher secular frequency, and a lower temperature of the apparatus [129]. Direct measurements of the scaling with d suggest that the main source of heating is typically due to patch potentials [76, 128], which is supported by the decrease of heating rates observed after in-situ cleaning with UV radiation [130] and argon-ion bombardment [131].

Low heating rates are expected for the trap used in this setup because of the rather large value of $d \approx 0.7\,\mathrm{mm}$ and the lowpass filtering directly on the trap wafers. Since no fast shuttling operations are necessary, variations of the trap DC voltages can be filtered with a cutoff frequency of only 113 Hz, suppressing electronic noise at the secular frequencies by 3 to 4 orders of magnitude.

Experimentally, the heating rates are determined by adding a variable waiting period between groundstate cooling and temperature determination. The result is shown in Fig. 5.13 for both radial modes. Table 5.1 contains the heating rates as derived from linear fits to the data and the deduced electric field noise PSDs [76].

In the absence of cooling, the energy transferred to the ion increases the 2nd-order Doppler

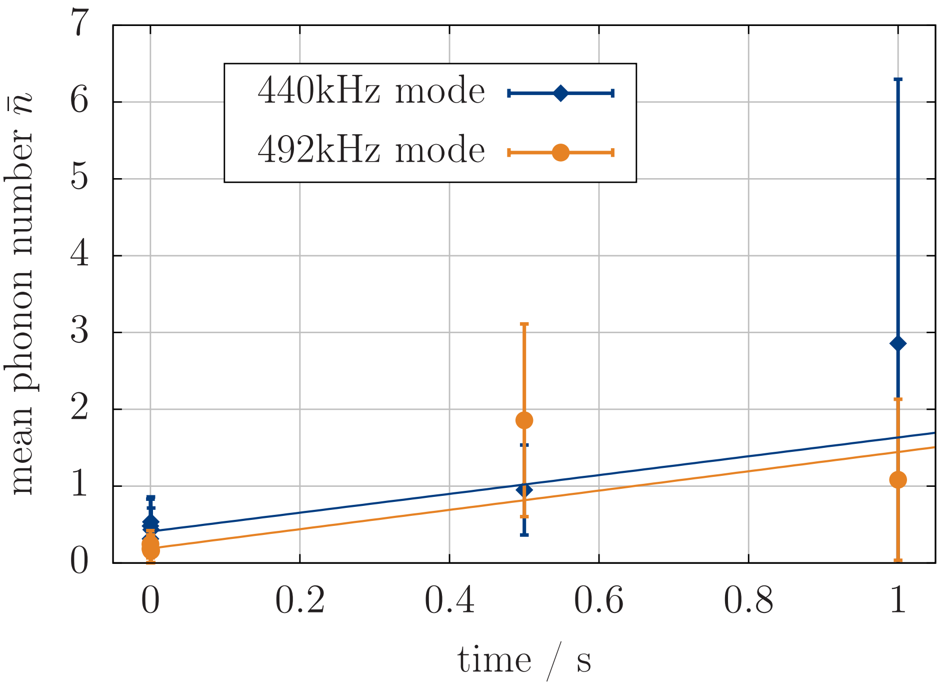

Figure 5.13.: Measurement of the heating rates in both radial modes. A single ion is cooled close to the ground state. After a variable waiting period, its temperature is determined by a comparison of first-order red and blue sideband excitations.

ω_{sec}	$\dot{\bar{n}}$	$S_E(\omega_{\text{sec}})$
$2\pi \times 440\,\text{kHz}$	$1.2(4)\,\text{s}^{-1}$	$1.6(5) \times 10^{-14}\ (\text{V/m})^2/\text{Hz}$
$2\pi \times 492\,\text{kHz}$	$1.3(5)\,\text{s}^{-1}$	$1.9(7) \times 10^{-14}\ (\text{V/m})^2/\text{Hz}$

Table 5.1.: Heating rates measured for the radial modes and derived electric field noise PSDs.

shift due to each mode as

$$\frac{\partial}{\partial t}\left(\frac{\Delta\nu_{\mathrm{D2}}}{\nu}\right) = -\frac{\dot{\bar{n}}\hbar\omega_{\mathrm{sec}}}{mc^2}\,, \tag{5.4}$$

which evaluates to $-2.5(10) \times 10^{-20}\,\mathrm{s}^{-1}$ for an indium ion using the value obtained for the 492 kHz mode. The frequency shift during the optimal interrogation period of 200 ms would therefore be completely negligible. The trap would even be suitable for interrogation times on the order of several seconds, as would be possible with narrower clock transitions.

6. Micromotion determination for frequency uncertainties below 10^{-19}

Micromotion is an essential consequence of the rf confinement in a Paul trap that can give rise to considerable frequency uncertainties if not properly treated. With overall systematic uncertainties in trapped-ion frequency standards approaching the low 10^{-18} region, time dilation due to micromotion is currently among the dominating contributions [15, 36]. This section describes methods for the determination of micromotion amplitudes at a level corresponding to fractional frequency uncertainties $< 10^{-19}$. Three commonly used techniques are compared in terms of their uncertainty and applicability during clock operation. A new model is developed for photon-correlation signals, which is necessary for a quantitative evaluation under commonly encountered experimental conditions. It is verified by comparison with resolved sideband measurements. When performed close to Doppler temperature, sideband measurements show a previously undescribed temperature-dependent offset, for which an expression is derived. This contribution becomes relevant at the level of a few 10^{-19} for the used experimental parameters. By comparison with photon-correlation measurements, it is shown that the easy to implement parametric excitation method allows micromotion compensation at a level $< 10^{-19}$ as well. The main results presented in this chapter have been published in J. Appl. Phys. [132].

6.1. Quantification and compensation of excess micromotion

Two of the investigated techniques allow a quantitative measurement of the micromotion amplitude. Both are based on the 1st-order Doppler shift due to micromotion, which can be described as a sinusoidal modulation of the laser phase in the reference frame of the ion. Its amplitude is referred to as the modulation index $\beta = \vec{k}\vec{x}_0 = \vec{k}\vec{v}_0/\Omega_{\mathrm{rf}}$, where $\vec{x}_0$, $\vec{v}_0$ are the micromotion peak amplitude and velocity. Under typical conditions, $\beta \ll 1$, and the spectrum of a monochromatic laser at ω_L, as experienced by the ion, can be approximated by

$$\begin{aligned} E(\omega) \propto\; & J_0(\beta)\delta(\omega-\omega_L) \\ & + J_1(\beta)\left(\delta(\omega-\omega_L-\Omega_{\mathrm{rf}}) - \delta(\omega-\omega_L+\Omega_{\mathrm{rf}})\right) \ . \end{aligned} \tag{6.1}$$

As a direct measure of the micromotion amplitude, β is related to the residual rf electric field $\vec{E}_{\mathrm{rf}}$ experienced by the ion via

$$E_{\mathrm{rf}} = \frac{m\Omega_{\mathrm{rf}}^2}{ke}\beta \, , \tag{6.2}$$

where E_{rf} is the projection of $\vec{E}_{\mathrm{rf}}$ onto $\vec{k}$. The second order Doppler shift due to thermal motion and EMM is (see section 2.3.1)

$$\left\langle \frac{\Delta\nu_{\mathrm{2D}}}{\nu} \right\rangle = -\frac{5k_BT}{2mc^2} - \left(\frac{e}{2mc\Omega_{\mathrm{rf}}}E_{\mathrm{rf}}\right)^2 = -\frac{5k_BT}{2mc^2} - \left(\frac{\Omega_{\mathrm{rf}}}{2ck}\beta\right)^2 \, . \tag{6.3}$$

Its independence from both the mass and transition wavelength makes it a useful way to quantify EMM in the context of spectroscopy.

In addition, micromotion gives rise to a 2nd-order Stark shift due to the non-vanishing mean-squared electric field E [1]

$$\left\langle \frac{\Delta\nu_{\mathrm{S}}}{\nu} \right\rangle = \sigma_{\mathrm{S}} \left\langle E^2 \right\rangle = \sigma_{\mathrm{S}} \left(\frac{1}{2}E_{\mathrm{rf}}^2 + \frac{m\Omega_{\mathrm{rf}}^2}{e^2}k_BT \right) \, , \tag{6.4}$$

the sign and magnitude of which depend on the differential static polarizability σ_{S} of the involved states [32]. For clock transitions in which the Stark effect increases the frequency, the proper choice of trap drive frequency allows a cancellation of both contributions [14]. In species with a low differential static polarizability of the clock states, such as In^+ and Al^+ [29], the Stark shift due to a given rf electric field amplitude is typically more than an order of magnitude below the corresponding 2nd-order Doppler shift.

The possible causes for EMM in the directions of rf confinement are phase shifts between the rf electrodes and stray electric fields, which displace the potential minimum from the rf node [32]. Phase shifts are eliminated by ensuring equal effective lengths of the rf feeds, while external fields are compensated in the experiment by two voltages, denoted U_{tc} and U_{ec}, which are applied to the trap electrodes as indicated in Fig. 6.1.

There are various experimental techniques for the detection of micromotion [134–141]. The following sections introduce the three which have been investigated in the scope of this work in terms of their resolution and applicability in a (multi-ion) optical clock.

---

[1] When derived within the adiabatic approximation, the right-hand side of Eq. 6.4 contains an additional term $\sigma_S E_{\mathrm{dc}}^2$. The exact solution, however, shows that the equilibrium position is where E_{dc} is canceled by the time-averaged contribution from the inhomogeneity of the rf electric field, which the approximation neglects [133, supp. material].

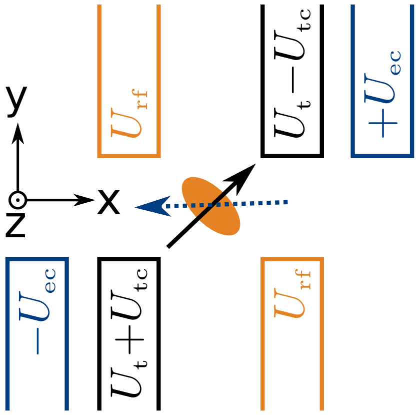

Figure 6.1.: Radial cut through a trap segment showing the different voltages applied to the electrodes. The compensation voltages U_tc and U_ec are used to cancel static electric stray fields for excess micromotion compensation.

6.2. The resolved-sideband method

The resolved sideband method makes use of a transition with a linewidth of $\Gamma \ll \Omega_\mathrm{rf}$. In this case, the micromotion component parallel to $\vec{k}$ can be determined from a measurement of the relative strengths of carrier and sideband transitions in (6.1):

$$\frac{\Omega_{\pm 1}}{\Omega_0} = \frac{J_1(\beta)}{J_0(\beta)} \approx \frac{\beta}{2} \, , \tag{6.5}$$

where Ω_0 and $\Omega_{\pm 1}$ denote the Rabi frequency of the carrier transition and 1st-order micromotion sideband, respectively.

Depending on Γ and the available laser power, the Rabi frequencies can be determined either from coherent population evolution or from steady-state excitation rates. In the latter case, decoherence must be well understood, e.g. solely due to excited state decay, in order to quantitatively determine $\Omega_{0,\pm 1}$. Sufficiently broad transitions allow a direct detection of the steady-state fluorescence [142].

Experimental realization

The experimental realization of the sideband method is straightforward. After the micromotion sideband frequency is determined by a frequency scan, Rabi oscillations are observed first on the sideband and then on the carrier transition. The measurements are performed in that order since the correct detuning is more critical on the sideband transition, due to the lower Rabi frequency. For a detailed description of the spectroscopy sequence, see Ch. 5. In order to reduce the time consumption, measurements are performed without sideband cooling. The temperature and $\Omega_0^{(\mathrm{int})}$ are extracted from a fit to the carrier Rabi oscillations. In the fit to the sideband signal, the temperature is fixed at the determined value.

6.2.1. IMM sampling in measurements at Doppler temperature

In the limit of an infinitely narrow ion wavepacket, the micromotion sideband vanishes entirely when there is no EMM component parallel to $\vec{k}$, as expected from the above derivation. This is not necessarily true for Doppler cooled ions, for which a temperature-dependent offset can appear, even in the Lamb-Dicke regime. This section explains the origin of the signal, which is on the order of $|\Delta\nu_{\mathrm{2D}}/\nu| = 10^{-19}$ for a Doppler-cooled $^{172}\mathrm{Yb}^+$ ion in a trap with $\omega_{\mathrm{sec}} = 2\pi \times 500\,\mathrm{kHz}$.

Classical considerations

According to Eq. 2.9, in the absence of EMM, the ion motion contains only Fourier components at ω_i and $\Omega_{\mathrm{rf}} \pm \omega_i$. However, the phase modulation of the laser electric field is described by the factor $\exp(i\vec{k}\vec{u}(t))$, the nonlinearity of which gives rise to a frequency component at Ω_{rf} in the absorption spectrum. This can be shown by expanding the resulting phase modulation at all three frequencies in terms of Bessel functions:

$$\begin{aligned}
&\exp\left(iku_i(t)\right) = \exp\left(iku_{1,i}\left(\cos(\omega_i t) + \frac{q_i}{4}\cos((\Omega_{\mathrm{rf}}+\omega_i)t) + \frac{q_i}{4}\cos((\Omega_{\mathrm{rf}}-\omega_i)t)\right)\right)\\
&= \left(\sum_{m_1=0}^{\infty} i^{m_1} J_{m_1}\left(ku_{1,i}\right) e^{im_1\omega_i t}\right)\\
&\times \left(\sum_{m_2=0}^{\infty} i^{m_2} J_{m_2}\left(ku_{1,i}\frac{q_i}{4}\right) e^{im_2(\Omega_{\mathrm{rf}}+\omega_i)t}\right)\left(\sum_{m_3=0}^{\infty} i^{m_3} J_{m_3}\left(ku_{1,i}\frac{q_i}{4}\right) e^{im_3(\Omega_{\mathrm{rf}}-\omega_i)t}\right) ,
\end{aligned} \tag{6.6}$$

where k is the projection of $\vec{k}$ onto u_i. After carrying out the multiplication, there are various terms oscillating at $\mp\Omega_{\mathrm{rf}}$ that lead to an excitation by a laser detuned by $\pm\Omega_{\mathrm{rf}}$. The two dominating terms at each frequency have an amplitude of

$$-J_1\left(ku_{1,i}\right) J_1\left(ku_{1,i}\frac{q_i}{4}\right) J_0\left(ku_{1,i}\frac{q_i}{4}\right) = -(ku_{1,i})^2\frac{q}{16} + \mathcal{O}\left((ku_{1,i})^4\right) \tag{6.7}$$

and interfere constructively. The scaling with $u_{1,i}^2$ leads to a linear temperature dependence of the signal. Adding EMM to this derivation results in an imaginary amplitude that scales with $iJ_1(ku_{0,i}q_i/2)$, which means that the two contributions add up quadratically:

$$|\Omega_1| = \sqrt{|\Omega_{1,\mathrm{IMM}}|^2 + |\Omega_{1,\mathrm{EMM}}|^2} \, . \tag{6.8}$$

This is important, as otherwise the two components could interfere and the signal minimum would not coincide with minimized EMM.

Figure 6.2 illustrates a more intuitive approach: As the ion undergoes secular oscillations across the rf node, the IMM phase changes by π, leading to a different sign for contributions

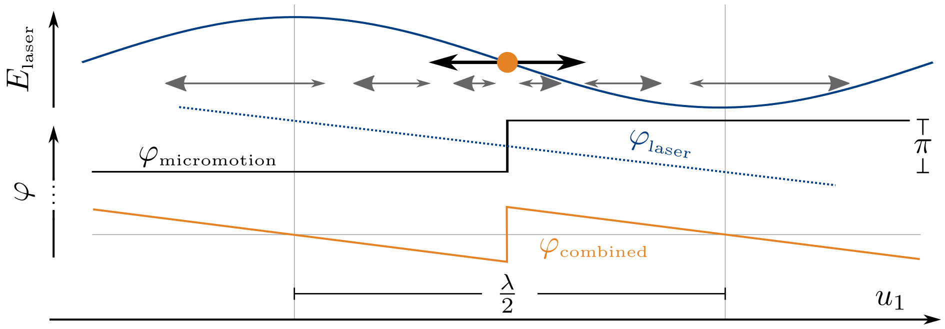

Figure 6.2.: Intuitive explanation for the IMM contribution in resolved sideband measurements. Top: ion undergoing secular motion along the $\tilde{k}$ vector of the probing laser. The induced micromotion is assumed to be parallel to the secular motion (thin arrows). Center: while the laser phase changes linearly with position, the phase of the micromotion jumps by π as the rf node is crossed. Bottom: if the amplitude of the secular motion becomes comparable to $\lambda/2$, contributions from either side of the rf node no longer cancel entirely.

from either half period. However, if it is not deep within the Lamb-Dicke regime, the ion samples a considerable range of laser phases during its secular motion. The reduced phase shift between IMM contributions weakens the cancellation, and excitation on the sideband can be observed.

Since the signal is caused by correlated micromotion and secular motion components along $\vec{k}$, its amplitude is maximized in the one-dimensional geometry assumed so far. In typical setups, optical access is such that $\vec{k}$ is more likely to be aligned almost perpendicular to the quadrupole field lines, as depicted in Fig. 6.3. In that geometry, displacements along $\vec{k}$ induce micromotion in the perpendicular direction. The relative amplitude of the signal at Doppler temperature can then be calculated from the temporal average of the product of secular motion and micromotion in the classical radial trajectory of the ion, each projected onto $\vec{k}$:

$$\begin{aligned} |\Omega_{\pm 1}| &\propto \left\langle \left(\vec{k}\vec{E}_{\text{rf}}(\vec{r})\right)\left(\vec{k}\vec{r}\right)\right\rangle_t \\ &\propto \left[\cos(\theta_{\text{rf}})\sin(2\theta_{\text{dc}})(r_2^2 - r_1^2) + \sin(\theta_{\text{rf}})\left(r_1^2(1+\cos(2\theta_{\text{dc}})) + r_2^2(1-\cos(2\theta_{\text{dc}}))\right)\right] \ , \end{aligned} \tag{6.9}$$

where indices 1 and 2 denote the radial modes, the pulse duration t is assumed to be long compared to $1/|\omega_1 - \omega_2|$, and $r_i = \sqrt{k_B T/(m\omega_i^2)}$ is the classical thermal amplitude of secular oscillations.

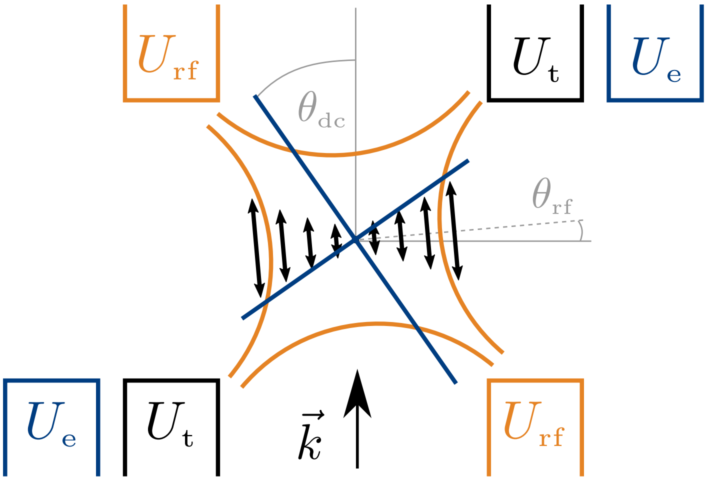

Figure 6.3.: Illustration of the sampled IMM in resolved sideband measurements for a typical geometry (not to scale). The signal depends on the amount of correlation between secular motion and micromotion (black arrows) in the radial trajectories of the ion when projected onto $\tilde{k}$, averaged over the duration of the pulse.

Quantum-mechanical derivation

While intuitive, the classical derivation is only valid for thermal states of sufficient temperature. In the following, the signal is therefore derived quantum-mechanically for a Fock state. For simplicity, again only motion in one dimension is considered, assuming that the secular motion, the resulting micromotion, and the $\vec{k}$ vector are parallel. Furthermore, the pulsation of the harmonic oscillator wavefunctions at Ω_{rf} [62] is neglected.

In the adiabatic approximation of Eq. 2.9, micromotion can be described as a position-dependent phase modulation with amplitude $k(\hat{x}+x_e)q/2$, where $\hat{x} = x_0(\hat{a}+\hat{a}^\dagger)$ is the position operator, and the origin is defined by the potential minimum, which is displaced from the rf node by x_e. A laser field detuned by Ω_{rf} appears in the moving frame of reference as

$$\vec{E}(t) = \vec{E}_0 \times e^{i(\omega_0+\Omega_{\mathrm{rf}})t} \times e^{ik\hat{x}} \times e^{i\frac{1}{2}k(\hat{x}+x_e)q\cos(\Omega_{\mathrm{rf}}t)} \,. \tag{6.10}$$

Expanding the rightmost exponential as a series of sidebands weighted with the respective Bessel functions yields

$$\vec{E}(t) = \vec{E}_0 \times e^{i(\omega_0+\Omega_{\mathrm{rf}})t} \times e^{ik\hat{x}} \times \left(\sum_{n=-\infty}^{\infty} i^n J_n\left(\frac{k(\hat{x}+x_e)q}{2}\right) e^{in\Omega_{\mathrm{rf}}t} \right) \,. \tag{6.11}$$

Neglecting all terms detuned by $\geq \Omega_{\mathrm{rf}}$ reduces the expression to

$$\vec{E}(t) = \vec{E}_0 \times e^{i\omega_0 t} \times e^{ik\hat{x}} \times (-i)J_{-1}\left(\frac{k(\hat{x}+x_e)q}{2}\right) \,. \tag{6.12}$$

The transition matrix element between internal states $|g\rangle$ and $|e\rangle$ in the motional state $|n\rangle$ is

$$\left\langle e,n \middle| \vec{d}\cdot\vec{E}(t) \middle| g,n \right\rangle = \frac{\hbar\Omega_0^{(\mathrm{int})}}{2} \left\langle n \middle| e^{ik\hat{x}} \times (-i)J_{-1}\left(\frac{k(\hat{x}+x_e)q}{2}\right) \middle| n \right\rangle \,, \tag{6.13}$$

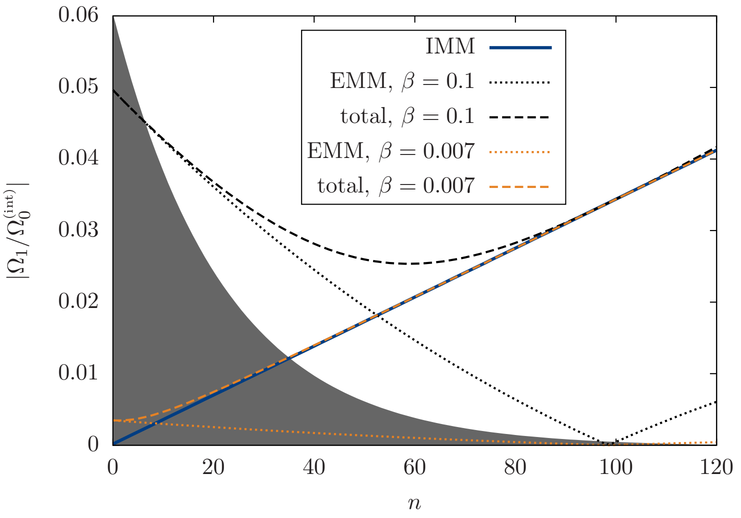

Figure 6.4.: Influence of the IMM sideband on EMM measurements at $\omega = 2\pi \times 470\,\mathrm{kHz}$. The shaded area shows the thermal occupation of states at the $^{172}\mathrm{Yb}^+$ Doppler limit of 0.5 mK. Experimentally observed signals are ensemble averages of Rabi oscillations, weighted with this distribution.

where $\vec{d}$ denotes the transition dipole element and $\Omega_0^{(\mathrm{int})}$ the Rabi frequency of the free ion. Expanding the Bessel function and neglecting terms of order q^3 simplifies the overlap integral of the motional wavefunction to

$$\left\langle n \left| e^{ik\hat{x}} \times (-i) J_{-1}\left(\frac{k(\hat{x}+x_e)q}{2}\right) \right| n \right\rangle \approx \left\langle n \left| e^{ik\hat{x}} \times (-i) \frac{k\hat{x}q}{4} \right| n \right\rangle - i\frac{kx_e q}{4} \left\langle n \left| e^{ik\hat{x}} \right| n \right\rangle . \tag{6.14}$$

Since all terms with odd powers of $\hat{x}$ vanish for parity reasons, the expression evaluates to

$$\frac{\Omega_1}{\Omega_0^{(\mathrm{int})}} = \underbrace{\frac{q}{4}\eta^2 (2n+1) + \mathcal{O}\left(\eta^4\right)}_{\mathrm{IMM}} \underbrace{- i\mu_{n,n}\left(\frac{\beta}{2} + \mathcal{O}\left(q^3\right)\right)}_{\mathrm{EMM}} , \tag{6.15}$$

with the Lamb-Dicke parameter $\eta = kx_0$, EMM modulation index $\beta = kx_e q/2$, and motional overlap factor $\mu_{n,n'} = \langle n' | e^{ik\hat{x}} | n\rangle$. Note again the $\pi/2$ phase shift between the components, which prevents interference.

Figure 6.4 illustrates the influence of the IMM sideband on EMM measurements at the $^{172}\mathrm{Yb}^+$ Doppler limit of 0.5 mK for a secular frequency of 470 kHz. Signals measured in experiments are ensemble averages of Rabi oscillations, weighted with the thermal occupation of states. When EMM is suppressed to the technical limit of $\beta = 0.007$, as explained below in section 6.5.1, IMM strongly dominates the signal.

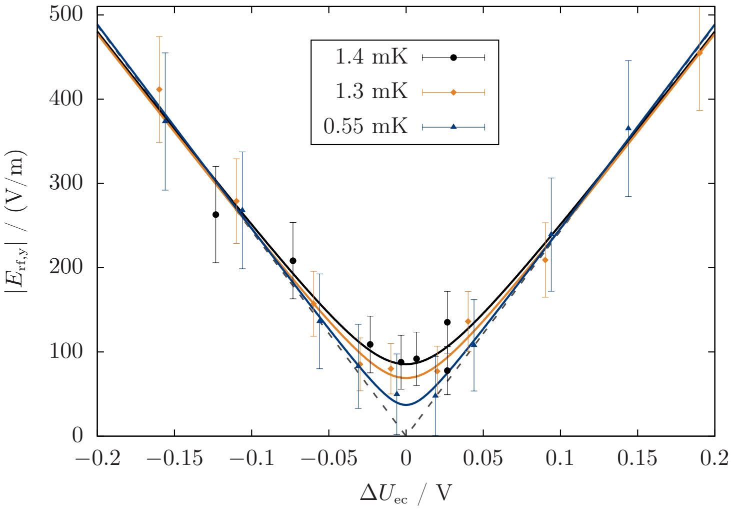

Figure 6.5.: Experimental observation of the IMM influence in resolved sideband measurements at varied temperature.

Experimental observation of the IMM signal

Since the amount of sampled IMM in the experiments depends on various unknown geometrical parameters, it would need to be included as a free parameter in the fits. This would require fitting all sideband data simultaneously, which would result in a tremendous increase in computational effort. Moreover, at the Doppler limit, the sideband Rabi frequencies caused by IMM are close to the resolution limit due to magnetic field induced decoherence and negligible compared to the EMM contribution in most of the measurements. For these reasons, IMM is not included in the model for data evaluation and appears as an error in measurements with low EMM.

Figure 6.5 shows three scans of the compensation voltage U_{ec} at different temperatures. The influence of IMM is visible around the EMM minimum as an $|E_{\mathrm{rf}}|$ offset that scales linearly with temperature, as expected from the derivations above. With groundstate cooled ions, no sideband excitation is observed once EMM is minimized. In order to estimate the geometrical factor between the experimental (2D) case and the amplitude derived above for the (1D) worst case, the evaluation is run on artificial data calculated according to Eq. 6.15 with $\beta = 0$ at Doppler temperature. The resulting offset of $\beta = 0.1$ shows that the experimentally observed value is about 1/8 of the worst case.

While the minimum occurs at the correct compensation voltage to cancel stray fields, the offset could be mistaken for EMM caused by an rf phase shift. Since the observed offsets resemble EMM corresponding to $|\Delta\nu_{\mathrm{2D}}/\nu| \approx 1 \times 10^{-19}$ (0.55 mK) … 6×10^{-19} (1.4 mK) for $^{115}\mathrm{In}^+$, the effect cannot be neglected when targeting frequency uncertainties of 10^{-18} and below.

6.3. The photon-correlation method

The photon-correlation method determines the modulation index β using a transition that violates the resolved sideband condition $\Gamma \ll \Omega_{\mathrm{rf}}$. It has been described in detail by Berkeland et al. [32] for the case when $\Gamma \gg \Omega_{\mathrm{rf}}$, i.e. assuming that the scattering rate is in steady state at every instance of the rf cycle. However, with an rf drive frequency of 25 MHz, this assumption cannot be made for the $^2\mathrm{S}_{1/2} \leftrightarrow {}^2\mathrm{P}_{1/2}$ transition in $^{172}\mathrm{Yb}^+$, where $\Gamma = 2\pi \times 19.6\,\mathrm{MHz}$. This is in fact the case for a lot of typical Paul trap setups and ion species. In this section, the signals obtained by the photon-correlation method are therefore derived in a way that is valid in the regime $\Gamma \approx \Omega_{\mathrm{rf}}$.

6.3.1. Principle

The method makes use of the fact that as a driven motion, micromotion has a fixed phase relation to the trap rf voltage. This results in a correlation between the trap drive and the fluorescence modulation due to the 1st-order Doppler shift from EMM [143, 144], which is observed by recording the time delay between each detected photon and the succeeding rf zero crossing. A histogram of the observed delays resembles the time-inverted distribution of photons within one rf period. It has the form

$$S(t) = S_0 + \Delta S \cos(\Omega_{\mathrm{rf}} t - \varphi) \,, \tag{6.16}$$

where S_0 is proportional to the mean fluorescence, the observation time and the bin size, and the normalized modulation amplitude $\Delta S/S_0$ and the phase φ are used to determine the amplitude and phase of the EMM.

Analytic model

In the limit of low intensity $I \ll I_{\mathrm{sat}}$, the atomic transition can be described as a classical damped harmonic oscillator with resonance (angular) frequency ω_0 and damping rate Γ. Its frequency response to an excitation at frequency ω is (see, e.g. [89])

$$A(\omega - \omega_0) = \frac{1}{2} \frac{\frac{\Gamma}{2} - i(\omega - \omega_0)}{(\omega - \omega_0)^2 + (\frac{\Gamma}{2})^2} \,, \tag{6.17}$$

as shown in Fig. 6.6. The detected fluorescence is proportional to the power in this oscillator when excited with the spectrum (6.1), which in the time domain consists of three

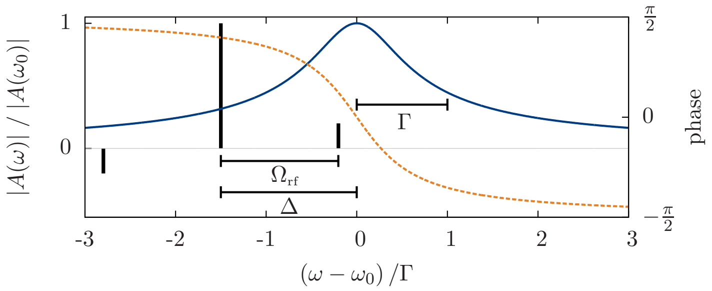

Figure 6.6.: Illustration of the model used to derive the photon-correlation signal. The atomic transition is described as a classical damped oscillator (see Eq. 6.17), the spectral response of which is shown by the solid (amplitude) and dashed (phase) lines. In its frame of reference, micromotion causes an apparent phase modulation of the laser, which produces sidebands (vertical bars, see Eq. 6.1). The quantities Γ,Ω_{rf} and Δ are indicated in units of Γ.

contributions:

$$\begin{aligned} S(\Delta, t) &= \left| \int_{-\infty}^{\infty} A(\omega - \omega_0) E(\omega) e^{i\omega t} d\omega \right|^2 \\ &\propto \underbrace{J_0^2(\beta)|A(\Delta)|^2 + J_1^2(\beta)\left(|A(\Delta + \Omega_{\text{rf}})|^2 + |A(\Delta - \Omega_{\text{rf}})|^2\right)}_{S_0, \text{“dc component”}} \\ &+ \underbrace{2J_0(\beta)J_1(\beta)\left|A^*(\Delta)A(\Delta + \Omega_{\text{rf}}) - A(\Delta)A^*(\Delta - \Omega_{\text{rf}})\right|}_{\Delta S, \text{“rf component”}} \cos\left(\Omega_{\text{rf}} t + \varphi\right) \\ &+ 2J_1^2(\beta)|A(\Delta + \Omega_{\text{rf}})A^*(\Delta - \Omega_{\text{rf}})| \cos(2\Omega_{\text{rf}} t + \varphi') \end{aligned} \tag{6.18}$$

with phase

$$\varphi = \arg\left(A^*(\Delta)A(\Delta + \Omega_{\text{rf}}) - A(\Delta)A^*(\Delta - \Omega_{\text{rf}})\right) . \tag{6.19}$$

Here, $\Delta = \omega_L - \omega_0$ is the detuning of the laser (carrier) frequency from the atomic resonance.

The first two terms in (6.18) correspond to the offset S_0 and amplitude ΔS of the observed signal (6.16), whereas the term that oscillates at $2\Omega_{\text{rf}}$ is of order $J_1^2(\beta)$ and can be neglected for $\beta \ll 1$. This result reflects that the process is analogous to performing frequency-modulation spectroscopy on the atomic transition [145].

Equation 6.18 shows that for $\beta \ll 1$, the quantity $\Delta S/S_0 \propto J_1(\beta)/J_0(\beta)$ is a direct measure of the excess micromotion amplitude. The proportionality factor depends on the well-known parameters Γ and Ω_{rf}, as well as the laser detuning Δ, as shown in Fig. 6.7. While this

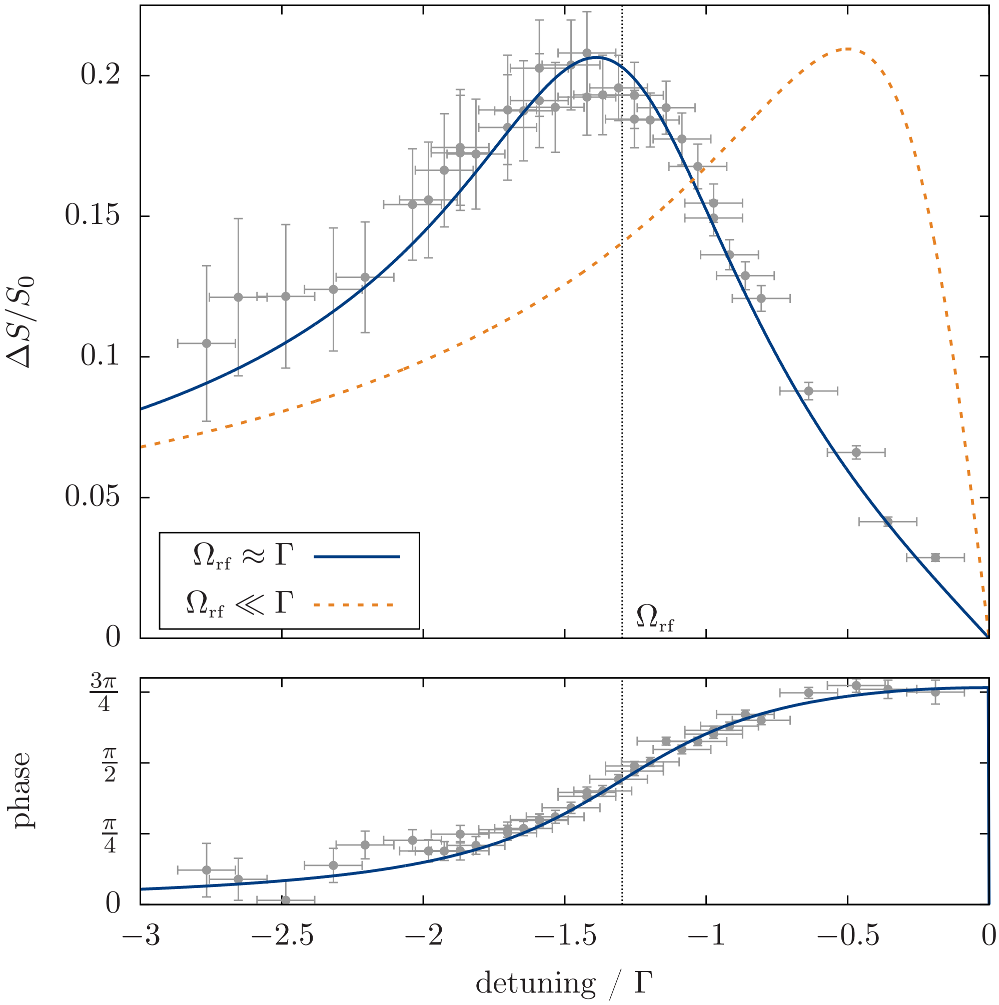

Figure 6.7.: Photon-correlation signal for a fixed micromotion amplitude ($\beta = 0.085$) and varied laser detuning in the limit $I \ll I_{\rm sat}$. The solid curve is calculated using the experimental parameters ($\Gamma = 2\pi \times 19.6\,\mathrm{MHz}$ and $\Omega_{\rm rf} = 2\pi \times 25.42\,\mathrm{MHz}$). Experimental values confirm the expected behavior (see section 6.3.2). The dashed curve shows the result of the model derived by Berkeland et al. [32] for the same micromotion velocity v_0. The two models agree in the limit $\Omega_{\rm rf} \ll \Gamma$. In that limit, the phase becomes constant.

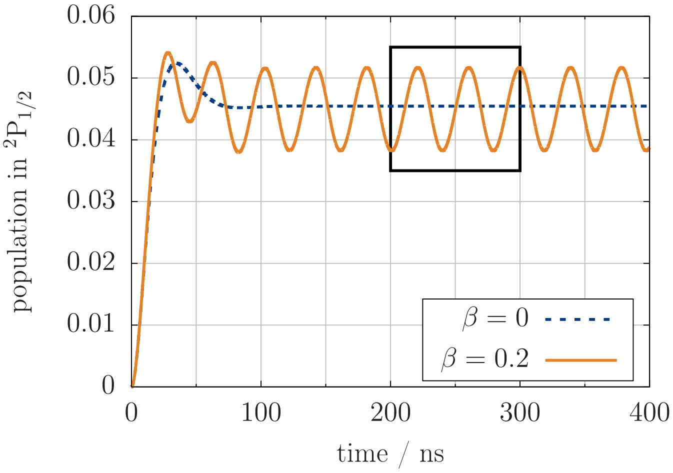

Figure 6.8.: Influence of micromotion on the evolution of the excited state population. The signal within the black box is used to derive $\Delta S/S_0$ and the relative phase.

model agrees with the one derived by Berkeland et al. [32] in the limit $\Omega_{\mathrm{rf}} \ll \Gamma$, there is a significant deviation when the frequency scales become comparable. This is due to the fact that the phase difference in the atomic response to carrier and sidebands cannot be neglected, and a first order approximation of the line shape over a range of $2\Omega_{\mathrm{rf}}$ fails in this regime (cf. Fig. 6.6). It is also apparent that the highest sensitivity is no longer attained at a detuning of $-\Gamma/2$, but rather close to $-\Omega_{\mathrm{rf}}$. Note that the clear maximum at a known detuning provides a simple way to experimentally determine the resonance frequency, which cannot be measured directly on a cooling transition [146].

The phase information obtained with the signal is a major advantage of the photon-correlation method: the separation of in-phase and out-of-phase components in measurements with two nonparallel beams allows a full determination of the amplitude and orientation of the micromotion within the common plane. The phase information also allows a distinction between excess micromotion due to a displacement and due to an rf phase shift, since the phase of the former changes by π when the ion is moved across the rf node.

Numerical corrections

While the above treatment has the advantage of providing an analytic expression, the classical approach cannot take saturation into account. Experimentally, it is not desirable to measure at low intensities, since longer integration times are necessary to obtain a given signal to noise ratio. In order to include saturation effects, the fluorescence signal is derived from the steady-state population of the $^2\mathrm{P}_{1/2}$ level in the numerical solution to the master equation of the system. For this purpose, only the $^2\mathrm{S}_{1/2}$ and $^2\mathrm{P}_{1/2}$ states are taken into account and micromotion is modeled as a time-dependent detuning. The interaction picture Hamiltonian is therefore

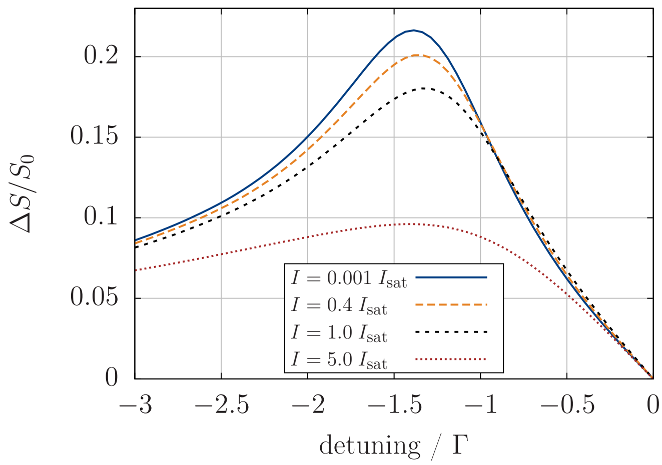

Figure 6.9.: Numerically calculated photon-correlation signal amplitudes as a function of laser detuning when taking saturation into account. The assumed micromotion amplitude corresponds to $\beta = 0.085$.

$$H(t) = \hbar \begin{pmatrix} 0 & \frac{\Omega}{2} \\ \frac{\Omega}{2} & \Delta \end{pmatrix} + \hbar \begin{pmatrix} 0 & 0 \\ 0 & \Delta_{\text{mm}} \end{pmatrix} \cos(\Omega_{\text{rf}} t + \varphi) \quad \text{with} \quad \Delta_{\text{mm}} = \vec{k}\vec{v}_{\text{mm}} \;, \tag{6.20}$$

where $\Omega = \Gamma\sqrt{I/(2I_{\text{sat}})}$ is the Rabi frequency. Figure 6.8 shows the resulting excited state population (numerically calculated [147], including decay) as a function of time, assuming that the interaction is switched on at $t = 0$. To avoid the influence of the transient, the range marked by the black box is used for the evaluation. A fit to this data directly extracts $\Delta S/S_0$ and the relative phase.

The result is shown in Fig. 6.9 as a function of detuning for different intensities and a fixed amount of EMM. For low intensities, it matches the analytic expression (6.18). The most important consequence of saturation is a reduction of the signal, which requires a correction and introduces an uncertainty in the evaluation of experimental data.

The signal is further affected by additional line broadening processes. Most of these contributions, such as the laser linewidth and the thermal 1st-order Doppler broadening, can be summed up into an overall Gaussian broadening. The Zeeman shift is an exception, as it consists of a small number of discrete lines. All of these influences can be included as an ensemble average of the numerical solution over the respective spectral distribution. Their effect is both a reduction of the maximum sensitivity and a shift of the laser detuning at which it occurs. Figure 6.10 shows the numerically calculated magnitude of both these influences. In the case of Gaussian broadening, "width" denotes the standard deviation, whereas for the Zeeman effect, two components, shifted with opposite sign by the indicated amount, have been assumed.

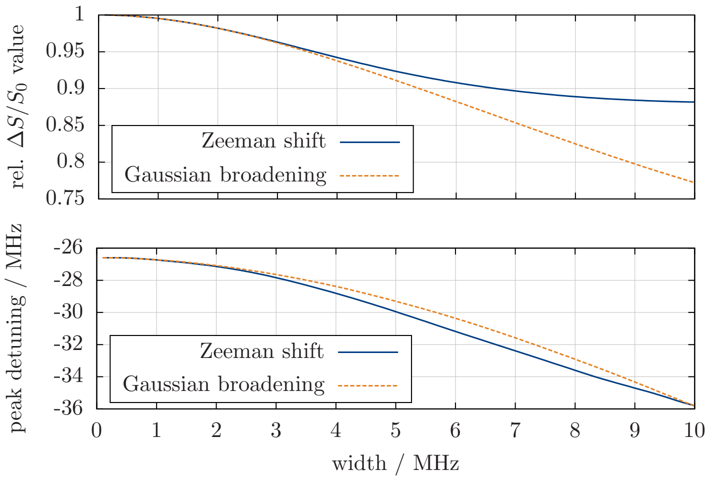

Figure 6.10.: Influence of line broadening and the Zeeman effect on the photon-correlation signal. The top plot shows the reduction of the signal amplitude with increasing width. The detuning at which the signal amplitude is maximized shifts with increasing broadening, as shown by the lower plot. "Width" refers to half the relative shift between two assumed Zeeman components and the standard deviation of a Gaussian frequency distribution, respectively.

6.3.2. Experimental realization

Figure 6.11 illustrates the experimental scheme. Three laser beams are necessary for the full determination of the micromotion amplitude and direction. The two horizontal beams, H1 and H2, are used for measurements within the x-z plane. They are oriented at an angle of $\theta_z = 25\,^\circ$ with respect to the z axis. The vertical component of micromotion is determined with the beam V, which is oriented along the y direction. Since it is orthogonal to the trap axis, a strongly attenuated H1 beam is applied simultaneously in these measurements to prevent axial heating. The power is actively stabilized using an AOM. As a compromise between the count rate and micromotion sensitivity, the intensity is set to $I = 0.4 \times I_{\mathrm{sat}}$.

The fluorescence is imaged onto a PMT, and a discriminator produces a TTL pulse for each detected photon. This pulse acts as the start trigger for a time-to-amplitude converter (TAC), which is stopped by the following zero crossing of U_{rf}. The output of the TAC is binned by a multi-channel analyzer (MCA) to produce the signal (6.16).

Data evaluation and uncertainty contributions

Parasitic coupling of U_{rf} to the PMT signal leads to an error in EMM determination. The effect of this component depends on its relative phase with respect to the actual EMM signal.

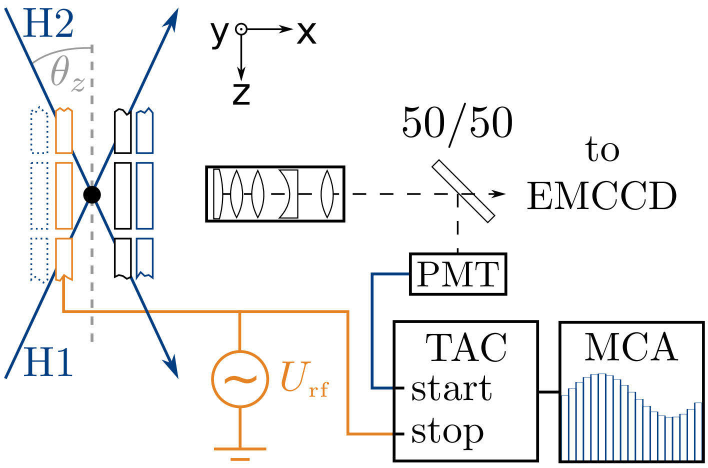

Figure 6.11.: Laser geometry and simplified detection setup used for photon-correlation measurements. Micromotion in the horizontal plane is detected using two beams denoted H1 and H2. The vertical component of micromotion is measured with a single vertical beam (V). Half of the collected fluorescence is imaged onto a photomultiplier tube for detection. A time-to-amplitude converter and multi-channel analyzer extract the photon-correlation signal.

Figure 6.12.: Illustration of the influence of an rf pickup signal on micromotion compensation. While the in-quadrature component only increases the minimum signal, the in-phase component shifts the position of the minimum and thereby introduces an error in the deduced optimal compensation voltage.

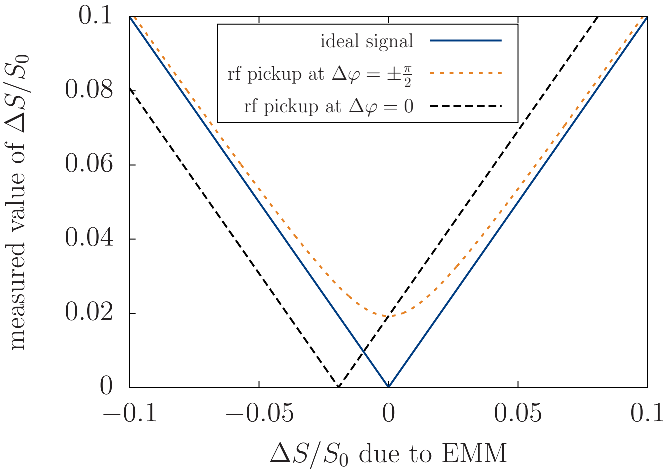

Figure 6.12 illustrates the extreme cases: While a pickup signal 90 ° out of phase with the micromotion is only visible when EMM is compensated, a signal at any other phase will lead to an error in determining the minimum, since the total signal is minimized when EMM compensates for the in-phase pickup component. Since the pickup signal remains constant unless any of the electronics are moved, a simple solution is to measure it using straylight and remove its influence from the raw data of the measurements. Omitting this correction would correspond to an $|E_{\mathrm{rf}}|$ error on the order of 20 V/m to 30 V/m. In addition, the amount of straylight from each beam needs to be measured and subtracted from the S_0 fit values.

After obtaining $\Delta S/S_0$, the results are converted to modulation indices using a 5th-order polynomial fit to the numerically calculated dependence. The relative error due to this approximation is less than 2×10^{-3} as long as $\Delta S/S_0 \leq 0.75$ (i.e. $\beta \leq 0.4$, $E_{\mathrm{rf}} \leq 1070\,\mathrm{V/m}$). Next, the E_{rf} components in the xyz coordinate system are calculated. In the y direction, the values only need to be rescaled: $E_{\mathrm{rf},y} = m\Omega_{\mathrm{rf}}^2 \beta_V/(ek)$. For the x and z components, a coordinate transformation is required:

$$\begin{aligned} E_{\mathrm{rf},x} &= \frac{m\Omega_{\mathrm{rf}}^2}{ek\cos(\theta_x)} \sqrt{\beta_{\mathrm{H1}}^2 + \beta_{\mathrm{H2}}^2 + 2\beta_{\mathrm{H1}}\beta_{\mathrm{H2}}\cos(\Delta\varphi)} \\ E_{\mathrm{rf},z} &= \frac{m\Omega_{\mathrm{rf}}^2}{ek\cos(\theta_z)} \sqrt{\beta_{\mathrm{H1}}^2 + \beta_{\mathrm{H2}}^2 - 2\beta_{\mathrm{H1}}\beta_{\mathrm{H2}}\cos(\Delta\varphi)}\ , \end{aligned} \tag{6.21}$$

where $\theta_x = 90\,° - \theta_z$ and $\Delta\varphi = \varphi_{\mathrm{H1}} - \varphi_{\mathrm{H2}}$. The $\Delta\varphi$ terms introduce an additional uncertainty for these components, which consists of a fit uncertainty and a contribution from the signal phase dependence on laser detuning (see Fig. 6.7).

Another uncertainty arises from the intensity dependence of the signal amplitude. From a linear approximation around $I = 0.4 \times I_{\mathrm{sat}}$,

$$\delta\left(\frac{\Delta S}{S_0}\right)_I \approx \frac{\Delta S}{S_0} \times (-0.175) \times \delta\left(\frac{I}{I_{\mathrm{sat}}}\right)\ . \tag{6.22}$$

As the laser power is actively stabilized, the biggest contribution to $\delta(I/I_{\mathrm{sat}})$ is the uncertainty in the saturation power. Its relative uncertainty of 25 % translates into a 1.8 % uncertainty in $\Delta S/S_0$.

Since measurements are performed at the maximum of sensitivity with respect to the laser detuning, its contribution to the overall uncertainty is a 2nd-order effect. A parabola fitted to the numerical data yields

$$\delta\left(\frac{\Delta S}{S_0}\right)_\nu \approx \frac{\Delta S}{S_0} \times (-4.4 \times 10^{-3})\,\mathrm{MHz}^{-2} \times \delta\nu^2\ . \tag{6.23}$$

As shown in section 3.2.3, the wavemeter instability is $\lesssim 1\,\mathrm{MHz}$, which leads to $\delta\nu = 2\,\mathrm{MHz}$ due to the subsequent SHG. The relative uncertainty in $\Delta S/S_0$ due to detuning is therefore

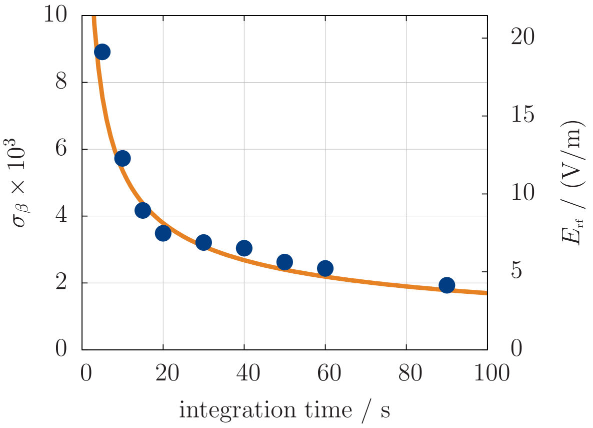

Figure 6.13.: Uncertainty of the photon-correlation method due to shot noise as a function of integration time. The fitted uncertainty is $1.7 \times 10^{-2}/\sqrt{t}$ for a count rate of 3600 cps. All other contributions to uncertainty are typically more than an order of magnitude lower.

1.8 %. Long-term drifts can be excluded since the absolute frequency is determined once a day with a scan over the maximum of $\Delta S/S_0$. Fluctuations of the laser frequency with respect to the wavemeter occur on timescales much shorter than the measurement and are therefore taken into account as an uncertainty of the Gaussian line broadening (see Fig. 6.10).

All of these contributions are relative and become negligible once micromotion is minimized. The dominating contribution to uncertainty then comes from the fit value of ΔS. In order to see the resolution limit, perfectly compensated micromotion is simulated by performing a series of correlation measurements with a straylight signal. Figure 6.13 shows the standard deviation of 50 measurements each as a function of the integration time. The good agreement with the fit function $\sigma_\beta(t) = \sigma_\beta(1\,\mathrm{s})/\sqrt{t}$ shows that the uncertainty is solely due to shot noise.

The continuous illumination during the measurement produces a net force that shifts the equilibrium position of the ion by

$$\Delta\vec{x} = \frac{\hbar\vec{k}\Gamma_{\rm sc}}{m\omega^2}\,, \tag{6.24}$$

where $\Gamma_{\rm sc}$ is the photon scattering rate, and ω quantifies the restoring force of the trapping potential in the direction of $\vec{k}$. For $\omega = 2\pi \times 440\,\mathrm{kHz}$, this amounts to $\Delta x = 2.2\,\mathrm{nm}$. The choice of $\vec{k}$ ensures that the micromotion induced by this displacement is perpendicular to $\vec{k}$ and therefore does not affect compensation.

6.3.3. Quantitative comparison to sideband measurements

In order to test the evaluation according to the new model, an interleaved measurement with the photon-correlation and sideband methods is performed. First, the horizontal displacement of the ion is minimized with photon-correlation measurements using the H1 and H2

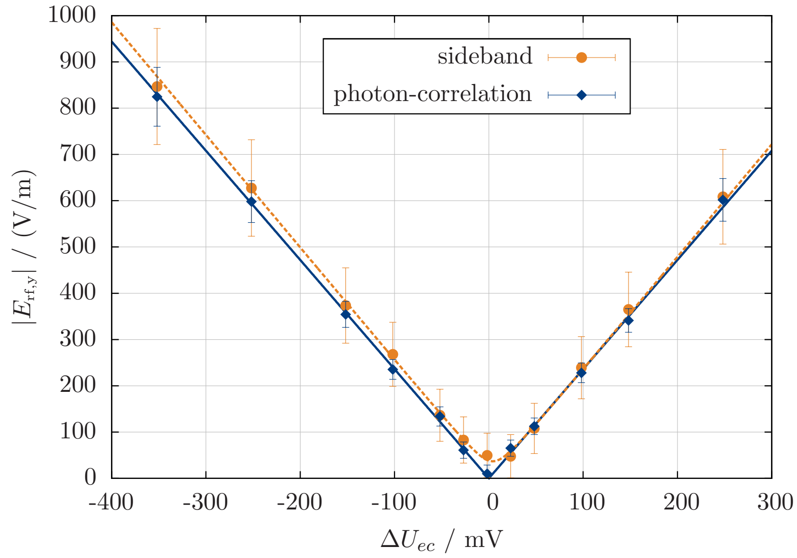

Figure 6.14.: Interleaved measurement using the photon-correlation and sideband methods (at 0.5 mK) as the ion is shifted radially through the trap center. The error bars of the photon correlation data are due to shot noise and the systematic uncertainties discussed in the text. The error bars of the sideband method assume 10 % fit uncertainty of the Rabi frequencies. The function fitted to the sideband data takes into account the offset due to IMM discussed in section 6.2.1.

beams and the compensation voltage U_{tc}, as shown in Fig. 6.1. The second compensation voltage, U_{ec} displaces the ion (to within 2 °) along the x direction, inducing EMM along y.

Figure 6.14 shows the measurement of this micromotion component using the vertical beams at 411 nm and 370 nm. The fitted slopes of E_{rf} with respect to U_{ec} are $s_{\mathrm{pc}} = (2360 \pm 30)\,(\mathrm{V/m})/\mathrm{V}$ and $s_{\mathrm{sb}} = (2437 \pm 29)\,(\mathrm{V/m})/\mathrm{V}$ for the photon-correlation and sideband method, respectively, showing a residual mismatch of less than 4 %. The optimum values of U_{ec} determined by the fits agree to within 4.2 mV, corresponding to a difference in E_{rf} of (10 ± 4) V/m. The 2nd-order Doppler shift for an $^{115}\mathrm{In}^{+}$ ion due to this mismatch would be below 10^{-20}.

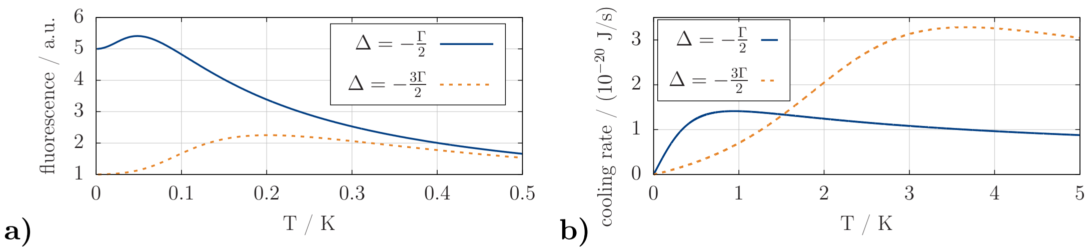

Figure 6.15.: Quantities to consider when choosing the laser cooling parameters in parametric excitation measurements: **a)** fluorescence and **b)** Doppler cooling rate as a function of temperature for two different laser detunings, at an intensity of $I = 0.1 \times I_{\text{sat}}$.

6.4. The parametric heating method

6.4.1. Principle

The parametric heating method does not measure micromotion directly, but detects a displacement $u_{0,i}$ from the minimum of the ponderomotive potential. When a modulation of the rf voltage is applied at $2/n \times \omega_{\text{sec}}$, with $n \in \mathbb{N}$, the secular motion is excited parametrically at a rate proportional to the displacement [138]. Unlike the other two methods, parametric excitation is not able to measure micromotion due to a phase shift between rf electrodes. Besides the simple experimental implementation, a major advantage of this method is that it uses the Doppler shift due to secular motion, rather than micromotion, to generate a signal. In principle, this allows three-dimensional micromotion compensation with a single laser beam, as long as it has projections onto all principal axes of the trap.

The signals observed for this method are changes in the amount of fluorescence as the modulation frequency is swept over the resonance. Both increases and decreases of the fluorescence have been observed, depending on the choice of parameters [138, 148, 149]. An increase in fluorescence typically occurs for low deviations from Doppler temperature, whereas fluorescence decreases when the temperature is increased further. In order to get a monotonic dependence of the signal with respect to EMM, it is therefore necessary to operate in the regime of fluorescence increase. The corresponding temperature range can be extended by detuning the cooling laser further from resonance, as shown in Fig. 6.15a, based on a Voigt profile. Since both the heating and Doppler cooling rates depend on temperature, experimental parameters must be chosen such that equilibrium is eventually reached, to avoid runaway heating. As the sensitivity of the method increases with equilibrium temperature, there is a trade-off between resolution and robustness, which can require several iterations while adjusting parameters as the minimum is approached.

The Doppler cooling rate can be estimated by integrating the energy loss due to the

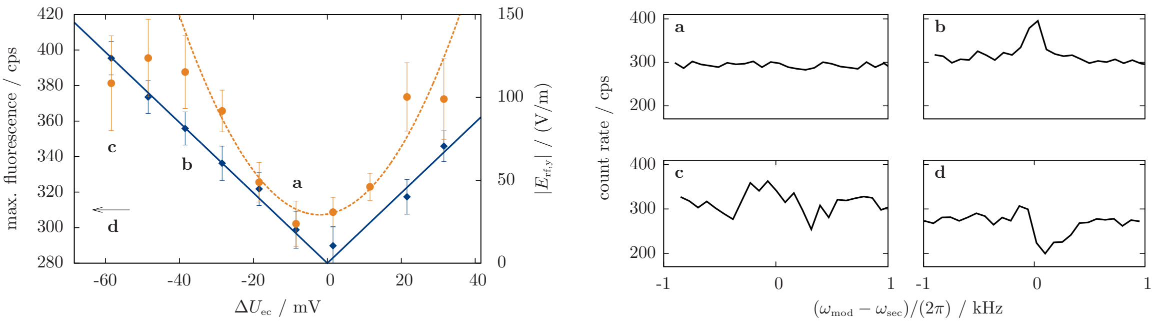

Figure 6.16.: Parametric excitation signals. Left: fluorescence at the parametric resonance as the ion is shifted radially through the trap (orange circles; mean and standard deviation of 10 sweeps each). A parabola is fitted to the six innermost data points to determine the position of the minimum. Intermittent photon-correlation measurements are used to quantify the amount of excess micromotion (blue diamonds). Right: examples of signals obtained in different micromotion amplitude regimes. Small displacements from the rf node lead to an increase of fluorescence, whereas large displacements produce a fluorescence decrease. Labels **a** to **d** indicate the corresponding data points in the left graph.

momentum imparted by absorbed photons [68] over one period of secular motion:

$$\dot{E}_{\mathrm{cool}} = \frac{I}{I_{\mathrm{sat}}} \hbar k v_0 \frac{\Gamma}{4\pi} \int_0^{2\pi} \frac{\sin(t')}{1 + \left(\frac{2(\Delta - k v_0 \sin(t'))}{\Gamma}\right)^2} dt' \tag{6.25}$$

$$\text{with } v_0 = \sqrt{\frac{k_B T}{m}} ,$$

where k is the projection of $\vec{k}$ onto the principal axis of the mode, and it is assumed that $I \ll I_{\mathrm{sat}}$. Equation 6.25 neglects heating due to the recoil from emitted photons, which has negligible influence for temperatures far above the Doppler limit. Figure 6.15b shows the numerically calculated values of Eq. 6.25 as a function of T.

The heating rate due to parametric excitation has been derived by Savard et al. [150]. To give an example, for the experimental parameters used below and $E_{\mathrm{rf}} = 100\,\mathrm{V/m}$, the initial heating rate at $T = 0.5\,\mathrm{mK}$ is on the order of $10^{-21}\,\mathrm{J/s}$. In the experiments, the fluorescence begins to drop for $E_{\mathrm{rf}} > 100\,\mathrm{V/m}$, indicating that the equilibrium temperature exceeds 200 mK at this point.

6.4.2. Experimental results

The parameters for parametric excitation measurements are chosen as a compromise between sensitivity and robustness. As shown in Fig. 6.15, a higher detuning of the cooling laser from resonance widens the temperature range for which both fluorescence and cooling rate increase with increasing temperature. The measurements are performed at a detuning $\Delta = -3\Gamma/2$ and intensity $I/I_{\text{sat}} \approx 0.01$. The parametric resonance is excited by an amplitude modulation of the rf voltage, which modulates the secular frequency as

$$\omega_{\text{sec}}(t) = \omega_{\text{sec},0}\left(1 + m_0 \sin(\omega_{\text{mod}} t)\right) \ , \tag{6.26}$$

with $\omega_{\text{sec},0} = 2\pi \times 500\,\text{kHz}$, and $m_0 = 0.04$. The modulation frequency ω_{mod} is swept over a range of $2\pi \times 2\,\text{kHz}$ around $\omega_{\text{sec},0}$ during 30 s. Figure 6.16 shows a parametric heating measurement as the ion is moved along the x direction using the compensation voltage U_{ec}. Each point is derived from the maximum fluorescence of the average of 10 modulation frequency sweeps, examples of which are shown in the right part of the figure. Interleaved photon-correlation measurements are performed to quantify the amount of micromotion along y. It should be noted that the two measurements are sensitive to displacements along different axes: while the amount of vertical micromotion determined by photon-correlation is proportional to the x displacement, the strength of parametric excitation depends on the displacement along the respective principal axis, which is at about $-48\,^\circ$ from the x axis. This dependence has been verified by displacing the ion by the same amount in different directions. To ensure that the minima in Fig. 6.16 coincide, the y displacement of the ion was minimized beforehand using U_{tc} and photon-correlation measurements with the horizontal beams. The fitted minima agree to within $\Delta U_{\text{ec}} = 2\,\text{mV}$, corresponding to a mismatch of $E_{\text{rf}} = (4.6 \pm 3.7)\,\text{V/m}$. The sensitivity of the parametric excitation method can be increased by lowering the trapping potential in order to increase the displacement due to a given residual static field E_{dc}.

Parametric excitation could also be used to find the position with minimal axial micromotion. However, the contribution of the rf field to the axial trapping potential strongly depends on the electrode geometry and is ideally negligible by design, in particular when compared to the static axial potential. Exciting axial motion would therefore require a much stronger modulation of the rf voltage. To give an example, the expected ponderomotive potential due to residual axial rf fields for the current geometry corresponds to about 200 Hz according to FEM calculations, and the measured amplitude in the prototype (see section 6.6.2) corresponds to a $\approx 3\,\text{kHz}$ confinement.

6.5. Comparison of the techniques

6.5.1. Resolution limits

Table 6.1 summarizes the resolution limit observed for a single measurement with each method.

method	$\beta \times 10^3$	$E_{\mathrm{rf}}\,/(\mathrm{V/m})$	$E_{dc}\,/(\mathrm{V/m})$	$\lvert\Delta\nu_{\mathrm{D2}}/\nu\rvert \times 10^{20}$
sideband (T_{Doppler})	17 ± 16	50 ± 48	0.6 ± 0.6	8.5 ± 16
photon-correlation	2.7 ± 2.7	7.1 ± 7.2	0.09 ± 0.09	0.17 ± 0.35
parametric excitation		≤ 23	≤ 0.3	≤ 1.8

Table 6.1.: Comparison of the observed minima to demonstrate the sensitivity achieved in a single measurement with each technique.

In sideband measurements, the resolution is limited by the lowest observable Rabi frequency on the sideband and the available laser power. The maximum carrier Rabi frequency in this experiment is currently $\Omega_0 = 2\pi \times 140\,\mathrm{kHz}$, limited by the output power of the SHG for the 411 nm light. The sideband Rabi frequency resolution is $\Omega_{\pm 1} = 2\pi \times 500\,\mathrm{Hz}$, limited by the magnetic field fluctuations on the order of 30 nT between experimental cycles. The lowest resolvable modulation index due to these technical limitations is $\beta = 0.007$, which corresponds to $E_{\mathrm{rf}} = 21\,\mathrm{V/m}$. At a temperature of 0.5 mK however, the minimum observed sideband excitation is limited by IMM, as described in section 6.2.1. The fit uncertainty in obtaining $\Omega_{0,\pm 1}$ from measurements using an ion at the Doppler limit is about 10 %. Taking all these contributions into account, the experimentally observed minimum is $E_{\mathrm{rf}} = (50 \pm 48)\,\mathrm{V/m}$ for an ion at the Doppler temperature. In the ground state, the expected IMM contribution corresponds to less than $1\,\mathrm{V/m}$ and Rabi frequencies can be determined more precisely.

The photon correlation method is limited by shot noise, as discussed in section 6.3.2. It contributes about $5\,\mathrm{V/m}$ to the uncertainty in E_{rf} for an integration time of 90 s. Taking into account the additional uncertainty contributions, the observed minimum is $\beta = (2.7 \pm 2.7) \times 10^{-3}$, which corresponds to $E_{\mathrm{rf}} = (7.1 \pm 7.2)\,\mathrm{V/m}$.

For the parametric excitation method, the statistical uncertainty of the fluorescence peak is given, as shown in Fig. 6.16. It is dominated by photon shot noise and corresponds to $E_{\mathrm{rf}} = 23\,\mathrm{V/m}$.

6.5.2. Applicability during operation in a multi-ion clock

During clock operation, varying external electric fields need to be compensated at regular intervals. If the frequency feedback to the clock laser is interrupted while the new compensation voltage values are determined, the required uncertainty should be achieved as quickly as possible [151]. This section compares the time consumption of the micromotion compensation techniques for a single ion. In a multi-ion clock, an initial evaluation over the full extent of the ion crystal is necessary in order to determine the frequency shifts of the individual ions. However, for crystals with a small extension compared to the distance from the electrodes, it is reasonable to approximate fluctuating fields as homogeneous. Drifts in EMM can therefore be compensated using measurements on a single ion as well. If necessary, the Coulomb crystal can meanwhile be stored in a separate trap segment.

As shown above, the quantitative dependence of micromotion on the radial displacement can be mapped precisely, see, e.g. Fig. 6.14. A single measurement per dimension is therefore sufficient to determine the minimum. A controlled displacement is needed to resolve the sign ambiguity when sideband or parametric heating measurements are used. For photon-correlation measurements, the sign is given by the phase of the modulation signal and no displacement is necessary.

The resolution of a photon-correlation measurement is limited by shot noise for low EMM amplitudes, as shown in section 6.3.2. According to the fit shown in Fig. 6.13, 10 s of measurement per dimension would therefore be sufficient to reduce the respective uncertainty in the 2nd-order Doppler shift to 1×10^{-20}. Since the signals can be derived from the fluorescence during Doppler cooling, there is no fundamental need to interrupt clock operation at all when applying this method. Multiple cooling beams from different directions with alternating attenuation could allow three-dimensional micromotion measurements without deteriorating the ion temperature. Fluorescence detection with a camera allows the application to a full Coulomb crystal simultaneously, but fast gating is necessary to resolve fractions of a micromotion period. This can be achieved with an image intensifier [152]. The integration time required for a given SNR increases considerably with this method, since photons outside the gate pulse are disregarded.

In a sideband measurement without ground state cooling, the acquisition of a single data point (200 cycles) takes at least 2 s, limited by the time required for state detection and repumping. Total time consumption per dimension is therefore on the order of 10 s. Since the optimal compensation voltage is extrapolated from a measurement with added EMM, it is affected less by the IMM contribution and decoherence than measurements with minimized EMM. Position-resolved state detection with an EMCCD camera allows simultaneous measurements across an ion crystal, albeit with a reduced resolution due the Debye-Waller effect from the increasing number of secular modes.

Parametric heating measurements need to be performed within the regime of monotonic dependence of the fluorescence peak on the micromotion amplitude if the minimum is to be deduced from a single data point. The choice of parameters therefore requires a trade-off between robustness and resolution. As the fluorescence value depends on the equilibrium temperature in the presence of heating, laser cooling parameters need to be well controlled in order to achieve reproducible values. On a timescale of hours, the secular frequency instability is on the order of 100 Hz, which is comparable to the width of the parametric resonance.

method	advantages	limitations	resolution	time per point
sideband	fast acquisition measures ratio Ω_1/Ω_0 $\rightarrow$ common mode effects cancel	resolution limited by – decoherence – laser power	3×10^{-20} $\sigma_\beta = 0.007$	$< 10\,\mathrm{s}$
photon-correlation	contains phase information $\rightarrow$ E_{rf} direction can be inferred, rf phase shift / displacement distinguishable applicable continuously during clock operation	resolution limited by – photon shot noise	3.5×10^{-21} $\sigma_\beta = 0.0027$	10 s to 100 s (no dead time)
parametric excitation	simple implementation no 3D laser access required	no quantitative evaluation insensitive to rf phase shift	2×10^{-20}	10 s to 100 s

Table 6.2.: Summary of the evaluated micromotion detection methods. Resolutions are given in terms of the second-order Doppler shift; the sideband value assumes that the offset described in section 6.2.1 is negligible, as, e.g. for a groundstate cooled ion. For the quantitative methods, the corresponding uncertainty in the modulation index σ_β is indicated.

This requires either an active stabilization of U_{rf} or a scan of the modulation frequency. Assuming an averaging time of 10 s per modulation frequency, total time consumption is therefore on the order of 10 to 100 s.

Table 6.2 summarizes the advantages and limitations of the investigated methods and lists the achieved resolutions and time consumption.

6.6. Trap characterization

Micromotion measurements can reveal a number of important properties of the setup. Understanding the electric fields resulting from voltages applied to the various electrodes is essential in the development of ion traps for precision spectroscopy. This section shows how EMM amplitudes are used to deduce these field amplitudes in order to understand the current setup and test the trap design and manufacturing tolerances. In addition, fluctuations of external fields need to be characterized in order to estimate the timescale for compensation voltage adjustments to keep uncertainties below 10^{-18}.

6.6.1. Compensation voltage electric fields

The EMM amplitude can act as an experimental reference for ion displacements, since its amplitude and direction can be calculated from the rf and dc components of the radial potential, which in turn can be determined accurately from measurements of the radial secular frequencies and Lamb-Dicke parameters. From the motional sideband spectrum (see

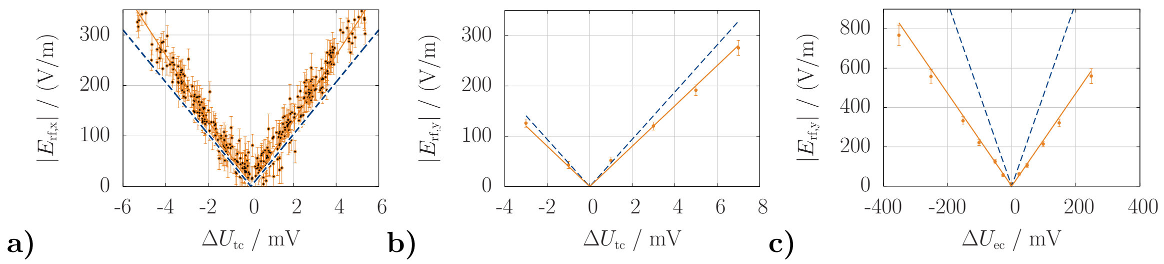

Figure 6.17.: Comparison of the measured micromotion components induced by varying the compensation voltages (solid lines) to the values expected from FEM calculations (dashed lines). The $E_{\mathrm{rf,x}}$ component induced by U_{ec} is negligible in both calculation and experiment. Graph **a** uses data recorded as part of the regular EMM compensation over the course of four months.

Ch. 5), the following trap parameters have been deduced:

$$\begin{aligned} a_{\mathrm{rad,i}} &= \frac{2}{\Omega_{\mathrm{rf}}^2}\left(-\omega_{\mathrm{ax}}^2 \pm \left|\omega_{\mathrm{rad,1}}^2 - \omega_{\mathrm{rad,2}}^2\right|\right) = (-1.0 \pm 1.4) \times 10^{-4}\ , \\ q_i &= \pm\frac{2}{\Omega_{\mathrm{rf}}}\sqrt{\omega_{\mathrm{rad,1}}^2 + \omega_{\mathrm{rad,2}}^2 + \omega_{\mathrm{ax}}^2} = \pm 0.054\ , \end{aligned} \tag{6.27}$$

and the strong principal axis is oriented at $\theta_> = 48.5\,^\circ$ from x.

The amplitude and orientation of micromotion induced by varying the compensation voltages allows a deduction of the electric field applied at the position of the ion. The displacement Δx resulting from an applied field E_{dc} is derived by equating the force eE_{dc} of the field with the restoring force $m\omega^2\Delta x$ of the trapping potential. From Δx, the rf electric field, and therefore the EMM amplitude can be calculated:

$$E_{\mathrm{rf}} = \frac{4}{q\left(1 + \frac{2a}{q^2}\right)} E_{\mathrm{dc}} \approx \frac{\sqrt{2}\Omega_{\mathrm{rf}}}{\omega} E_{\mathrm{dc}} \quad \text{if} \quad a \ll \frac{q^2}{2}\ . \tag{6.28}$$

If the ellipticity of the potential cannot be neglected, the orientation of the principal axes with respect to the applied field needs to be taken into account.

Figure 6.17 shows the expected and measured E_{rf} components due to U_{tc} and U_{ec}. From graphs a and b, it seems as if the actual field due to U_{tc} is rotated toward the y axis with respect to the calculated value. One possible reason could be a smaller distance between the inner electrodes, e.g. due to sightly bent wafers (cf. Fig. 6.1). An alternate explanation would be a clockwise rotation of the rf quadrupole, leading to a rotated reference for all of these measurements. However, while the FEM calculations show a 1.7 ° clockwise rotation, 35 ° would be necessary in order to fully explain the discrepancy. This would clearly show

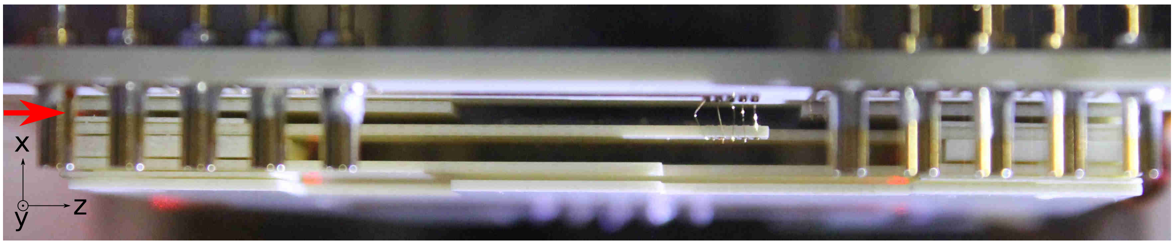

Figure 6.18.: Top view of the real trap. The arrow indicates a gap between one of the compensation wafers and the rest of the stack, which is a possible explanation for the weaker field from the compensation voltage U_{ec}.

up as an $E_{\mathrm{rf,x}}$ component due to U_{ec}, which is not observed in the experiments. Figure 6.17c shows that the field applied by U_{ec} is significantly weaker than expected. This could be due to a larger separation of the compensation wafers. A photo of the trap, shown in Fig. 6.18 supports this hypothesis: it seems that one of the compensation wafers and the rest of the stack have become separated at the top end. All of these geometric assumptions can be tested more thoroughly once the trap prototype is taken out of the vacuum chamber to be replaced by the next generation trap.

6.6.2. Axial excess micromotion

While the radial rf field components are essential for the confinement, an ideal linear trap would not produce any axial rf field component. This is different for real traps, where the translational symmetry is broken due to the finite extension of the electrodes, the segmentation, and manufacturing tolerances. Since a compensation of axial rf fields is not feasible, especially when multiple ions are to be stored along the trap axis, they are best eliminated by design. Extensive FEM calculations have therefore been performed to ensure sufficiently low axial rf fields in the traps used in this work [28].

The goal was to maximize the range with an axial rf field amplitude $|E_{\mathrm{rf,z}}| < 115\,{}^{\mathrm{V}}\!/\mathrm{m}$, which corresponds to $|\Delta\nu_{2\mathrm{D}}/\nu| < 1 \times 10^{-18}$ for $^{115}\mathrm{In}^+$, in order to store linear crystals for clock operation. Figure 6.19 shows a three-dimensional photon-correlation measurement while shifting an ion along the z axis. The radial compensation voltages are kept at constant values throughout.

The fitted slope is $(7.4\pm0.1)\,({}^{\mathrm{V}}\!/\mathrm{m})/\mu\mathrm{m}$, which corresponds to a region of $31\,\mu$m with $|E_{\mathrm{rf,z}}| \leq 115\,{}^{\mathrm{V}}\!/\mathrm{m}$. This is about an order of magnitude less than expected for this geometry, according to FEM calculations. Storing a linear chain of 10 $^{115}\mathrm{In}^+$ ions within $31\,\mu$m requires an axial trap frequency of 500 kHz and radial frequencies above 2.6 MHz [67], which means an 8-fold (6-fold) increase in dc (rf) voltage and is therefore not feasible. It has however already been

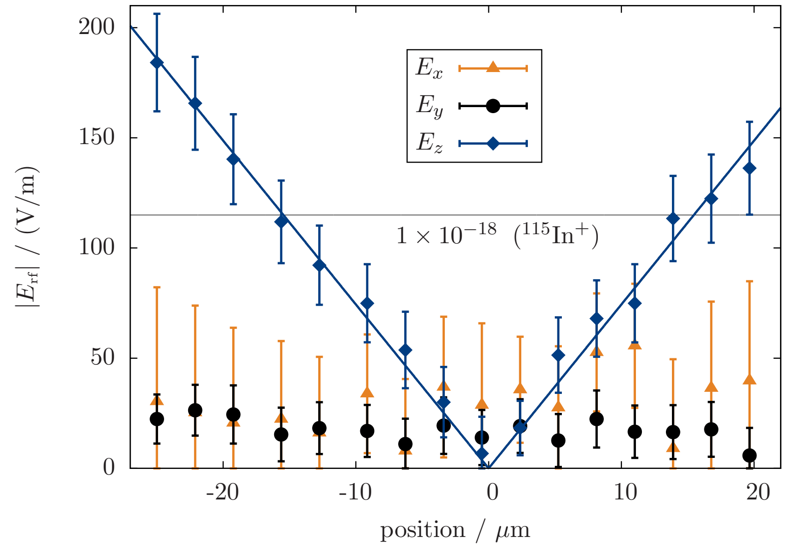

Figure 6.19.: Measurement of the axial rf field component in the milled Rogers prototype trap. The region with $|E_{\mathrm{rf,z}}| \leq 115\,\mathrm{V/m}$ has a length of $31\,\mu$m.

shown that $|E_{\mathrm{rf,z}}|$ is a factor of two lower in a laser-cut version of the same trap [33], and calculations for the next trap generation geometry promise $|E_{\mathrm{rf,z}}| \leq 60\,\mathrm{V/m}$ across the entire trapping region for $U_{\mathrm{rf}} = 1\,\mathrm{kV}$.

6.6.3. Long-term drift of electric stray fields

Photon-correlation measurements have been used to compensate stray fields at least once per day before every measurement reported in this chapter. As the electric fields from the compensation voltages are not linearly independent, compensation consists of first finding the minimum of $E_{\mathrm{rf,x}}$ with respect to U_{tc} and then minimizing the remaining $E_{\mathrm{rf,y}}$ component with U_{ec}. The resulting pairs of voltages allow an analysis of the long-term behavior of electric stray fields in the trapping region. Figure 6.20 shows the optimal voltages over the course of three months. Typical day-to-day fluctuations are $\lesssim 100\,\mathrm{V/m}$, corresponding to a fractional 2nd-order Doppler shift of about 1×10^{-18}. Multiple measurements on the same day typically show shifts on the order of a few $10\,\mathrm{V/m}$. It therefore seems feasible to keep the 2nd-order Doppler shift negligible at a level of 10^{-18} with compensation voltage adjustments on the timescale of a few hours. It is not clear what caused the additional diagonal field between December and January or the temporary vertical component in February. The latter appeared during the week after an air conditioning failure and might be the result of mechanical deformation.

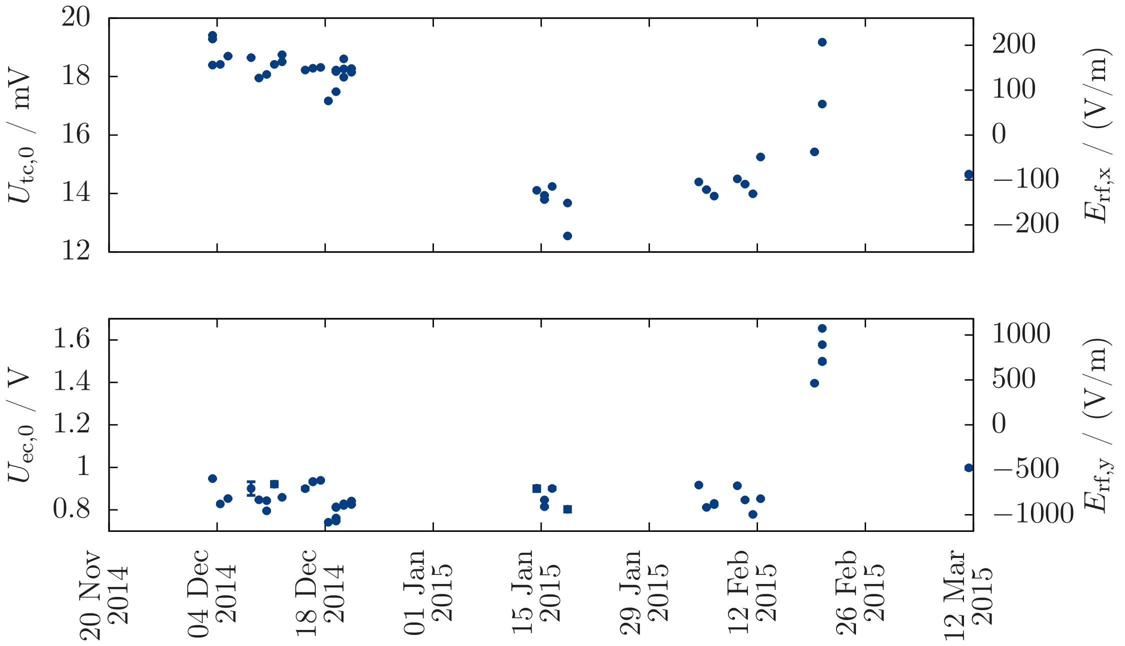

Figure 6.20.: Long-term drift of electric stray fields. Note that the fields from the two voltages are not linearly independent and in order to compensate vertical stray fields, U_{ec} needs to compensate the accompanying horizontal influence of U_{tc}. The uncertainties are smaller than the symbols for most values. The right ordinates are for orientation and have arbitrary offsets.

In summary, it has been shown that the frequency shift due to EMM can be determined with uncertainties below 10^{-19} with methods relying on the 1st-order Doppler shift. Of these methods, the photon-correlation technique seems the most promising for clock operation, since it can be applied without interrupting the spectroscopy sequence.

7. Summary and outlook

This thesis contributes toward the realization of an optical clock based on Coulomb crystals, which will benefit from the low systematic uncertainties achievable in spectroscopy with trapped ions, but require shorter averaging times than the currently employed single-ion approach. $^{115}\mathrm{In}^+$ ions will be used as the frequency reference, while $^{172}\mathrm{Yb}^+$ ions will provide sympathetic cooling. The setup of two ultra-stable reference cavities and spectroscopic determination of the ion motion are described.

For short-term stabilization of the clock laser, a 30 cm long ULE cavity with a simple spacer design has been set up and characterized. The expected thermal noise floor and the measured vibration sensitivity are sufficiently low to achieve a fractional frequency instability of $\sigma_y = 1 \times 10^{-16}$ for averaging times $> 30\,\mathrm{ms}$ under normal laboratory conditions. With a laser stabilized to this cavity, it will be possible to operate a frequency standard based on 100 $^{115}\mathrm{In}^+$ ions at its QPN limit of $7.2 \times 10^{-17}/\sqrt{\tau/\mathrm{s}}$. Further contributions to laser frequency instability have been investigated with a simpler 12 cm long cavity. An ECDL stabilized to this cavity reaches an instability of $\sigma_y = 6 \times 10^{-16}$ in 1 s. The limiting contributions are thermal noise, environmental vibrations and unsuppressed high-frequency noise of the diode laser. While the first two will be reduced for the $^{115}\mathrm{In}^+$ clock laser with the use of the 30 cm cavity, the intrinsic laser noise at high Fourier frequencies is expected to be significantly lower, since a solid-state laser can be used to address the clock transition in $^{115}\mathrm{In}^+$.

In today's best ion-based optical clocks, time dilation due to ion motion is among the limiting contributions to the frequency inaccuracy. Reducing this uncertainty while at the same time increasing the number of ions is the main technical challenge for the implementation of a clock based on Coulomb crystals. It is addressed partially by the development of a segmented linear Paul trap with low axial rf field components [28, 33, 34], and partially by precise determination of the residual motional amplitudes. The work presented here contributes to the latter by providing the means to measure the motional excitation spectroscopically, at a level corresponding to 2nd-order Doppler shift uncertainties below 10^{-18}. Both secular motion and micromotion are addressed.

Ion motion is observed by spectroscopy on the 411 nm $^2\mathrm{S}_{1/2} \leftrightarrow {}^2\mathrm{D}_{5/2}$ line in $^{172}\mathrm{Yb}^+$ with the aforementioned highly stable ECDL. State detection with an EMCCD camera has been implemented to obtain a spatial resolution in ion crystals. For a single ion in which two motional modes are addressed simultaneously, the temperature after Doppler cooling has been determined with an uncertainty below 20 % from the dephasing of Rabi oscillations, corresponding to an uncertainty in the resulting 2nd-order Doppler shift of 2×10^{-19}.

Groundstate cooling of the two radial modes has been implemented with a single ion in order to resolve the motional heating rates of the ion trap. These could be determined to be below $2\,\mathrm{s}^{-1}$ at secular frequencies of about 500 kHz, and correspond to a 2nd-order Doppler shift for an uncooled indium ion of $-2.5(10) \times 10^{-20}\,\mathrm{s}^{-1}$. As part of the cooling sequence, the $^2\mathrm{D}_{5/2}$ state is depleted via the transition to the $^2\mathrm{P}_{3/2}$ state, the frequency of which has been determined as $\nu = 181.65947(19)\,\mathrm{THz}$ ($\lambda_{\mathrm{vac}} = 1650.2991(17)\,\mathrm{nm}$). Better control of the frequency will be achieved by observing the second harmonic of the laser on the more accurate wavemeter already used for the stabilization of most other lasers. This will permit a continuous cooling scheme instead of the current pulsed one, which will significantly reduce the cooling time as well as losses to the metastable $^2\mathrm{F}_{7/2}$ state during cooling. Driving the 1650 nm transition also strongly improves the efficiency of the $^2\mathrm{F}_{7/2}$ clearout with 639 nm radiation, as it avoids population cycling via the decay $^1[5/2]_{5/2} \rightarrow {}^2\mathrm{D}_{5/2} \rightarrow {}^2\mathrm{F}_{7/2}$. A characterization of the repumping process has determined a new upper bound of 5 ms for the lifetime of the $^1[5/2]_{5/2}$ state. The current limitation of cycle time to about 20 ms by the repumping process will be improved with a more powerful laser diode at 639 nm.

Besides secular motion, frequency shifts due to EMM are crucial. Three established methods for the detection of micromotion have been investigated in terms of their suitability at a level of 10^{-18} and below and their applicability in clock operation. Although the technique is in widespread use, the only previously published model for a quantitative evaluation of photon-correlation measurements [32] is not applicable in the very common regime of comparable trap drive frequency and transition linewidth. A refined model is presented in this thesis along with the verification of its validity by a comparison with resolved-sideband measurements. A study of experimental sources of uncertainty reveals an achievable micromotion amplitude resolution corresponding to frequency shifts below 10^{-20}. Moreover, the technique can be applied without interrupting clock operation by using the fluorescence emitted during Doppler cooling, which is a significant advantage in terms of frequency stability.

If not performed deep within the Lamb-Dicke regime, resolved-sideband EMM measurements exhibit an offset due to sampling of IMM, which for the current experimental parameters ($\omega_{\mathrm{sec}} \approx 2\pi \times 500\,\mathrm{kHz}$, $q \approx 0.05$, $\eta \approx 0.1$) is on the order of a few 10^{-19} for Doppler cooled ions. A theoretical description is in agreement with the experimental observations. The effect scales as $\propto q\eta^2\bar{n}$ and is expected to be on the same order for other trapped ion optical clock setups, e.g. the PTB and NPL ytterbium ion clocks ($q \approx 0.1$ and $\omega_{\mathrm{sec}} \approx 2\pi \times 600\,\mathrm{kHz}$ and 1 MHz, respectively [153]).

An imminent major step is the replacement of the Rogers prototype trap with the next generation trap built from AlN wafers. An increased rf voltage will allow radial frequencies

	$\lvert\Delta\nu/\nu_0\rvert \times 10^{18}$	$\sigma\left(\lvert\Delta\nu/\nu_0\rvert\right) \times 10^{18}$	**reference**
2nd-order Doppler shift (single ion thermal motion at 0.5 mK)	-1	< 0.2	Ch. 5
2nd-order Doppler shift (per second without cooling)	-0.025	0.01	Ch. 5
2nd-order Doppler shift (EMM)	0	< 0.1	Ch. 6
2nd-order Stark shift (trap rf) (single ion thermal motion at 0.5 mK)	-0.02	< 0.01	[29], Ch. 5
black-body radiation (BBR) AC Stark shift at 300 K	-13.6	< 0.1	[29, 153]
2nd-order Zeeman shift	< 0.1	< 0.1	[28]

Table 7.1.: Expected atomic contributions to the uncertainty budget of an indium clock. The BBR shift uncertainty only includes the temperature contribution [153], not the uncertainty of the calculated differential polarizability, which is currently on the order of 1×10^{-18} at 300 K [29], but is likely to be reduced by an experimental determination.

of at least 1.5 MHz, which will benefit spectroscopy through a reduced motional dephasing at Doppler temperatures and improve the initial conditions for sideband cooling. An optimized electrode geometry and lower manufacturing tolerances are expected to result in axial rf fields below 60 V/m across the entire trapping region at a drive voltage of 1 kV, permitting the storage of a linear crystal with axial EMM shifts below 3×10^{-19}.

The new trap has also been optimized to reduce the uncertainty due to the thermal environment experienced by the ions. This includes the use of materials with low rf losses and good heat conductivity, as well as a thermal model of the trap, which has been refined by measurements with a prototype [153]. With the help of this model, the black-body spectrum experienced by the ion can be determined to within 0.1 K using onboard temperature sensors. In combination with the comparatively low sensitivity of the $^{115}\mathrm{In}^+$ clock transition to the AC Stark shift from black-body radiation (BBR) [29], the resulting uncertainty can be expected to be well below 10^{-19}. This estimate does not include the uncertainty of the differential static polarizability, which currently amounts to 1×10^{-18} at 300 K for the calculated value reported in [29]. However, an improvement can be expected from an experimental determination, using either an infrared laser [35, 154], or controlled heating of the trap with the onboard thermistors.

Table 7.1 summarizes the expected atomic contributions to the systematic frequency uncertainty of an indium ion clock. The uncertainties of the first four contributions benefit from the work presented in this thesis. The last line points out another advantageous property of $^{115}\mathrm{In}^+$: The second-order Zeeman shift of $4.1\,\mathrm{Hz}/\mathrm{mT}^2$ is considerably lower than for other clock transitions. The value given in the table assumes $B^2_{\mathrm{rms}} = 2 \times 10^{-11}\,\mathrm{T}^2$, as observed in a different setup due to unbalanced currents in the trap feeds [36].

In a continuation of the experiments presented here, the trap characterization with a single ion will first be repeated in the AlN trap, before the ion number is successively increased. Spectroscopy on multiple ions will be facilitated by the addition of a voltage that adjusts the radial principal axis orientations, which can reduce the number of modes with projections onto the spectroscopy laser by a factor of two. A slave laser system at 411 nm will permit the expansion of the beam radius along the trap axis for addressing multiple ions simultaneously without a decrease in Rabi frequency. The next major goal is to perform simultaneous resolved-sideband EMM measurements with multiple ions and temperature measurements with a mixed-species crystal to determine the achievable frequency inaccuracy in a multi-ion clock.

In the long-term, this experiment will provide the means to store Coulomb crystals with well-understood motional shifts by a combination of trap development and precise measurements of the motional excitation. Apart from the current approach for an $^{115}\mathrm{In}^+$ clock with improved short-term instability, ion clocks based on other species can benefit from the results of this development. Those based on narrower transitions, which are currently limited by the clock laser instability, can benefit even more from an increased number of ions by using more elaborate interrogation schemes [56–59]. Candidates include Al^+ [45] and possibly the Yb^+ octupole transition, owing to the low electric quadrupole moment of the $^2\mathrm{F}_{7/2}$ state [35].

The high degree of control over the electric potential acting on trapped ions also opens up the possibility to use the present setup for the study of non-equilibrium dynamics in Coulomb crystals, which can act as a highly controllable laboratory model in the intermediate regime between a single atom and a solid state system. Work performed by the author has contributed to multiple research papers on the subject [155–157], which has been omitted in this thesis to focus on the topic of spectroscopy. This setup has been used [155, 157] to study the dynamics during the second-order phase transition [158] which a crystal undergoes as the trap aspect ratio is lowered and the equilibrium configuration changes from a linear chain to a two-dimensional "zig-zag" arrangement. When this transition is crossed non-adiabatically, the crystal structure can exhibit topological defects ("kinks"), as shown in Fig. 7.1, which behave as quasi-particles and are an example of discrete solitons. The effective potential seen by these kinks has been investigated and controlled by applying external electric fields and by adding mass defects to the crystal [156]. These experiments provide a foundation for the use of ion crystals to study the physics of solitons. The addition of a narrow spectroscopy

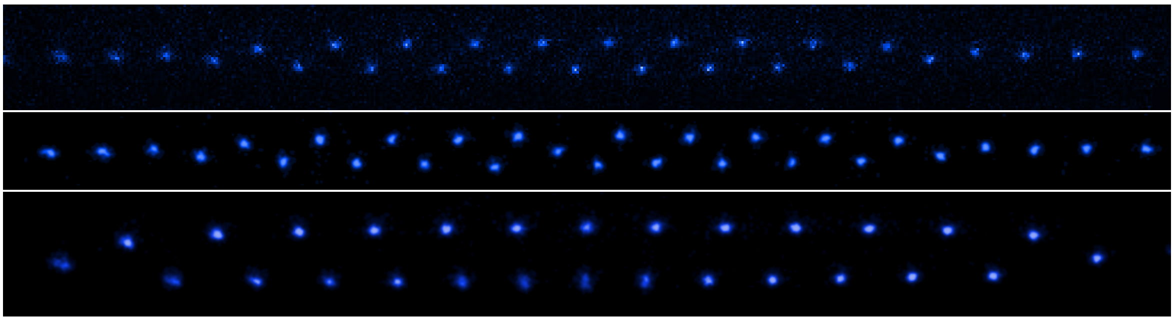

Figure 7.1.: Topological defects in Coulomb crystals. The top image shows a two-dimensional crystal without defects. If the phase transition from a linear chain to this configuration is crossed non-adiabatically, topological defects can form, as shown in the lower two images. The defect geometry depends on the trap aspect ratio.

laser to the setup provides a new experimental tool for such studies, as kinks exhibit localized high-frequency modes of oscillation [159, 160]. These modes are well decoupled from the rest of the mode spectrum and have therefore been suggested for the storage of quantum information and entanglement generation [161].

Finally, the spatially resolved detection is ideally suited for studying heat transport within Coulomb crystals [162]. The low axial rf field component allows a weak axial confinement without distortion by ponderomotive forces. With the resulting high inter-ion distance, the phonon tunneling rate [163] is reduced to below 10 kHz, and the dynamics are slowed down sufficiently to be observed with resolved-sideband spectroscopy. For faster processes, other techniques are required to determine the motional states, such as the observation of a dark resonance in a fast transition [164] or Ramsey interferometry combined with spin-dependent displacement of the motional state [165].

Besides advancing toward clock spectroscopy in mixed-species crystals, studies of heat transport are planned for the near future, after the new AlN trap has been set up and characterized.

A. ^{172}Yb^{+} spectroscopic data

States

Term	$E/\,\mathrm{cm}^{-1}$ [82]	τ_{calc}	τ_{obs}	g_{calc} [82]	g_{obs} [82]
$4f^{14}6s\ ^2\mathbf{S}_{1/2}$	0	-	-	2.000	1.998
$4f^{13}6s^2\ ^2\mathbf{F}_{7/2}$	21418.75(2)	4.1 yr [166]	10^{+7}_{-4} yr [120]	1.143	1.145
$4f^{14}5d\ ^2\mathbf{D}_{3/2}$	22960.80(2)	40 ms [166]	52.15(100) ms [167]	0.800	1.802
$4f^{14}5d\ ^2\mathbf{D}_{5/2}$	24332.69(2)	5.2 ms [166]	7.0(4) ms [81]	1.200	1.202
$4f^{14}6p\ ^2\mathbf{P}_{1/2}$	27061.82(2)	8.60 ns [79]	8.12(2) ns [168]	0.667	0.667
$4f^{14}6p\ ^2\mathbf{P}_{3/2}$	30392.23(2)	7.23 ns [79]	6.15(9) ns [169]	1.333	1.333
$4f^{13}5d6s\ ^2\mathrm{F}_{7/2}\ ^3[3/2]_{1/2}$	33653.86(2)	32.10 ns [79]	37.7(5) ns [170]	1.318	1.320
$4f^{13}5d6s\ ^2\mathrm{F}_{7/2}\ ^1[5/2]_{5/2}$	37077.59(2)		≤ 5 ms (see 5.3.2)	1.113	1.113

Transitions

States	$\lambda_{\mathrm{vac}}/\,\mathrm{nm}$	$A_{\mathrm{calc}}/\,\mathrm{s}^{-1}$	$A_{\mathrm{obs}}/\,\mathrm{s}^{-1}$	**Function**
$^2S_{1/2} \leftrightarrow {}^2P_{1/2}$	369.5243(3) [82]	$1.155 \cdot 10^8$ [79]	$122.3(3) \cdot 10^6$ [120, 168]	cooling/det.
$^2D_{3/2} \leftrightarrow {}^2P_{1/2}$			$0.862(2) \cdot 10^6$ [120, 168]	
$^2D_{3/2} \leftrightarrow {}^3[3/2]_{1/2}$	935.1860(25) [82]	$0.555 \cdot 10^6$ [79]	$0.504(40) \cdot 10^6$ [120, 170]	clear out $^2D_{3/2}$
$^2S_{1/2} \leftrightarrow {}^3[3/2]_{1/2}$			$26.02(17) \cdot 10^6$ [120, 170]	
$^2S_{1/2} \leftrightarrow {}^2D_{5/2}$	410.9691077(1) [122]		24.29(576) [81, 122]	spectroscopy/sbc
$^2F_{7/2} \leftrightarrow {}^2D_{5/2}$			118.57(546) [81, 122]	
$^2F_{7/2} \leftrightarrow {}^1[5/2]_{5/2}$	638.615(1) [120]			clear out $^2F_{7/2}$
$^2D_{5/2} \leftrightarrow {}^2P_{3/2}$	1650.2903(77) [82]	$1.41 \cdot 10^6$ [79]		quench $^2D_{5/2}$
	1650.2991(17) (Ch. 5)			
$^2S_{1/2} \leftrightarrow {}^2P_{3/2}$		$1.37 \cdot 10^8$ [79]		

B. Photo-ionization schemes

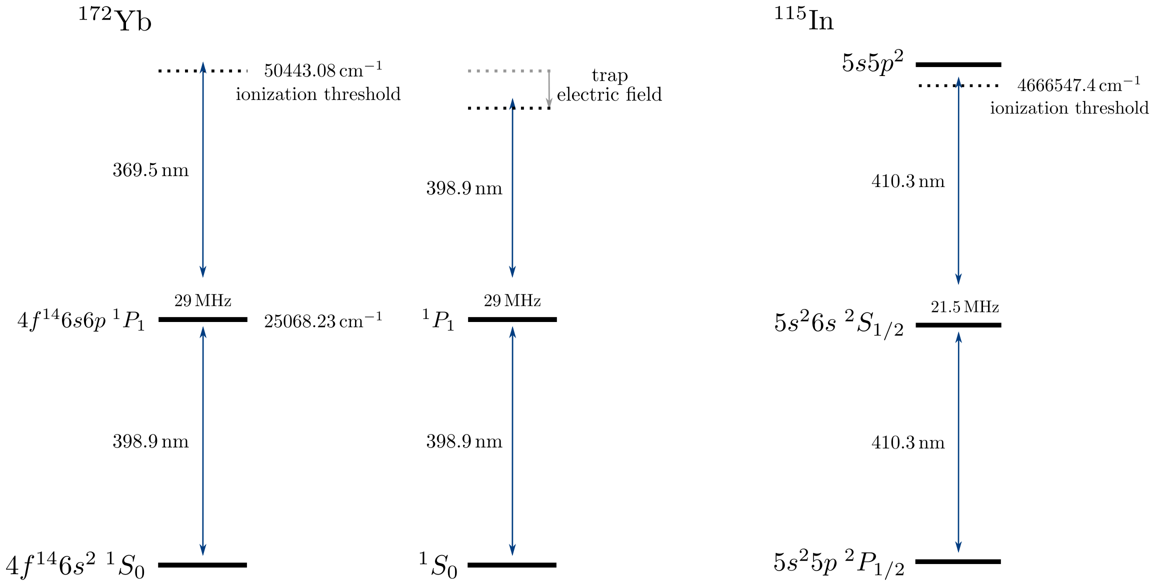

^{172}Yb
50443.08 cm^{-1}
ionization threshold
369.5 nm
29 MHz
$4f^{14}6s6p\ ^1P_1$
25068.23 cm^{-1}
398.9 nm
$4f^{14}6s^2\ ^1S_0$
trap
electric field
398.9 nm
29 MHz
$^1P_1$
398.9 nm
$^1S_0$
^{115}In
$5s5p^2$
4666547.4 cm^{-1}
ionization threshold
410.3 nm
21.5 MHz
$5s^26s\ ^2S_{1/2}$
410.3 nm
$5s^25p\ ^2P_{1/2}$

	^{172}Yb	^{115}In
Ionization threshold	50443.08(5) cm^{-1} [171]	5.786358 eV [172]
Transition	$4f^{14}6s^2\ ^1\mathbf{S}_0 \leftrightarrow 4f^{14}6s6p\ ^1\mathbf{P}_1$	$5s^25p\ ^2\mathbf{P}_{1/2} \leftrightarrow 5s^26s\ ^2\mathbf{S}_{1/2}$
Wavelength	398.91134856(4) nm [173]	410.296 nm [174]
	398.910990(45) nm [175]	
Exc. state lifetime	5.464(5) ns [176]	7.4(3) ns[177]
⇒ linewidth	$2\pi \times 29.13(3)$ MHz	$2\pi \times 21.5(9)$ MHz

For the ytterbium “single color” scheme, see [178]

Acronyms

AOM acousto-optic modulator

BBR black-body radiation

BSB blue sideband transition

CIC clock-induced charges

COM center of mass

CTE coefficient of thermal expansion

ECDL external-cavity diode laser

EMCCD electron-multiplying CCD

EMM excess micromotion

EOM electro-optic modulator

FEM finite-element method

FPGA field-programmable gate array

FS fused silica

FWHM full width at half-maximum

IMM intrinsic micromotion

LO local oscillator

MCA multi-channel analyzer

NA numerical aperture

NIST National Institute of Standards and Technology, national metrology institute of the United States

NPL National Physical Laboratory, national metrology institute of the UK

PDH Pound-Drever-Hall [109]

PMT photomultiplier tube

PSD power spectral density

PTB Physikalisch-Technische Bundesanstalt, national metrology institute of Germany

QPN quantum projection noise

rf radio-frequency

rms root mean square

ROI region of interest

RSB red sideband transition

SBC sideband cooling

SHG second-harmonic generation

SNR signal-to-noise ratio

TAC time-to-amplitude converter

Bibliography

[1] J. C. Maxwell, *The scientific papers of James Clerk Maxwell*, ed. by W. D. Niven, vol. II, Cambridge University Press, 1890 (cit. on p. 1).

[2] L. Essen and J. V. L. Parry, “An Atomic Standard of Frequency and Time Interval: A Cæsium Resonator”, *Nature* **176**, 280–282 (1955) (cit. on p. 1).

[3] T. W. Hänsch and A. L. Schawlow, “Cooling of gases by laser radiation”, *Opt. Commun.* **13**, 68 (1975) (cit. on p. 1).

[4] D. J. Wineland, R. E. Drullinger, and F. L. Walls, “Radiation-Pressure Cooling of Bound Resonant Absorbers”, *Phys. Rev. Lett.* **40**, 1639–1642 (1978) (cit. on p. 1).

[5] W. Neuhauser et al., “Visual observation and optical cooling of electrodynamically contained ions”, *Appl. Phys.* **17**, 123–129 (1978) (cit. on p. 1).

[6] M. A. Kasevich et al., “RF spectroscopy in an atomic fountain”, *Phys. Rev. Lett.* **63**, 612–615 (1989) (cit. on p. 1).

[7] A. Clairon et al., “Ramsey resonance in a Zacharias fountain”, *Europhys. Lett.* **16**, 165 (1991) (cit. on p. 1).

[8] V. A. Dzuba and V. V. Flambaum, “Atomic optical clocks and search for variation of the fine-structure constant”, *Phys. Rev. A* **61**, 034502 (2000) (cit. on p. 1).

[9] T. Rosenband et al., “Frequency Ratio of Al^+ and Hg^+ Single-Ion Optical Clocks; Metrology at the 17th Decimal Place”, *Science* **319**, 1808– (2008) (cit. on p. 1).

[10] N. Huntemann et al., “Improved Limit on a Temporal Variation of $\mathrm{m}_p/\mathrm{m}_e$ from Comparisons of Yb^+ and Cs Atomic Clocks”, *Phys. Rev. Lett.* **113**, 210802 (2014) (cit. on p. 1).

[11] R. M. Godun et al., “Frequency Ratio of Two Optical Clock Transitions in $^{171}\mathrm{Yb}^+$ and Constraints on the Time Variation of Fundamental Constants”, *Phys. Rev. Lett.* **113**, 210801 (2014) (cit. on p. 1).

[12] B. C. Young et al., “Visible Lasers with Subhertz Linewidths”, *Phys. Rev. Lett.* **82**, 3799–3802 (1999) (cit. on pp. 1, 33).

[13] T. Udem, R. Holzwarth, and T. W. Hänsch, “Optical frequency metrology”, *Nature* **416**, 233–237 (2002) (cit. on pp. 1, 5).

[14] A. A. Madej et al., "^{88}Sr^{+} 445-THz Single-Ion Reference at the 10^{-17} Level via Control and Cancellation of Systematic Uncertainties and Its Measurement against the SI Second", *Phys. Rev. Lett.* **109**, 203002 (2012) (cit. on pp. 1, 5, 72).

[15] N. Huntemann et al., "High-Accuracy Optical Clock Based on the Octupole Transition in ^{171}Yb^{+}", *Phys. Rev. Lett.* **108**, 090801 (2012) (cit. on pp. 1, 53, 57, 71).

[16] R. Le Targat et al., "Experimental realization of an optical second with strontium lattice clocks", *Nat. Commun.* **4**, 2109 (2013) (cit. on p. 1).

[17] S. Falke et al., "A strontium lattice clock with 3×10^{-17} inaccuracy and its frequency", *New J. Phys.* **16**, 073023 (2014) (cit. on p. 1).

[18] K. Yamanaka et al., "Frequency Ratio of ^{199}Hg and ^{87}Sr Optical Lattice Clocks beyond the SI Limit", *Phys. Rev. Lett.* **114**, 230801 (2015) (cit. on p. 1).

[19] P. Gill, "When should we change the definition of the second?", *Phil. Trans. R. Soc. A* **369**, 4109–4130 (2011) (cit. on p. 1).

[20] F. Riehle, "Towards a redefinition of the second based on optical atomic clocks", *C. R. Phys.* **5**, 506–515 (2015) (cit. on p. 1).

[21] C. W. Chou et al., "Optical Clocks and Relativity", *Science* **329**, 1630 (2010) (cit. on p. 1).

[22] G. Xu, ed., *Sciences of Geodesy II - Innovations and Future Developments*, Springer-Verlag, Heidelberg, 2013 (cit. on p. 1).

[23] A. Bjerhammar, "On a relativistic geodesy", *B. Geod.* **59**, 207–220 (1985) (cit. on p. 2).

[24] `http://geoq.uni-hannover.de` (cit. on p. 2).

[25] W. Paul, H. P. Reinhard, and U. von Zahn, "Das elektrische Massenfilter als Massenspektrometer und Isotopentrenner", *Z. Phys.* **152**, 143–182 (1958) (cit. on pp. 2, 10).

[26] W. Paul, "Electromagnetic traps for charged and neutral particles", *Rev. Mod. Phys.* **62**, 531–540 (1990) (cit. on pp. 2, 10).

[27] C. Champenois et al., "Ion ring in a linear multipole trap for optical frequency metrology", *Phys. Rev. A* **81**, 043410 (2010) (cit. on p. 2).

[28] N. Herschbach et al., "Linear Paul trap design for an optical clock with Coulomb crystals", *Appl. Phys. B* **107**, 891–906 (2012) (cit. on pp. 2, 3, 6, 23, 96, 101, 103).

[29] M. S. Safronova, M. G. Kozlov, and C. W. Clark, "Precision Calculation of Blackbody Radiation Shifts for Optical Frequency Metrology", *Phys. Rev. Lett.* **107**, 143006 (2011) (cit. on pp. 2, 6, 72, 103).

[30] T. Becker et al., "High-resolution spectroscopy of a single In^{+} ion: Progress towards an optical frequency standard", *Phys. Rev. A* **63**, 051802 (2001) (cit. on pp. 2, 6).

[31] M. Brownnutt et al., "Ion-trap measurements of electric field noise near surfaces", arXiv:1409.6572 (2014) (cit. on pp. 3, 68).

[32] D. J. Berkeland et al., "Minimization of ion micromotion in a Paul trap", *J. Appl. Phys.* **83**, 5025–5033 (1998) (cit. on pp. 3, 12, 72, 79, 81, 82, 102).

[33] K. Pyka, "High-precision ion trap for spectroscopy of Coulomb crystals", PhD thesis, Leibniz-Universität Hannover, 2013 (cit. on pp. 3, 23, 29, 97, 101).

[34] K. Pyka et al., "A high-precision segmented Paul trap with minimized micromotion for an optical multiple-ion clock", *Appl. Phys. B* **114**, 231–241 (2014) (cit. on pp. 3, 23, 29, 101).

[35] N. Huntemann, "High-Accuracy Optical Clock Based on the Octupole Transition in $^{171}\mathrm{Yb}^{+}$", PhD thesis, Leibniz-Universität Hannover, 2014 (cit. on pp. 5, 57, 103, 104).

[36] C. W. Chou et al., "Frequency Comparison of Two High-Accuracy Al^{+} Optical Clocks", *Phys. Rev. Lett.* **104**, 070802 (2010) (cit. on pp. 5, 71, 104).

[37] D. J. Wineland et al., "Quantum Computers and Atomic Clocks", *Frequency Standards and Metrology*, ed. by P. Gill, 2002, pp. 361–368 (cit. on p. 6).

[38] N. Yu, H. Dehmelt, and W. Nagourney, "The $3^1\mathrm{S}_0 - 3^3\mathrm{P}_0$ Transition in the Aluminum Isotope Ion $^{26}\mathrm{A1}^{+}$: A Potentially Superior Passive Laser Frequency Standard and Spectrum Analyzer", *Proc. Natl. Acad. Sci. U.S.A.* **89**, 7289 (1992) (cit. on p. 6).

[39] E. Peik, G. Hollemann, and H. Walther, "Laser cooling and quantum jumps of a single indium ion", *Phys. Rev. A* **49**, 402–408 (1994) (cit. on p. 6).

[40] H. G. Dehmelt, "Mono-ion oscillator as potential ultimate laser frequency standard.", *IEEE Trans. Instrum. Meas.* **31**, 83–87 (1982) (cit. on p. 6).

[41] R. H. Garstang, "Hyperfine structure and intercombination line intensities in the spectra of magnesium, zinc, cadmium and mercury", *J. Opt. Soc. Am.* **52**, 845 (1962) (cit. on p. 6).

[42] E. Peik, "Laserspektroskopie an gespeicherten Indium-Ionen", PhD thesis, Max-Planck-Institut für Quantenoptik, 1993 (cit. on p. 6).

[43] P. O. Schmidt et al., "Spectroscopy Using Quantum Logic", *Science* **309**, 749–752 (2005) (cit. on p. 6).

[44] D. B. Hume et al., "Trapped-Ion State Detection through Coherent Motion", *Phys. Rev. Lett.* **107**, 243902 (2011) (cit. on p. 6).

[45] M. Schulte et al., "Quantum Algorithmic Readout in Multi-Ion Clocks", arXiv:1501.06453 (2015) (cit. on pp. 6, 104).

[46] K. Wakui, K. Hayasaka, and T. Ido, "Generation of vacuum ultraviolet radiation by intracavity high-harmonic generation toward state detection of single trapped ions", *Appl. Phys. B* **117**, 957 (2014) (cit. on p. 6).

[47] J. B. Wübbena et al., "Sympathetic cooling of mixed-species two-ion crystals for precision spectroscopy", *Phys. Rev. A* **85**, 043412 (2012) (cit. on pp. 7, 20, 24, 65).

[48] C. Champenois et al., "Evaluation of the ultimate performances of a Ca^+ single-ion frequency standard", *Phys. Lett. A* **331**, 298–311 (2004) (cit. on p. 7).

[49] E. Riis and A. G. Sinclair, "Optimum measurement strategies for trapped ion optical frequency standards", *J. Phys. B* **37**, 4719–4732 (2004) (cit. on p. 7).

[50] E. Peik, T. Schneider, and C. Tamm, "Laser frequency stabilization to a single ion", *J. Phys. B* **39**, 145–158 (2006) (cit. on pp. 7, 8, 52).

[51] N. F. Ramsey, "A Molecular Beam Resonance Method with Separated Oscillating Fields", *Phys. Rev.* **78**, 695–699 (1950) (cit. on p. 7).

[52] W. Nagourney, J. Sandberg, and H. Dehmelt, "Shelved optical electron amplifier - Observation of quantum jumps", *Phys. Rev. Lett.* **56**, 2797–2799 (1986) (cit. on p. 7).

[53] W. M. Itano et al., "Quantum projection noise: Population fluctuations in two-level systems", *Phys. Rev. A* **47**, 3554–3570 (1993) (cit. on p. 8).

[54] V. Giovannetti, S. Lloyd, and L. Maccone, "Quantum Metrology", *Phys. Rev. Lett.* **96**, 010401 (2006) (cit. on p. 9).

[55] S. F. Huelga et al., "Improvement of Frequency Standards with Quantum Entanglement", *Phys. Rev. Lett.* **79**, 3865–3868 (1997) (cit. on p. 9).

[56] A. André, A. S. Sørensen, and M. D. Lukin, "Stability of Atomic Clocks Based on Entangled Atoms", *Phys. Rev. Lett.* **92**, 230801 (2004) (cit. on pp. 10, 104).

[57] I. D. Leroux, M. H. Schleier-Smith, and V. Vuletić, "Orientation-Dependent Entanglement Lifetime in a Squeezed Atomic Clock", *Phys. Rev. Lett.* **104**, 250801 (2010) (cit. on pp. 10, 104).

[58] T. Rosenband and D. R. Leibrandt, "Exponential scaling of clock stability with atom number", arXiv:1303.6357 (2013) (cit. on pp. 10, 104).

[59] J. Borregaard and A. S. Sørensen, "Efficient Atomic Clocks Operated with Several Atomic Ensembles", *Phys. Rev. Lett.* **111**, 090802 (2013) (cit. on pp. 10, 104).

[60] S. Earnshaw, "On the Nature of the Molecular Forces which Regulate the Constitution of the Luminiferous Ether", *Transactions of the Cambridge Philosophical Society* **7**, 97 (1848) (cit. on p. 10).

[61] F. G. Major, V. N. Gheorge, and G. Werth, *Charged Particle Traps*, Springer-Verlag, Heidelberg, 2005 (cit. on p. 11).

[62] D. Leibfried et al., "Quantum dynamics of single trapped ions", *Rev. Mod. Phys.* **75**, 281–324 (2003) (cit. on pp. 12, 14, 76).

[63] G. Morigi and H. Walther, "Two-species Coulomb chains for quantum information", *European Physical Journal D* **13**, 261–269 (2001) (cit. on pp. 12, 16).

[64] D. F. V. James, “Quantum dynamics of cold trapped ions with application to quantum computation”, *Appl. Phys. B* **66**, 181–190 (1998) (cit. on pp. 12, 54).

[65] D. Kielpinski et al., “Sympathetic cooling of trapped ions for quantum logic”, *Phys. Rev. A* **61**, 032310 (2000) (cit. on p. 12).

[66] H. Landa et al., “Modes of oscillation in radiofrequency Paul traps”, *New J. Phys.* **14**, 093023 (2012) (cit. on p. 12).

[67] A. Steane, “The ion trap quantum information processor”, *Appl. Phys. B* **64**, 623–643 (1996) (cit. on pp. 12, 96).

[68] D. J. Wineland and W. M. Itano, “Laser cooling of atoms”, *Phys. Rev. A* **20**, 1521–1540 (1979) (cit. on pp. 14, 15, 90).

[69] D. J. Wineland et al., “Experimental issues in coherent quantum-state manipulation of trapped atomic ions”, *J. Res. Natl. Inst. Stand. Technol.* **103**, 259 (1998) (cit. on pp. 14, 17).

[70] R. H. Dicke, “The Effect of Collisions upon the Doppler Width of Spectral Lines”, *Phys. Rev.* **89**, 472–473 (1953) (cit. on p. 16).

[71] I. Lizuain, J. G. Muga, and J. Eschner, “Motional frequency shifts of trapped ions in the Lamb-Dicke regime”, *Phys. Rev. A* **76**, 033808 (2007) (cit. on p. 16).

[72] H. J. Lipkin, *Quantum mechanics*, North-Holland Publishing, Amsterdam, 1973 (cit. on p. 17).

[73] C. F. Roos, “Controlling the quantum state of trapped ions”, PhD thesis, Leopold-Franzens-Universität Innsbruck, 2000 (cit. on pp. 17, 31, 54).

[74] A. D. Ludlow et al., “Optical Atomic Clocks”, *Rev. Mod. Phys* **87**, 637 (2015) (cit. on p. 17).

[75] R. Loudon, *The Quantum Theory of Light*, Oxford University Press, 1983 (cit. on p. 18).

[76] Q. A. Turchette et al., “Heating of trapped ions from the quantum ground state”, *Phys. Rev. A* **61**, 063418 (2000) (cit. on pp. 18, 68).

[77] K. Hayasaka, “Synthesis of two-species ion chains for a new optical frequency standard with an indium ion”, *Appl. Phys. B* **107**, 965–970 (2012) (cit. on p. 20).

[78] W. W. Macalpine and R. O. Schildknecht, “Coaxial Resonators with Helical Inner Conductor”, *Proceedings of the IRE* **47**, 2099–2105 (1959), ISSN: 0096-8390 (cit. on p. 23).

[79] E. Biémont et al., “Lifetime calculations in Yb II”, *J. Phys. B* **31**, 3321–3333 (1998) (cit. on pp. 24, 107).

[80] M. M. Schauer et al., “Collisional population transfer in trapped Yb$^+$ ions”, *Phys. Rev. A* **79**, 062705 (2009) (cit. on p. 24).

[81] N. Yu and L. Maleki, “Lifetime measurements of the $4f^{14}5d$ metastable states in single ytterbium ions”, *Phys. Rev. A* **61**, 022507 (2000) (cit. on pp. 24, 107).

[82] W. F. Meggers, “The second spectrum of Ytterbium (Yb II)”, *J. Res. Nat. Bureau Stand. A* **71A**, 396 (1967) (cit. on pp. 29, 107).

[83] M. Hirsch et al., “A Stochastic Model for Electron Multiplication Charge-Coupled Devices From Theory to Practice”, *PLoS ONE* **8**, e53671 (2013) (cit. on pp. 30, 31).

[84] R. N. Tubbs, “Lucky Exposures: Diffraction limited astronomical Imaging through the Atmosphere”, PhD thesis, Cambridge University, 2003 (cit. on p. 31).

[85] J. Keller et al., “Simple vibration insensitive cavity for laser stabilization at the 10^{-16} level”, *Appl. Phys. B* **116**, 203–210 (2014) (cit. on p. 33).

[86] H. B. Callen and T. A. Welton, “Irreversibility and Generalized Noise”, *Phys. Rev.* **83**, 34–40 (1951) (cit. on p. 34).

[87] Y. Levin, “Internal thermal noise in the LIGO test masses: A direct approach”, *Phys. Rev. D* **57**, 659–663 (1998) (cit. on p. 34).

[88] D. W. Allan, “Statistics of atomic frequency standards”, *P. IEEE* **54** (1966) (cit. on pp. 34, 36).

[89] F. Riehle, *Frequency Standards - Basics and Applications*, Wiley-VCH, Weinheim, 2004 (cit. on pp. 34, 79).

[90] J. Millo et al., “Ultrastable lasers based on vibration insensitive cavities”, *Phys. Rev. A* **79**, 053829 (2009) (cit. on p. 34).

[91] S. T. Dawkins et al., “An ultra-stable referenced interrogation system in the deep ultraviolet for a mercury optical lattice clock”, *Appl. Phys. B* **99**, 41–46 (2010) (cit. on p. 34).

[92] T. Kessler et al., “A sub-40-mHz-linewidth laser based on a silicon single-crystal optical cavity”, *Nat. Photonics* **6**, 687–692 (2012) (cit. on pp. 34, 44).

[93] E. D’Ambrosio, “Nonspherical mirrors to reduce thermoelastic noise in advanced gravitational wave interferometers”, *Phys. Rev. D* **67**, 102004 (2003) (cit. on p. 34).

[94] B. Mours, E. Tournefier, and J.-Y. Vinet, “Thermal noise reduction in interferometric gravitational wave antennas: using high order TEM modes”, *Classical Quant. Grav.* **23**, 5777–5784 (2006) (cit. on p. 34).

[95] S. Amairi et al., “Reducing the effect of thermal noise in optical cavities”, *Appl. Phys. B* **113**, 233–242 (2013) (cit. on p. 34).

[96] Y. Y. Jiang et al., “Making optical atomic clocks more stable with 10^{-16}-level laser stabilization”, *Nat. Photonics* **5**, 158 (2011) (cit. on p. 34).

[97] T. L. Nicholson et al., “Comparison of Two Independent Sr Optical Clocks with $1{\times}10^{-17}$ Stability at 10^3s”, *Phys. Rev. Lett.* **109**, 230801 (2012) (cit. on p. 34).

[98] S. Häfner et al., "8×10^{-17} fractional laser frequency instability with a long room-temperature cavity", *Opt. Lett.* **40**, 2112–2115 (2015) (cit. on pp. 34, 50).

[99] K. Numata, A. Kemery, and J. Camp, "Thermal-Noise Limit in the Frequency Stabilization of Lasers with Rigid Cavities", *Phys. Rev. Lett.* **93**, 250602 (2004) (cit. on pp. 34, 35).

[100] T. Kessler, T. Legero, and U. Sterr, "Thermal noise in optical cavities revisited", *J. Opt. Soc. Am. B* **29**, 178 (2012) (cit. on p. 34).

[101] S. D. Penn et al., "Mechanical loss in tantala/silica dielectric mirror coatings", *Classical Quant. Grav.* **20**, 2917–2928 (2003) (cit. on p. 34).

[102] A. E. Villar et al., "Measurement of thermal noise in multilayer coatings with optimized layer thickness", *Phys. Rev. D* **81**, 122001 (2010) (cit. on p. 35).

[103] G. M. Harry et al., "Titania-doped tantala/silica coatings for gravitational-wave detection", *Classical Quant. Grav.* **24**, 405–415 (2007) (cit. on p. 35).

[104] G. D. Cole et al., "Tenfold reduction of Brownian noise in high-reflectivity optical coatings", *Nat. Photonics* **7**, 644 (2013) (cit. on pp. 35, 52).

[105] F. Brückner et al., "Monolithic dielectric surfaces as new low-loss light-matter interfaces", *Opt. Lett.* **33**, 264 (2008) (cit. on p. 35).

[106] Corning Inc., *ULE® Corning Code 7973 data sheet* (cit. on pp. 35, 39).

[107] T. Legero, T. Kessler, and U. Sterr, "Tuning the thermal expansion properties of optical reference cavities with fused silica mirrors", *J. Opt. Soc. Am. B* **27**, 914 (2010) (cit. on pp. 39, 40).

[108] P. Dubé et al., "A narrow linewidth and frequency-stable probe laser source for the $^{88}\mathrm{Sr}^{+}$ single ion optical frequency standard", *Appl. Phys. B* **95**, 43–54 (2009) (cit. on p. 41).

[109] R. W. P. Drever et al., "Laser phase and frequency stabilization using an optical resonator", *Appl. Phys. B* **31**, 97–105 (1983) (cit. on pp. 43, 112).

[110] Y. N. Zhao et al., "Sub-Hertz frequency stabilization of a commercial diode laser", *Opt. Commun.* **283**, 4696 –4700 (2010) (cit. on p. 43).

[111] A. L. Schawlow and C. H. Townes, "Infrared and Optical Masers", *Phys. Rev.* **112**, 1940–1949 (1958) (cit. on p. 43).

[112] L.-S. Ma et al., "Delivering the same optical frequency at two places: accurate cancellation of phase noise introduced by an optical fiber or other time-varying path", *Opt. Lett.* **19**, 1777–1779 (1994) (cit. on p. 44).

[113] J. E. Gray and D. W. Allan, *Proc. 28th Frequency Control Symposium* , 243 (1974) (cit. on p. 44).

[114] H. R. Telle, B. Lipphardt, and J. Stenger, “Kerr-lens, mode-locked lasers as transfer oscillators for optical frequency measurements”, *Appl. Phys. B* **74**, 1–6 (2002) (cit. on p. 44).

[115] D. W. Allan and J. Barnes, “A modified ’Allan variance’ with increased oscillator characterization ability”, *Proceedings of the 35th Ann. Freq. Control Symposium*, 1981, pp. 470–475 (cit. on p. 44).

[116] D.-M. Meier, “Ein Lasersystem zur Seitenbandspektroskopie an gemischten In^+/Yb^+-Kristallen”, MA thesis, Technische Universität Braunschweig, 2012 (cit. on p. 44).

[117] M. Zhu and J. L. Hall, “Stabilization of optical phase/frequency of a laser system: application to a commercial dye laser with an external stabilizer”, *J. Opt. Soc. Am. B* **10**, 802–816 (1993) (cit. on p. 45).

[118] A. Godone and F. Levi, “About the radiofrequency spectrum of a phase noise modulated carrier”, *Proceedings of the 12th European Frequency and Time Forum* , 392 (1998) (cit. on pp. 45, 46).

[119] T. Nazarova, “Towards the Quantum Noise Limit in Ramsey-Bordé Atom Interferometry”, PhD thesis, Leibniz-Universität Hannover, 2007 (cit. on p. 46).

[120] M. Roberts et al., “Observation of an Electric Octupole Transition in a Single Ion”, *Phys. Rev. Lett.* **78**, 1876–1879 (1997) (cit. on pp. 53, 62, 107).

[121] P. Taylor, “Observation of an Ultra-High Q Resonance in a Single Ion of $^{172}Yb^+$”, PhD thesis, University of Oxford, 1996 (cit. on pp. 53, 62).

[122] P. Taylor et al., “Investigation of the $^2S_{1/2}$-$^2D_{5/2}$ clock transition in a single ytterbium ion”, *Phys. Rev. A* **56**, 2699–2704 (1997) (cit. on pp. 53, 57, 107).

[123] M. Roberts, “Spectroscopy of a Single Ytterbium Ion”, PhD thesis, Imperial College, University of London, 1997 (cit. on pp. 53, 57).

[124] C. Tamm, D. Engelke, and V. Bühner, “Spectroscopy of the electric-quadrupole transition $^2S_{1/2}(F=0)$-$^2D_{3/2}(F=2)$ in trapped $^{171}Yb^+$”, *Phys. Rev. A* **61**, 053405 (2000) (cit. on p. 53).

[125] I. Sherstov et al., “Diode-laser system for high-resolution spectroscopy of the $^2S_{1/2}\rightarrow{}^2F_{7/2}$ octupole transition in $^{171}Yb^+$”, *Phys. Rev. A* **81**, 021805 (2010) (cit. on p. 57).

[126] F. Diedrich et al., “Laser cooling to the zero-point energy of motion”, *Phys. Rev. Lett.* **62**, 403–406 (1989) (cit. on p. 65).

[127] I. Marzoli et al., “Laser cooling of trapped three-level ions: designing two-level systems for sideband cooling”, *Phys. Rev. A* **49**, 2771–2779 (1994) (cit. on p. 66).

[128] L. Deslauriers et al., “Scaling and Suppression of Anomalous Heating in Ion Traps”, *Phys. Rev. Lett.* **97**, 103007 (2006) (cit. on p. 68).

[129] J. Labaziewicz et al., “Temperature Dependence of Electric Field Noise above Gold Surfaces”, *Phys. Rev. Lett.* **101**, 180602 (2008) (cit. on p. 68).

[130] D. T. C. Allcock et al., “Reduction of heating rate in a microfabricated ion trap by pulsed-laser cleaning”, *New J. Phys.* **13**, 123023 (2011) (cit. on p. 68).

[131] D. A. Hite et al., “100-Fold Reduction of Electric-Field Noise in an Ion Trap Cleaned with In Situ Argon-Ion-Beam Bombardment”, *Phys. Rev. Lett.* **109**, 103001 (2012) (cit. on p. 68).

[132] J. Keller et al., “Precise determination of micromotion for trapped-ion optical clocks”, *J. Appl. Phys.* **118**, 104501 (2015) (cit. on p. 71).

[133] P. Dubé et al., “High-Accuracy Measurement of the Differential Scalar Polarizability of a $^{88}\mathrm{Sr}^{+}$ Clock Using the Time-Dilation Effect”, *Phys. Rev. Lett.* **112**, 173002 (2014) (cit. on p. 72).

[134] C. Lisowski et al., “Dark resonances as a probe for the motional state of a single ion”, *Appl. Phys. B* **81**, 5–12 (2005) (cit. on p. 72).

[135] K. R. Brown et al., “Loading and characterization of a printed-circuit-board atomic ion trap”, *Phys. Rev. A* **75**, 015401 (2007) (cit. on p. 72).

[136] D. T. C. Allcock et al., “Implementation of a symmetric surface-electrode ion trap with field compensation using a modulated Raman effect”, *New J. Phys.* **12**, 053026 (2010) (cit. on p. 72).

[137] T. A. Peppers et al., “Fixation of humeral prostheses and axial micromotion”, *J. Shoulder Elbow Surg.* **7**, 414 (1998) (cit. on p. 72).

[138] Y. Ibaraki, U. Tanaka, and S. Urabe, “Detection of parametric resonance of trapped ions for micromotion compensation”, *Appl. Phys. B* **105**, 219–223 (2011) (cit. on pp. 72, 89).

[139] B. L. Chuah et al., “Detection of ion micromotion in a linear Paul trap with a high finesse cavity”, *Opt. Express* **21**, 10632 (2013) (cit. on p. 72).

[140] A. Härter et al., “Minimization of ion micromotion using ultracold atomic probes”, *Appl. Phys. Lett.* **102**, 221115 (2013) (cit. on p. 72).

[141] T. F. Gloger et al., “Ion trajectory analysis for micromotion minimization and the measurement of small forces”, *Phys. Rev. A* **92**, 043421 (2015) (cit. on p. 72).

[142] E. Peik et al., “Sideband cooling of ions in radio-frequency traps”, *Phys. Rev. A* **60**, 439–449 (1999) (cit. on p. 73).

[143] F. Diedrich and H. Walther, “Nonclassical radiation of a single stored ion”, *Phys. Rev. Lett.* **58**, 203–206 (1987) (cit. on p. 79).

[144] J. T. Höffges et al., “Heterodyne measurement of the fluorescent radiation of a single trapped ion”, *Opt. Commun.* **133**, 170–174 (1997) (cit. on p. 79).

[145] G. C. Bjorklund, “Frequency-modulation spectroscopy: a new method for measuring weak absorptions and dispersions”, *Opt. Lett.* **5**, 15–17 (1980) (cit. on p. 80).

[146] T. Pruttivarasin, M. Ramm, and H. Häffner, “Direct spectroscopy of the $^2S_{1/2}$ - $^2P_{1/2}$ and $^2D_{3/2}$ - $^2P_{1/2}$ transitions and observation of micromotion modulated spectra in trapped $^{40}Ca^+$”, *J. Phys. B* **47**, 135002 (2014) (cit. on p. 82).

[147] J. R. Johansson, P. D. Nation, and F. Nori, “QuTiP 2: A Python framework for the dynamics of open quantum systems”, *Comput. Phys. Commun.* **184**, 1234 –1240 (2013) (cit. on p. 83).

[148] S. Narayanan et al., “Electric field compensation and sensing with a single ion in a planar trap”, *J. Appl. Phys.* **110**, 114909 (2011) (cit. on p. 89).

[149] U. Tanaka et al., “Micromotion compensation in a surface electrode trap by parametric excitation of trapped ions”, *Appl. Phys. B* **107**, 907–912 (2012) (cit. on p. 89).

[150] T. A. Savard, K. M. O’hara, and J. E. Thomas, “Laser-noise-induced heating in far-off resonance optical traps”, *Phys. Rev. A* **56**, 1095 (1997) (cit. on p. 90).

[151] G. P. Barwood et al., “Frequency noise processes in a strontium ion optical clock”, *J. Phys. B* **48**, 035401 (2015) (cit. on p. 92).

[152] R. B. Linnet, “Probing and controlling ion Coulomb crystals by optical cavity fields”, PhD thesis, Aarhus University, 2014 (cit. on p. 93).

[153] M. Doležal et al., “Analysis of thermal radiation in ion traps for optical frequency standards”, *Metrologia* **52**, 842 (2015) (cit. on pp. 102, 103).

[154] T. Rosenband et al., “Blackbody radiation shift of the $^{27}Al^+$ $^1S_0$ - $^3P_0$ transition”, *Proceedings of the 20th European Time and Frequency Forum* , 289–291 (2006) (cit. on p. 103).

[155] K Pyka, J. Keller et al., “Topological defect formation and spontaneous symmetry breaking in ion Coulomb crystals”, *Nat. Commun.* **4**, 2291 (2013) (cit. on p. 104).

[156] H. L. Partner et al., “Dynamics of topological defects in ion Coulomb crystals”, *New J. Phys.* **15**, 103013 (2013) (cit. on p. 104).

[157] H. L. Partner et al., “Structural phase transitions and topological defects in ion Coulomb crystals”, *Physica B* **460**, 114–118 (2015) (cit. on p. 104).

[158] S. Fishman et al., “Structural phase transitions in low-dimensional ion crystals”, *Phys. Rev. B* **77**, 064111 (2008) (cit. on p. 104).

[159] H. Landa et al., “Quantum Coherence of Discrete Kink Solitons in Ion Traps”, *Phys. Rev. Lett.* **104**, 043004 (2010) (cit. on p. 105).

[160] M. Mielenz et al., “Trapping of Topological-Structural Defects in Coulomb Crystals”, *Phys. Rev. Lett.* **110**, 133004 (2013) (cit. on p. 105).

[161] H. Landa et al., “Entanglement Generation Using Discrete Solitons in Coulomb Crystals”, *Physs Rev. Lett.* **113**, 053001 (2014) (cit. on p. 105).

[162] A. Bermudez, M. Bruderer, and M. B. Plenio, “Controlling and Measuring Quantum Transport of Heat in Trapped-Ion Crystals”, *Phys. Rev. Lett.* **111**, 040601 (2013) (cit. on p. 105).

[163] M. Ramm, T. Pruttivarasin, and H. Häffner, “Energy transport in trapped ion chains”, *New J. Phys.* **16**, 063062 (2014) (cit. on p. 105).

[164] J. Roßnagel et al., “Fast thermometry for trapped ions using dark resonances”, *New J. Phys.* **17**, 045004 (2015) (cit. on p. 105).

[165] K. G. Johnson et al., “Sensing Atomic Motion from the Zero Point to Room Temperature with Ultrafast Atom Interferometry”, *Phys. Rev. Lett.* **115**, 213001 (2015) (cit. on p. 105).

[166] B. C. Fawcett and M. Wilson, “Computed Oscillator Strengths, and Landé g-Values, and Lifetimes in Yb II”, *At. Data Nucl. Data Tables* **47**, 241 (1991) (cit. on p. 107).

[167] C. Gerz et al., “Lifetime and collisional depopulation of the metastable 5 D $_{3/2}$-state of Yb^{+}”, *Z. Phys. D* **8**, 235–237 (1988) (cit. on p. 107).

[168] S. Olmschenk et al., “Measurement of the lifetime of the 6pP2$_{1/2}{}^{o}$ level of Yb^{+}”, *Phys. Rev. A* **80**, 022502 (2009) (cit. on p. 107).

[169] E. H. Pinnington, G. Rieger, and J. A. Kernahan, “Beam-laser measurements of the lifetimes of the 6p levels in Yb II”, *Phys. Rev. A* **56**, 2421–2423 (1997) (cit. on p. 107).

[170] R. W. Berends et al., “Beam-laser lifetime measurements for four resonance levels of Yb II”, *J. Phys. B* **26**, L701–L704 (1993) (cit. on p. 107).

[171] M. Aymar et al., “Three-step laser spectroscopy and multichannel quantum defect analysis of odd-parity Rydberg states of neutral ytterbium”, *J. Phys. B* **17**, 3645–3661 (1984) (cit. on p. 109).

[172] D. C. Morton, “Atomic Data for Resonance Absorption Lines. II. Wavelengths Longward of the Lyman Limit for Heavy Elements”, *Astrophys. J. Suppl. Ser.* **130**, 403–436 (2000) (cit. on p. 109).

[173] D. Das et al., “Absolute frequency measurements in Yb with 0.08 ppb uncertainty: Isotope shifts and hyperfine structure in the 399-nm $^{1}S_{0} \rightarrow {}^{1}P_{1}$ line”, *Phys. Rev. A* **72**, 032506 (2005) (cit. on p. 109).

[174] K. Wagatsuma, “Classification of emission lines of the Group IIIB elements, aluminium, gallium and indium, excited by Grimm glow discharge plasmas using several different plasma gases”, *J. Anal. At. Spectrom.* **11**, 957–966 (1996) (cit. on p. 109).

[175] A. H. Nizamani, J. J. McLoughlin, and W. K. Hensinger, “Doppler-free Yb spectroscopy with the fluorescence spot technique”, *Phys. Rev. A* **82**, 043408 (2010) (cit. on p. 109).

[176] Y. Takasu et al., “Photoassociation Spectroscopy of Laser-Cooled Ytterbium Atoms”, *Phys. Rev. Lett.* **93**, 123202 (2004) (cit. on p. 109).

[177] M. D. Havey, L. C. Balling, and J. J. Wright, “Measurement of the lowest S-state lifetime of Al, Ga, In, and Tl.”, *J. Opt. Soc. Am.* **67**, 491–493 (1977) (cit. on p. 109).

[178] M. Johanning et al., “Resonance-enhanced isotope-selective photoionization of YbI for ion trap loading”, *Appl. Phys. B* **103**, 327–338 (2011) (cit. on p. 109).

Acknowledgments

Many people deserve thanks for their support during the time of this work. First I would like to thank Dr. Tanja Mehlstäubler for giving me the chance to work on this interesting project and for regular advice and discussions. I would also like to thank Prof. Piet Schmidt and PD Dr. Ekkehard Peik for their support and a very pleasant atmosphere at the QUEST institute and in the time and frequency department. Many thanks to Prof. Klemens Hammerer for agreeing to chair the PhD defense and to Prof. Kilian Singer for providing an external referee report on this thesis.

None of this would have been possible without the work of several colleagues in the lab. Norbert Herschbach and Karsten Pyka, thanks for starting this setup from an empty room and for many enjoyable hours in the lab and at the pool table. Heather Partner, thanks for all your help and for the great optimistic atmosphere. And of course thanks for initiating and enforcing many traditions such as the regular Schadt's. Tobias Burgermeister, it was always a pleasure to work with you. Dimitri Kalincev and Jan Kiethe, I enjoyed the few months of overlap we had at the experiment and I'm convinced that you will put this machine to good use.

Over the years, several students, interns and FWJlers helped us out. I'd like to thank David Meier and Kristijan Kuhlmann for their contributions and for keeping the sneak peek tradition alive. Keshav Thirumalai, Michael Moody, Yong Lu, Henrik Wingerath, thanks for all your help. Rohit Swarnkar, besides the contributions to the setup, thanks for introducing me to poha and hing. To the FWJlers Daniel Pflüger, Jan-Wilke Henke, Ida Sigusch, Achim Byl, Leander Thiessen, thanks for helping out in the lab and, in one case, starting a robin craze that far outlived your stay at PTB.

I'd like to thank our neighbors at the Th^+ project. Maksim Okhapkin, thanks for everything you taught me about laser stabilization and for happily sharing equipment on the (very few) occasions I asked for it. Andrey Herrera, thanks for infecting me with your road bike addiction and chasing me over mountains at insane hours in the morning.

Thanks to Thomas Legero for optically contacting the mirrors onto the 30 cm spacer and to Christian Grebing, who was in charge of the frequency comb during the three-cornered hat measurements.

We had several productive collaborations with guests in the past years. I would like to thank Stepan Ignatovich, Ramil Nigmatullin, Lin E, and Stephen Webster for their contributions to our work and the things I learned from them. I enjoyed working with each of you.

The experiment wouldn't be in its current state without the support from the mechanics and electronics workshops at department 4.4 and QUEST. On the mechanics side, thanks to Sven Klitzing, Alex Pablocki, Rebecca Müller, Martin Menzel, Thomas Leder and Hans-Albert Kremling. I could always rely on you to quickly come up with the parts I needed, even when I bothered you with urgent requests. The same can be said about the electronics workshops - thanks to Burghard Lipphardt, Andreas Hoppmann, Peter Carstens, Julia Fenske, Nikolai Beev, and Michael Kazda. Besides always helping out quickly and providing us with reliable devices (with one notable exception, but that can't be blamed on you...), you've also taught me a lot along the way.

I am very grateful to the people who kept me sane by dealing with the surrounding bureaucracy, namely Sandra Ludwig and Martina Bäumler at PTB, and Birgit Ohlendorf at LUH. Your help and patience has made my life a lot easier.

It has been a pleasure to work along the members of Piet Schmidt's and Christian Ospelkaus' groups. Thanks to Ian Leroux for some tremendously helpful discussions. In no particular order, thanks to Sana Amairi, Martina Wahnschaffe, Jannes Wübbena, Yong Wan, Florian Gebert, Börge Hemmerling, Olaf Mandel, Ivan Sherstov, Nils Scharnhorst, Tobias Leopold, Matthias Kohnen, Amado Bautista-Salvador, Fabian Wolf, Jan-Christoph Heip, Chunyan Shi, Stephan Hannig, Kornelius Jakobsen, and Johannes Kramer for many interesting discussions, some fun (and surprisingly dangerous) activities outside of work and lots of shared espressi / mokka and pizza.

Thanks to Ian, Heather, and Tanja for taking the time to read and comment on this manuscript.

I would like to thank my family and friends for their support and occasional distraction from work. And, lastly, apologies to anyone I might have forgotten to mention just now.

Curriculum vitae

Personal information

Name	Jonas Keller
Date of birth	December 5th, 1983
Place of birth	Groß-Umstadt, Germany

Education

2010 - 2015	**Physikalisch-Technische Bundesanstalt and Leibniz Universität Hannover** Doctoral studies Advisers: Dr. Tanja E. Mehlstäubler, Prof. Dr. Piet O. Schmidt
2007 - 2009	**TU Darmstadt** M.Sc. in Physics Master Thesis topic: *"Coherent manipulation of laser-cooled metastable neon atoms using Stimulated Raman Adiabatic Passage"* Adviser: Prof. Dr. G. Birkl
2004 - 2007	**TU Darmstadt** B.Sc. in Physics Bachelor Thesis topic: *"Experiments on the self-mixing effect in semiconductor lasers"* Adviser: Prof. Dr. W. Elsäßer
2003	**Gymnasium Michelstadt** Abitur

List of publications

- J. Keller, H. L. Partner, T. Burgermeister, and T. E. Mehlstäubler, “Precise determination of micromotion for trapped-ion optical clocks”, *J. Appl. Phys.* **118**, 104501 (2015)

- H. L. Partner, R. Nigmatullin, T. Burgermeister, J. Keller, K. Pyka, M. B. Plenio, A. Retzker, W. H. Zurek, A. del Campo, and T. E. Mehlstäubler, “Structural phase transitions and topological defects in ion Coulomb crystals”, *Physica B* **460**, 114 (2015)

- J. Keller, S. Ignatovich, S. A. Webster, and T. E. Mehlstäubler, “Simple vibration insensitive cavity for laser stabilization at the 10^{-16} level”, *Appl. Phys. B* **116**, 203 (2014)

- K. Pyka, N. Herschbach, J. Keller, and T. E. Mehlstäubler, “A high-precision segmented Paul trap with minimized micromotion for an optical multiple-ion clock”, *Appl. Phys. B* **114**, 231 (2014)

- H. L. Partner, T. Burgermeister, K. Pyka, J. Keller, and T. E. Mehlstäubler, R. Nigmatullin, A. Retzker, and M. B. Plenio, “Dynamics of topological defects in ion Coulomb crystals”, *New J. Phys.* **15**, 103013 (2013)

- K. Pyka[1], J. Keller[1], H. L. Partner, R. Nigmatullin, T. Burgermeister, D.-M. Meier, K. Kuhlmann, A. Retzker, M. B. Plenio, W. H. Zurek, A. del Campo, and T. E. Mehlstäubler, “Topological defect formation and spontaneous symmetry breaking in ion Coulomb crystals”, *Nat. Commun.* **4**, 2291 (2013)

- N. Herschbach, K. Pyka, J. Keller, and T. E. Mehlstäubler, “Linear Paul trap design for an optical clock with Coulomb crystals”, *Appl. Phys. B* **107**, 891 (2012)

---

[1] equal contributions